

Mathematisch–Naturwissenschaftlich–Technische Fakultät  
der Martin-Luther-Universität Halle–Wittenberg

## Dissertation

zur Erlangung des akademischen Grades  
doctor rerum naturalium (Dr. rer. nat.)

# Effect of Point Defects and Dislocations on Electrical and Optical Properties of III-V Semiconductors

vorgelegt von

Haile Lei

geboren am 20. 08. 1975 in Mianzhu, China

Gutachter:

1. Priv.-Doz. Dr. Hartmut S. Leipner, Martin-Luther Universität, Halle
2. Prof. Dr. Ulrich M. Gösele, Max-Planck Institut, Halle
3. Prof. Dr. J. R. Niklas, TU Bergakademie, Freiberg

Halle, November 2003

**urn:nbn:de:gbv:3-000005620**

[<http://nbn-resolving.de/urn/resolver.pl?urn=nbn%3Ade%3Agbv%3A3-000005620>]



# Zusammenfassung

Raman-, Katodolumineszenz- und Transmissionselektronenmikroskopie, sowie Positronenannihilation wurden eingesetzt, um den Einfluss von Punktdefekten wie Dotierungsatome, Galliumleerstellen, Leerstellenkomplexe und Versetzungen auf die elektrischen und optischen Eigenschaften der III-V-Halbleiter GaAs und GaN zu untersuchen. Dabei lag der Schwerpunkt auf der Wechselwirkung von Punktdefekten mit Versetzungen. Ein sogenanntes Diffusions-Drift-Aggregations-Modell (DDA-Modell) wurde entwickelt, um die mikroskopischen kinetischen Prozesse der Punktdefekte bezüglich ihrer Wechselwirkungen mit Versetzungen zu beschreiben. Computersimulationen auf der Grundlage des DDA-Modells wurden durchgeführt. Diese ergaben, dass die konventionelle Cottrellatmosphäre die Aggregation von Punktdefekten an einer Versetzung nicht immer korrekt beschreiben kann. Es ist die Bildung von Arsenausscheidungen an der Versetzung, die in einem räumlich ausgedehnten Anstieg der Dichte freier Elektronen an der Versetzung im Vergleich zur Matrix in n-Typ GaAs:Si und GaAs:S resultiert, wie es in Messungen mittels Ramanstreuung gefunden wurde. Das Auftreten von Arsenausscheidungen kann sowohl kinetisch mit dem DDA-Modell als auch energetisch aus molekulardynamischen Simulationen begründet werden. Die Aggregation von Punktdefekten an Versetzungen in n-Typ GaAs hängt ab von der Zeit der thermischen Behandlung, der Temperatur, dem Arsendampfdruck und der Dotierungskonzentration. Die örtliche Variation der Lumineszenz von der Matrix zur Versetzung wird erklärt durch die Berücksichtigung der Punktdefektagglomeration an Versetzungen. Die Unterschiede in den Lumineszenzbändern für niedrige und hohe Dotierungskonzentrationen wurden analysiert. Die entsprechenden Defekte wurden identifiziert und ihre Energieniveaus in der Bandlücke bestimmt. Galliumleerstellen-Komplexe wurden verantwortlich gemacht für die Bande der gelben Lumineszenz bei 2,2 eV in n-Typ GaN. Ihre Anreicherung an Versetzungen wird in Beziehung gesetzt zum Abfall in der Konzentration freier Elektronen an der Versetzung, wie er in Raman- und Katodolumineszenzmessungen gefunden wurde.

# Abstract

Raman scattering, cathodoluminescence (CL), transmission electron microscopy (TEM) as well as positron annihilation technique (PAT) have been applied to investigate the effect of point defects, such as dopants, gallium vacancies, and vacancy-related complexes, and dislocations on electrical and optical properties of III–V compound semiconductors, GaAs and GaN by concentrating on the interactions of point defects with dislocations. A so-called diffusion–drift–aggregation (DDA) model has been developed to describe the microscopic kinetic processes of point defects due to the interactions between them and dislocations. Computer simulations based on the DDA model have been carried out to reveal that the conventional “Cottrell” atmosphere cannot always correctly describe the aggregation of point defects at the dislocation and it is the formation of arsenic precipitates at the dislocation that results in the spatially extended increase in the free-electron concentration from the matrix to the dislocation in n-type GaAs:Si and GaAs:S, as indicated by Raman scattering. The arsenic precipitation at the dislocation in GaAs is found to be kinetically and energetically favorable by using the DDA model and molecular dynamics (MD) simulations. The aggregation of point defects at the dislocation in n-type GaAs is elucidated to depend on annealing time, temperature, arsenic pressure, and the doping level. The spatial variation of the luminescence from the matrix to the dislocation has been explained by considering the aggregation of point defects around the dislocation. The difference of the luminescence bands from the low doping level to the high doping level has been analyzed and the defects responsible for them have been identified. The energy levels of the corresponding defects in band gap have been determined. The gallium-vacancy-related complexes have been deduced to be responsible for the yellow luminescence band at 2.2 eV in n-type GaN. Their aggregation at the dislocation is revealed to result in the decrease in the free-electron concentration from the matrix to the dislocation by Raman scattering and cathodoluminescence.

# Contents

<b>1</b>	<b>Introduction</b>	<b>1</b>
<b>2</b>	<b>Theory of Interactions of Point Defects with Dislocations</b>	<b>5</b>
2.1	Atomic structures of dislocations in GaAs and GaN . . . . .	5
2.2	Diffusion–drift–aggregation model . . . . .	6
2.3	Fermi-level effect . . . . .	9
2.4	Arsenic-pressure effect . . . . .	10
2.5	Diffusion mechanisms in the diffusion–drift–aggregation model . . . . .	10
2.5.1	Diffusion mechanism in n-type GaAs:Si . . . . .	11
2.5.2	Diffusion mechanism in n-type GaAs:S . . . . .	13
<b>3</b>	<b>Experiments</b>	<b>17</b>
3.1	Raman Scattering . . . . .	17
3.1.1	Fundamental principle of Raman scattering . . . . .	17
3.1.2	Selection rule . . . . .	18
3.1.3	Electric effects . . . . .	19
3.1.4	Constituents of Raman spectroscopy . . . . .	21
3.2	Cathodoluminescence (CL) . . . . .	22
3.2.1	Fundamental principle of CL . . . . .	22
3.2.2	Effect of external conditions on CL spectra . . . . .	23
<b>4</b>	<b>Interactions of Point Defects with Dislocations in GaAs:Si</b>	<b>27</b>
4.1	Experimental methods . . . . .	27
4.2	Results and discussion . . . . .	29
<b>5</b>	<b>Interactions of Point Defects with Dislocations in GaAs:S</b>	<b>35</b>
5.1	Effect of in-grown dislocations on electrical and optical properties . . . . .	35
5.2	GaAs:S with fresh dislocations . . . . .	39
5.2.1	Effect of dislocations on the luminescence of GaAs:S with doping levels . . . . .	39
5.2.2	TEM observations of fresh dislocations . . . . .	43
5.3	Why are arsenic precipitates formed at dislocations . . . . .	45
5.3.1	Energetic factor . . . . .	45
5.3.2	Kinetic factor . . . . .	48
5.4	Computer simulations of spatial distribution of point defects . . . . .	50
5.4.1	Time evolution of the system . . . . .	51
5.4.2	As-pressure effect . . . . .	53
<b>6</b>	<b>Identification of luminescence bands in n-type GaAs</b>	<b>57</b>
6.1	Luminescence bands in n-type GaAs:Si . . . . .	57
6.2	Luminescence bands in n-type GaAs:S . . . . .	63
<b>7</b>	<b>Dislocations in GaN</b>	<b>69</b>

7.1 Experiments . . . . .	69
7.2 Results and discussion . . . . .	70
<b>8 Summary and Conclusion</b>	<b>77</b>

# 1 Introduction

Historically, most semiconductor devices have been created on a silicon-based crystal material. However, a growing number of electronic and optoelectronic devices are now being developed with requirements that exceed the capabilities of silicon. Lots of applications demand power-efficient high performance systems which can operate at high frequencies with lower power consumption and less noise and which can be produced cost-effectively in high volume. As a result, semiconductor device manufacturers are increasingly using compound semiconductor materials such as gallium arsenide (GaAs) and gallium nitride (GaN) to improve the performance of semiconductor devices and to enable new applications. GaAs has superior electronic and optical properties for providing high mobility of carriers and low power consumption. Moreover, GaAs-based devices can operate at microwave frequencies, whereas Si-based devices cannot. At present, GaAs has been widely used to build devices such as power amplifiers, radio frequency integrated circuits used in wireless handsets, high-brightness light emitting diodes (HBLEDs) and vertical cavity surface emitting lasers (VCSELs). Due to its wide band-gap character (3.4 eV), GaN is predicted to be one of the most promising semiconductor materials in the twenty-first century and it is expected to be applied in such areas as high-brightness blue and green light emitting diodes (LED), blue lasers, high power and high frequency electronics, high temperature electronics, ultraviolet detectors as well as electronics for microwave applications.

The first step in producing a semiconductor device is to grow a crystal or a film of the material. Historically, two main methods have been applied to grow compound semiconductor single crystal, the liquid encapsulated Czochraski (LEC) and the horizontal Bridgeman (HB) techniques. The two techniques have difficulties in producing six-inch, high-quality and low-cost semiconductor crystals. Now the producers have been tending to use the vertical gradient freezing (VGF) technique to grow compound semiconductors. Although it is still difficult to grow high-quality GaN single crystals, the techniques for GaN films are frequently vapor phase epitaxy (VPE), including metal-organic VPE and molecular beam epitaxy (MBE). During fabrication of semiconductor materials or during construction of the devices by utilizing the semiconductor materials, point and extended defects are inevitably created. It is thus essential to understand how the defects affect mechanical, electrical, and optical properties of the materials. How to minimize the possible disadvantages or how to convert them into useful effects stimulate fruitful studies all over the world.

Point defects such as impurities, vacancies and interstitial often induce localized electronic levels into the band gap of a semiconductor. The states can trap electrons or holes, thus possibly inducing compensation, scattering free carriers and introducing new luminescence bands with different energy and intensity from the near-band-edge emissions, and subsequently result in a change in electrical and optical properties. For example, parasitic optical transitions have been believed to result in luminescence bands at 1.20 eV in GaAs and at 2.2 eV in GaN, related to complexes formed by donors and gallium vacancies. Besides their influence on the electronic structure, point defects (usually charged in semiconductors) may also induce a significant lattice distortion. The magnification of a distortion depends on the charge state of defects, i.e. the Jahn-Teller effect. Consequently, all the properties related to such quantities as defect concentration at thermal equilibrium, solubility, and diffusivity as well as electron-phonon interactions are charge-state dependent.

Extended defects such as dislocations, grain boundaries and stacking faults have been widely investigated and have been revealed to have crucial influences on the mechanical, electrical and optical properties of semiconductors. Dislocations are known as non-radiative recombination centers to reduce the lifetime of excess minority carriers and to degrade the performance of GaAs- and GaN-based light emitters. The presence of space charge around dislocations was suggested to be responsible for the reduction of current gains in AlGaAs/GaAs heterojunction bipolar transistors (HBTs), lowering efficiency of solar cell, and degrading the breakdown voltage of GaAs-based power varactor diodes [1, 2]. It has been demonstrated that the threshold voltage of field effect transistors (FETs) built on the GaAs substrate depends on the distance to neighboring dislocations [3].

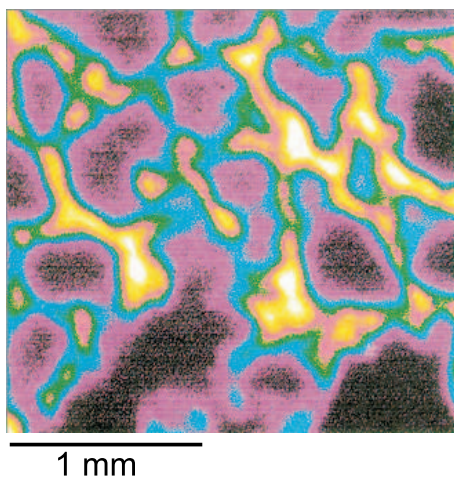


*Figure 1.1:* Photoluminescence map of the near-band-edge emission ( $\lambda = 832$  nm), revealing the influence of non-radiative recombination centers and inhomogeneous distribution of shallow-level defects on luminescence of GaAs (from Freiburger Compound Materials, Germany).

Dislocations are specific linear defects disturbing the regular sequence of atomic planes. Different from point defects, which disturb the short-range order of a crystal, dislocations disturb the long-range order. Dislocations are particularly generated by plastic deformation. A dislocation can be formed either by the collapse of a vacancy pancake or by incorporation of a layer of interstitial atoms. According to the relationship between Burgers vector and the dislocation line, there are two kinds of dislocations: edge or screw dislocation. The dislocations are well known as sinks of point defects (impurities or intrinsic point defects) to result in an inhomogeneous distribution in the electrical and optical properties of the materials (e.g., see Fig.1.1). This effect, called gettering effect, shows how the dislocations may play a significant role in controlling the detrimental effects of point defects in the active regions of semiconducting devices. It is usually utilized in defect engineering to remove the unfavorable defects from the matrix or to limit the amorphization of GaAs only in dislocation regions [4]. The interactions of different defects with dislocations can have different consequences, e.g., either hindering or promoting the dislocation climb. Doping with electrically active atoms such as Si, In or B in GaAs has been found to result in a dramatic reduction of the dislocation density [5–7], which was suggested to result from the reduction of the Fermi-energy-dependent activation energy of dislocation motion or metallurgical hardening [8]. Since strongly reconstructed dislocations in Si and GaAs are widely assumed to be electrically inactive except possibly for shallow levels, any electrical effect correlated with them have to result from point defects attached to the dislocation line [10]. For example, a threefold-coordinated vacancy in the core of a  $30^\circ$  partial in Si has been identified as being responsible for the Si-Y line in the dislocation-related electron paramagnetic resonance (EPR) [11]. In the case of GaN, transmission electron microscopy (TEM) and atomic force microscopes (AFM) in combination with cathodoluminescence revealed that threading dislocations exhibit dark contrasts, leading to the conclusion that they act as non-radiative recombination centers to degrade the luminescence efficiency in blue-light spectra of the GaN epilayer [12]. However, other investigations showed a higher intensity of the yellow luminescence near the threading edge dislocations and that efficient light-emitting diodes and lasers are feasible by using GaN-based crystal with a high density of dislocations ( $10^9 - 10^{10} \text{ cm}^{-2}$ ) [13].

---

The aggregation of point defects at the dislocations is generally assumed as a “Cottrell” atmosphere, i.e. a short-range increase (about tens of nm) in the number of point defects. The Cottrell atmosphere is often supposed to explain qualitatively some experimental observations although it presents poorly quantitative information. A specific instance is that it cannot interpret why the free-electron concentration in n-type GaAs:Si and GaAs:S increases from the matrix to the dislocation and why the extension in the increase is as broad as 10  $\mu\text{m}$  around the dislocation, as revealed by the experiments presented below [14, 15]. Moreover, in doped semiconductors, where there are various defects such as donors or acceptors, it is not clear how the aggregation of the defects at the dislocation affects the resultant electrical and optical properties.

In the thesis, I deal with the effect of point defects and dislocations on electrical and optical properties of III–V semiconductors, GaAs and GaN. Main emphasis is put on the interactions between point defects and dislocations. I will elucidate the spatial redistribution of point defects due to the interaction, and as a result, the variation of electrical and optical properties from the matrix to the dislocation. The influence of external conditions such as temperature and pressure on the interaction between point defects and dislocations will be addressed. For these purposes, several experimental methods such as TEM, cathodoluminescence (CL), and Raman scattering will be combined with computer simulations based on a diffusion–drift–aggregation model and molecular dynamics (MD) simulations. I will firstly focus on n-type GaAs:Si and GaAs:S with in-grown dislocations. The free-electron concentration in GaAs:Si and GaAs:S will be found to increase from the matrix to the dislocation with an extended radius of 10  $\mu\text{m}$ . Computer simulations and theoretical analysis will suggest that whether arsenic precipitates can be formed at the dislocation or not play an important role in determining the spatial distribution of point defects and the free-electron concentration. It will be theoretically elucidated that the formation of arsenic precipitates at the dislocations is energetically and kinetically favorable.

Secondly, in order to further concentrate on the interactions of dislocations with point defects, a layer of fresh dislocations introduced by scratching the (001) surface of n-type GaAs:S with different sulfur concentrations is investigated after thermal treatments under different conditions. The results indicate that the effect of the dislocations on the spatial distribution of the point defects and on the electrical and optical properties depends strongly on temperature and the doping level. The luminescence bands and their origins will be addressed in detail. I will especially identify which defects are responsible for the luminescence bands around 0.95 eV, 1.20 eV, and 1.30 eV. The donor–gallium vacancy complexes will be revealed to be formed commonly in n-type GaAs doped with different donors occupying gallium lattice sites or arsenic lattice sites. The doping level is found to influence the charge state of a gallium vacancy and its surrounding, i.e., how many donors are bound to a gallium vacancy. As a result, three types of gallium vacancy-related complexes may be formed and the resultant luminescence bands may be located at different energies.

Lastly, the electrical and optical properties of GaN with in-grown or fresh dislocations are studied to explore the origin of the yellow luminescence band at 2.2 – 2.3 eV and the effect of dislocations on luminescence in GaN. The role of defects and dislocations in GaN will be discussed there.



## 2 Theory of Interactions of Point Defects with Dislocations

In the past decades, many theoretical studies were carried out for metals to investigate the interactions of point defects with dislocations. In those studies, a diffusion–drift equation has been introduced to describe the kinetics of mobile point defects due to the existence of dislocations. Compared to the situation in metals, the interaction in semiconductors is more complex because point defects are often charged and thus their diffusivity is Fermi-level dependent. Up to now, there is no theoretical description of the interaction of point defects with dislocations in semiconductors despite its important effect on, e.g. the transport properties of carriers [16].

### 2.1 Atomic structures of dislocations in GaAs and GaN

In diamond (e.g., Si) and zinc-blende crystals (e.g., GaAs), perfect dislocations have  $a/2\langle 110 \rangle$  Burgers vectors ( $a$  is the lattice constant) and  $\{111\}$  slip planes, as in face centered cubic (f.c.c) crystals. They are usually dissociated into two Shockley partial dislocations with  $a/6\langle 112 \rangle$  Burgers vectors on the same slip plane to lower the energy. Between the two partials, a stacking fault ribbon is formed. A  $60^\circ$  dislocation is dissociated into a  $90^\circ$  and a  $30^\circ$  partial, while a screw dislocation into two  $30^\circ$  partials. There are two possible types of  $\{111\}$  slip planes due to the existence of two sorts of sublattices to result in two types of dislocations: a “*shuffle-set*” dislocation formed by the relative shear shift of one part of the crystal with respect to the other between the two neighboring  $\{111\}$  planes of one same sublattice; and a “*glide-set*” dislocation formed by the relative shear between the neighboring two  $\{111\}$  planes of one and the other sublattices. The dislocations in diamond and zinc-blende crystals actually belong to the glide-set dislocations because the arrangement of the orbitals containing unpaired electrons is more suitable for the rebonding in the core of the glide-set dislocation than in the shuffle-set dislocation core to reduce the total energy of the system. In GaAs, all the atoms in the core of a given segment of partial dislocations are chemically identical. The dislocation core in GaAs is reconstructed with a single-period (SP) atomic structure similar to Si to eliminate the dangling bonds (see Fig. 2.1) [17]. Although the SP structure is widely assumed to represent the physically correct core structure, recent theoretical calculations indicated that a double-period (DP) structure of a dislocation core in Si and GaAs is lower in energy [18, 19]. Compared to unreconstruction dislocations, the reconstruction has two consequences. The dislocation is of low mobility, since the energy necessary to form a kink or a jog would be high. The short core bonds lead to bonding and antibonding gap levels with a large separation so that the dislocations would be electrically inactive except for possible shallow levels in the band gap. The reconstruction is strongly influenced by electrically active impurities present in the core, e.g., acceptors (Be or Zn) destroy the reconstruction of  $\beta$  partials while donors (C or Te) destroy the reconstruction of  $\alpha$  dislocations, leading to a pinning effect in GaAs [17, 20]. The segregation of impurities at the dislocation core was additionally found to change the Fermi level to affect the mobility of the dislocation [21].

Unlike Si and GaAs, GaN has two different crystal structures, wurtzite (hexagonal) and zinc-blende (cubic), the former being more stable than the latter. Screw dislocations in GaN with the

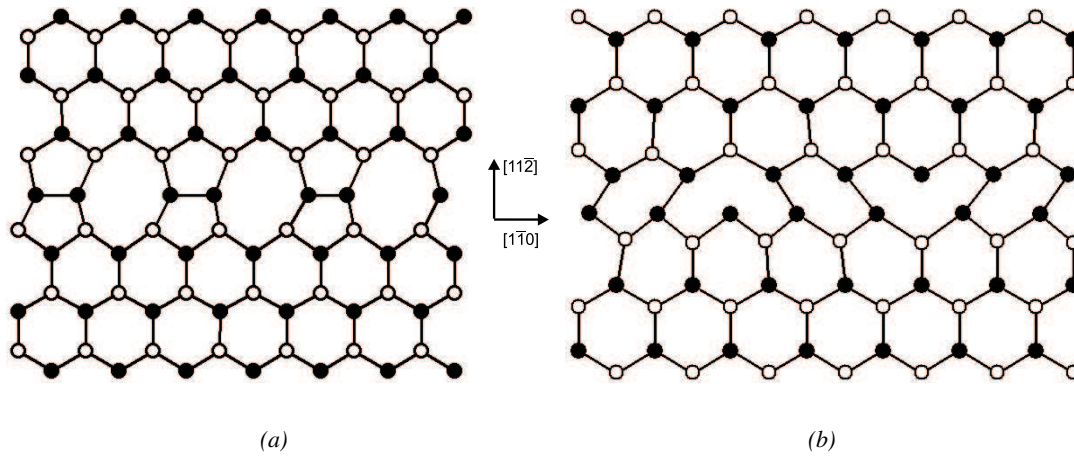


Figure 2.1: Atomic structures of the reconstructed cores of (a) the 30° and (b) 90° partial dislocations on the (111) slip plane in GaAs. Dark spheres represent Ga atoms and dark circles As atoms or vice versa [17].

wurtzite structure are not dissociated and have  $\langle 0001 \rangle$  Burgers vectors and  $\{0001\}$  slip planes and exist as open-core dislocations. Perfect edge dislocations have  $a/3 \langle 11\bar{2}0 \rangle$  Burgers vectors and  $\{0001\}$  slip planes as full-core dislocations (see Fig. 2.2) [22]. Three kinds of partial dislocations can be expected as the result of the dissociation of perfect edge dislocations: Shockley partials with  $a/3 \langle 10\bar{1}0 \rangle$  Burgers vector, Frank partials with  $a/2 \langle 0001 \rangle$  Burgers vector, and Frank–Shockley partials with  $a/6 \langle 20\bar{2}3 \rangle$  Burgers vector. Different from the dislocation core in GaAs, the cores of both screw and edge dislocations in GaN are stoichiometric with a structure similar to that of the  $(10\bar{1}0)$  surfaces. This means that the 3-fold coordinated atoms in the core move in such a way to enhance  $sp^2$  and  $p^3$  hybridization. The energy levels of the empty Ga pairs are pushed upwards the covalent band and the energy levels of filled nitrogen atoms lie near the valence band in a manner identical to the  $(10\bar{1}0)$  surface. As a result, both the screw and edge dislocations are electrically inactive except for possible shallow levels in bandgap, despite the existence of dangling bonds. The strained dangling bonds at the dislocations allow impurities or point defects to be trapped there. However, recent theoretical calculations indicated that the edge dislocation is electrically active due to, e.g., Ga vacancies [23–25] or Ga vacancies complexed with oxygen at the dislocation [26], introducing deep-level electron traps into the band gap, which contribute to the yellow luminescence (YL) [23–26].

In addition to straight dislocations, dislocation loops may be formed by condensation of interstitial or vacancies. When crystals are rapidly cooled from a temperature close to the melting point, the high-temperature equilibrium concentration of vacancies may be retained in a supersaturated state and the vacancies can thus agglomerate to form the void. If the host-lattice planes bow towards the center of the void, a “vacancy-type” dislocation loop is formed. A wave of atoms driven by the reconstruction on internal surfaces of the void can also precipitate into pillars within the void and produce an “interstitial-type” dislocation loop, at which the host-lattice planes bow away from the center of the loop [27].

## 2.2 Diffusion–drift–aggregation model

In addition to a diffusion flux, resulting from the transport process of point defects from a high to a low concentration region, a drift flux must be accounted for as a result of the interaction of point defects with dislocations. In general, the interaction of point defects with dislocations originate

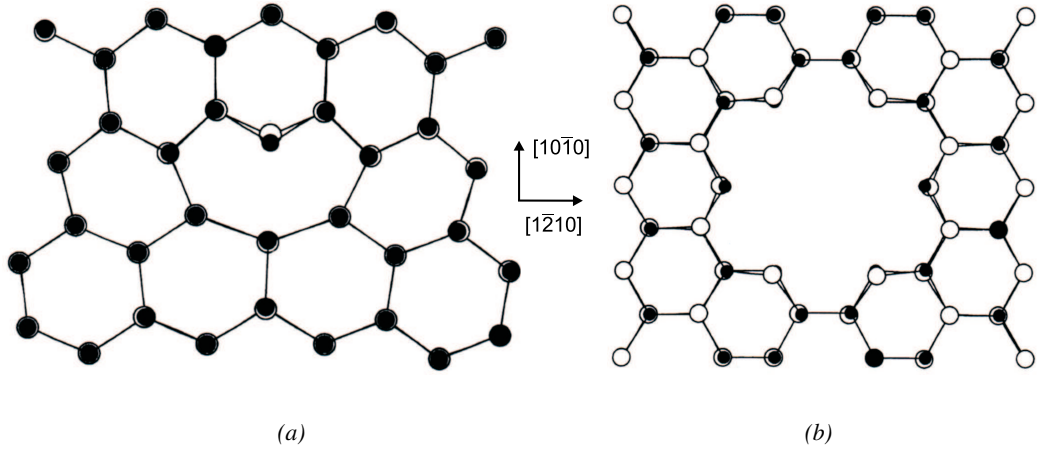


Figure 2.2: Atomic structures of the reconstructed cores of the edge (a) and screw (b) dislocations on the (0001) slip plane in GaN. Dark spheres represent Ga atoms and dark circles N atoms [22].

from three effects: the size misfit, the difference in elastic constants, and the possible electrostatic interactions resulting from the electric dipole and dangling bonds around a dislocation core. The size misfit is the dominant effect on the interaction of point defects with the edge dislocation [28]. The interaction energy  $\phi$  due to the size misfit is estimated in elastic theory by

$$\phi(r) = -\frac{A}{r} \sin\theta \text{ and } A = \frac{4}{3} \mu \varepsilon r_a^3 b \left( \frac{1+\nu}{1-\nu} \right), \quad (2.1)$$

where  $r$  is the distance of point defects to the edge dislocation.  $\mu$  and  $\nu$  are the shear modulus and Poisson's ratio, respectively.  $b$  is the magnitude of the Burgers vector of the dislocation.  $\varepsilon$  is the size misfit between the host atoms and defects.  $r_a$  and  $r_a(1 + \varepsilon)$  are the respective atomic radii of the host atoms and point defects. The angular dependence of  $\phi(r)$  is neglected for simplicity by setting  $\sin\theta = 1$  (see Fig. 2.3). Therefore, under the condition without other effects like precipitation, the fundamental equation governing the variation rate of the defect concentration  $C(r, t)$  around a dislocation can be expressed as [28]

$$\frac{\partial C(r, t)}{\partial t} = \nabla F(r, t), \quad (2.2)$$

and

$$F(r, t) = D \left[ \nabla C(r, t) + \frac{C(r, t)}{k_B T} \nabla \phi(r) \right], \quad (2.3)$$

where  $t$  is the time,  $D$  the diffusion coefficient of defects and  $C(r, t)$  the defect concentration at the distance  $r$  from the dislocation at time  $t$ .  $F(r, t)$  is the diffusion–drift flux.  $k_B$  is the Boltzmann constant and  $T$  the temperature in unit of Kelvin. The first term of the right side of Eq. (2.3) is the diffusion flow, while the second term is the drift flow due to the force between the point defect and the dislocation. It is assumed that the defect concentration  $C_{core}$  within the dislocation core  $r < r_0$  ( $r_0$  is the radius of a dislocation core) is a constant, i.e.  $C_{core}(t) = C(r_0, t)$ . Given the dislocation core is cylindrical, the variation rate of the defect concentration with time is just the net flow into the core region,

$$\pi r_0^2 \frac{dC(r_0, t)}{dt} = 2\pi r_0 F(r_0, t). \quad (2.4)$$

By integrating Eq. (2.4), the core boundary condition for Eq. (2.2) may be written as

$$C(r_0, t) = C(r_0, 0) + \frac{2}{r_0} \int_0^t F(r_0, t) dt. \quad (2.5)$$

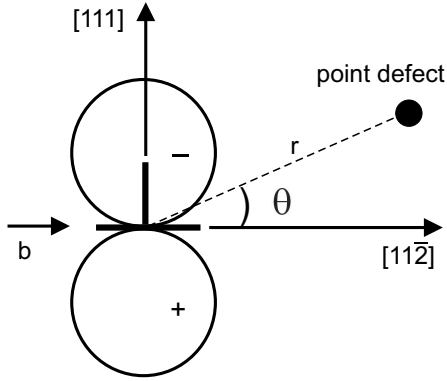


Figure 2.3: Scheme of the interaction of a point defect with an edge dislocation in GaAs. "-" denotes compressive region and "+" tensile region caused by the dislocation. The scheme only shows one component of the stress field due to the dislocation.

dislocation outwards to balance the drift flux towards the dislocation, i.e.  $F(r, t \rightarrow \infty) = 0$  everywhere. With the assumptions that the concentration of point defects at any point in the crystal never exceeds their solubility limit and remains low with respect to the density of the lattice sites, the spatial distribution of point defects at equilibrium in the field of dislocations must obey Boltzmann statistics,

$$C(r) = C_0 \exp[-\phi(r)/k_B T], \quad (2.7)$$

by solving  $F(r, t \rightarrow \infty) = 0$  [see Eq. (2.3)], where  $C_0$  is the defect concentration remote from the dislocation when the system is at equilibrium.

Since the solubility of the charged defects in semiconductors depends strongly on the local free-carrier concentration, a so-called "segregation" effect must be considered, as suggested by You et al [29]. The general diffusion equation is thus expanded to describe both the diffusion and the segregation of charged point defects in semiconductors [29],

$$\frac{\partial C(r, t)}{\partial t} = \nabla D \left[ \nabla C(r, t) - \frac{C(r, t)}{C^{eq}(r)} \nabla C^{eq}(r) \right], \quad (2.8)$$

where  $C(r, t)$  and  $C^{eq}(r, t)$  are respectively the actual and equilibrium concentration of point defects. The combination of Eqs. (2.2) and (2.8) gives an equation to describe the diffusion, the drift and the aggregation behaviors of point defects due to the existence of dislocations in semiconductors,

$$\frac{\partial C(r, t)}{\partial t} = \nabla D \left[ \nabla C(r, t) - \frac{C(r, t)}{C^{eq}(r)} \nabla C^{eq}(r) + \frac{C(r, t)}{k_B T} \nabla \phi(r) \right] + \Psi. \quad (2.9)$$

As far as an isolated dislocation is concerned, the second boundary condition is that the concentration of point defects remains constant, i.e.  $C(r \rightarrow \infty, t) = C(r \rightarrow \infty, t = 0)$  at the position far from the dislocation. If there is a finite dislocation density  $\rho$ , the second boundary condition is that there is no net flux at points midway between the dislocations,  $R = (\pi\rho)^{-1/2}$ , i.e.

$$F(R, t) = 0. \quad (2.6)$$

If the interaction potential  $\phi(r)$  is assumed to promote the movement of point defects towards dislocations, the concentration of point defects must decrease with the distance from the dislocation after a long time when the system reaches equilibrium so that the concentration gradient causes the diffusion flux from

In Eq. (2.9),  $\Psi$  represents the effect of other possible factors like precipitation on the defect concentration. Eq. (2.9) is the fundamental relationship which will be applied in the following simulations of the diffusion–drift–aggregation processes in n-type GaAs:Si and GaAs:S.

## 2.3 Fermi-level effect

In a semiconductor, although the thermal equilibrium concentration of a kind of neutral impurity atoms or point defects is independent of the position of the Fermi level, it is not true for a charged one. The equilibrium concentration of a kind of charged donors ( $z+$ ) or acceptors ( $z-$ ) as a function of Fermi level has been deduced as [30, 31]

$$C_{d^{z+}}^{\text{eq}} = \frac{C_{d^0}^{\text{eq}}}{g_d} \exp \left[ \left( \sum_{i=1}^z E_{d^{i+}} - zE_F \right) / k_B T \right], \quad (2.10)$$

$$C_{a^{z-}}^{\text{eq}} = \frac{C_{a^0}^{\text{eq}}}{g_a} \exp \left[ \left( zE_F - \sum_{i=1}^z E_{a^{i-}} \right) / k_B T \right]. \quad (2.11)$$

In Eqs. (2.10) and (2.11),  $E_F$  is the Fermi-level position,  $E_{d^{i+}}$  the donor level with  $i$  positive charges and  $E_{a^{i-}}$  the acceptor level with  $i$  negative charges.  $C_{d^0}^{\text{eq}}$  is the equilibrium concentration of neutral donors and  $C_{a^0}^{\text{eq}}$  the equilibrium concentration of neutral acceptors.  $g_d$  is the energy-level degeneracy factor of donors, which is equal to 2.  $g_a$  is the energy-level degeneracy factor of acceptors, which is equal to 4.

In an n-type semiconductor,  $n_i = N_C \exp [(E_F^i - E_C) / k_B T]$ ,  $n = N_C \exp [(E_F - E_C) / k_B T]$  and  $E_C$  is the conduction band edge position,  $E_F^i$  the intrinsic Fermi level position,  $n$  ( $n_i$ ) the (intrinsic) free-electron concentration (FEC),  $N_C$  the effective density of states of the conduction band. So Eq. (2.10) for shallow-level donors ( $E_d \approx E_C$ ) can be written as

$$C_{d^{z+}}^{\text{eq}}(n) = \frac{C_{d^0}^{\text{eq}}}{g_d} \left( \frac{n_i}{n} \right)^z \exp \left( \frac{zE_C - zE_F^i}{k_B T} \right). \quad (2.12)$$

Specially, for intrinsic donors and acceptors with  $z$  charge states in n-type semiconductors,

$$\frac{C_{d^{z+}}^{\text{eq}}(n)}{C_{d^{z+}}^{\text{eq}}(n_i)} = \left( \frac{n}{n_i} \right)^{-z} \quad \text{and} \quad \frac{C_{a^{z-}}^{\text{eq}}(n)}{C_{a^{z-}}^{\text{eq}}(n_i)} = \left( \frac{n}{n_i} \right)^z \quad (2.13)$$

holds from Eqs. (2.10) and (2.11).

Similarly, in a p-type semiconductor,  $n_i = N_V \exp [(E_V - E_F^i) / k_B T]$ ,  $p = N_V \exp [(E_V - E_F) / k_B T]$  and  $E_V$  is the valence band edge position,  $p$  the hole concentration,  $N_V$  the effective density of states of the valence band. So Eqs. (2.11) for shallow-level acceptors ( $E_a \approx E_V$ ) can be written as

$$C_{a^{z-}}^{\text{eq}}(p) = \frac{C_{a^0}^{\text{eq}}}{g_a} \left( \frac{n_i}{p} \right)^z \exp \left( \frac{zE_F^i - zE_V}{k_B T} \right), \quad (2.14)$$

and for intrinsic donors and acceptors with  $z$  charge states in p-type semiconductors,

$$\frac{C_{d^{z+}}^{\text{eq}}(p)}{C_{d^{z+}}^{\text{eq}}(n_i)} = \left( \frac{p}{n_i} \right)^z \quad \text{and} \quad \frac{C_{a^{z-}}^{\text{eq}}(p)}{C_{a^{z-}}^{\text{eq}}(n_i)} = \left( \frac{p}{n_i} \right)^{-z}. \quad (2.15)$$

Table 2.1: Arsenic pressure dependent concentration of point defects

Defect Type	Notation	$x$	As-Pressure dependent Concentration
Interstitial arsenic	$I_{As}$	1/4	$c_{I_{As}} \propto p_{As_4}^{1/4}$
Arsenic vacancies	$V_{As}$	-1/4	$c_{V_{As}} \propto p_{As_4}^{-1/4}$
Interstitial gallium	$I_{Ga}$	-1/4	$c_{I_{Ga}} \propto p_{As_4}^{-1/4}$
Gallium vacancies	$V_{Ga}$	1/4	$c_{V_{Ga}} \propto p_{As_4}^{1/4}$
Arsenic antisites	$As_{Ga}$	1/2	$c_{As_{Ga}} \propto p_{As_4}^{1/2}$
Gallium antisites	$Ga_{As}$	-1/2	$c_{Ga_{As}} \propto p_{As_4}^{-1/2}$

## 2.4 Arsenic-pressure effect

In III-V compound semiconductors, a thermodynamic range of non-stoichiometry exists at a specific temperature. So the thermal equilibrium concentrations of intrinsic point defects (vacancies, interstitial and antisites) in both sublattices depend upon the vapor pressure of the more volatile components, e.g. on the arsenic pressure in GaAs. The dominating vapor species is  $As_4$  in GaAs.

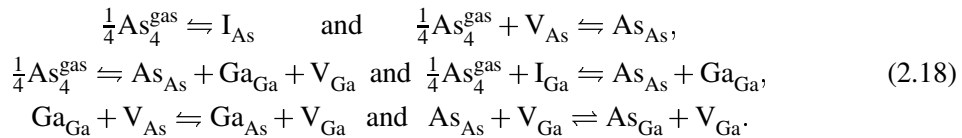
In GaAs, statistical thermodynamics elucidates that the concentration of a defect species, whatever charged state the defects are endowed with, depends on arsenic pressure  $p_{As_4}$  as [32]

$$C_D = C_0 \left( \frac{p_{As_4}}{B_{As_4}} \right)^x \exp \left( -\frac{G_D^{eff}}{k_B T} \right). \quad (2.16)$$

Here,  $C_0 = 2.215 \times 10^{22} \text{ cm}^{-3}$  denotes the density of arsenic or gallium sublattice sites.  $G_D^{eff}$  is the effective formation energy of a defect,  $x$  is the pressure exponent.  $B_{As_4}$  is the ideal gas pressure constant given by

$$B_{As_4} = \left( \frac{2\pi m_{As_4}}{h} \right)^{1/2} (k_B T)^{5/2} = 135.1 \times T^{5/2} \text{ atm}, \quad (2.17)$$

with  $m_{As_4}$  being the mass of an  $As_4$  molecule and  $h$  Planck's constant. The laws of mass actions for the gas-solid exchange reactions in GaAs,



predict that the corresponding pressure-dependent concentrations of the intrinsic point defects follow the relations in Table 2.1. As the concentration of point defects is As-pressure dependent, their diffusivity must also depend on the arsenic pressure. This point will be further discussed in Sec. 5.4.

## 2.5 Diffusion mechanisms in the diffusion-drift-aggregation model

In the practical applications, the concrete diffusion mechanisms must be considered to simulate the diffusion-drift-aggregation process of point defects at the dislocations. Starting from the general

descriptions of the diffusion–drift–aggregation processes of point defects due to their interactions with dislocations in semiconductors [see Eq. (2.9)], the detailed diffusion–drift–aggregation model under considerations of specific atomic diffusion mechanisms in GaAs:Si and GaAs:S will be constructed in this section. For simplicity, the mobility of the dislocation is neglected in the following model although the actual distribution of point defects around the dislocation might depend on the dislocation motion, which in turn is determined by the point-defect distribution. As a matter of fact, the dislocation climb may cause absorption of Ga vacancies (As interstitial) plus the simultaneous emission of As interstitials (Ga vacancies) [33] to lead their concentration to a local equilibrium [34].

### 2.5.1 Diffusion mechanism in n-type GaAs:Si

As suggested by You, Gösele and Tan [29], silicon atoms diffuse via Ga vacancies in n-type GaAs:Si as shown in Fig. 2.4.

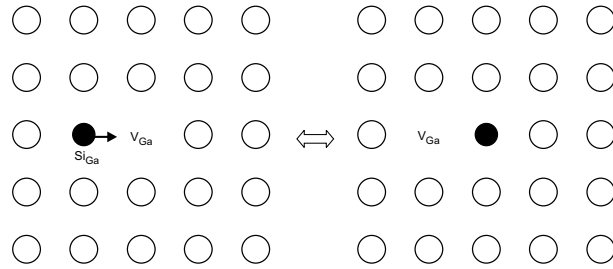


Figure 2.4: Schematic representation of the vacancy mechanism of the silicon diffusion in n-type GaAs:Si.

The triply negative charge state of a Ga vacancy ( $V_{\text{Ga}}^{3-}$ ) is assumed in n-type GaAs:Si [35]. The diffusion mechanism has been confirmed theoretically [36]. The effect of  $(\text{Si}_{\text{Ga}} V_{\text{Ga}})^{2-}$  complexes will be incorporated into the diffusion–drift–aggregation model because they largely exist in n-type GaAs:Si, as shown by cathodoluminescence measurements later. A  $(\text{Si}_{\text{Ga}} V_{\text{Ga}})^{2-}$  complex is formed by a reaction,



In order to process the information on the spatial distribution of point defects, a set of partial differential equations including the diffusion–drift–aggregation processes of  $\text{Si}_{\text{Ga}}^+$ ,  $V_{\text{Ga}}^{3-}$ , and  $(\text{Si}_{\text{Ga}} V_{\text{Ga}})^{2-}$  were solved numerically using the program package ZOMBIE [37].

$$K^+ C_{\text{Si}_{\text{Ga}}^+}^{\text{eq}} C_{V_{\text{Ga}}^{3-}}^{\text{eq}} = K^- C_{(\text{Si}_{\text{Ga}} V_{\text{Ga}})^{2-}}^{\text{eq}}, \quad (2.20)$$

$$\frac{\partial C_{(\text{Si}_{\text{Ga}} V_{\text{Ga}})^{2-}}}{\partial t} = K^+ C_{\text{Si}_{\text{Ga}}^+} C_{V_{\text{Ga}}^{3-}} - K^- C_{(\text{Si}_{\text{Ga}} V_{\text{Ga}})^{2-}}, \quad (2.21)$$

$$\frac{\partial C_{\text{Si}_{\text{Ga}}^+}}{\partial t} = \frac{\partial}{\partial r} \left[ D_{\text{Si}_{\text{Ga}}^+} \left( \frac{\partial C_{\text{Si}_{\text{Ga}}^+}}{\partial r} + \frac{C_{\text{Si}_{\text{Ga}}^+}}{n} \frac{\partial n}{\partial r} + \frac{C_{\text{Si}_{\text{Ga}}^+}}{k_B T} \frac{\partial \phi_{\text{Si}_{\text{Ga}}^+}}{\partial r} \right) \right] - \frac{\partial C_{(\text{Si}_{\text{Ga}} V_{\text{Ga}})^{2-}}}{\partial t} + \omega_1, \quad (2.22)$$

$$\frac{\partial C_{V_{\text{Ga}}^{3-}}}{\partial t} = \frac{\partial}{\partial r} \left[ C_{V_{\text{Ga}}^{3-}} \left( \frac{\partial C_{V_{\text{Ga}}^{3-}}}{\partial r} - 3 \frac{C_{V_{\text{Ga}}^{3-}}}{n} \frac{\partial n}{\partial r} + \frac{C_{V_{\text{Ga}}^{3-}}}{k_B T} \frac{\partial \phi_{V_{\text{Ga}}^{3-}}}{\partial r} \right) \right] - \frac{\partial C_{(\text{Si}_{\text{Ga}} V_{\text{Ga}})^{2-}}}{\partial t} + \omega_2. \quad (2.23)$$

where  $C_{\text{Si}_{\text{Ga}}^+}$ ,  $C_{V_{\text{Ga}}^{3-}}$  and  $C_{(\text{Si}_{\text{Ga}} V_{\text{Ga}})^{2-}}$  are the concentrations of  $\text{Si}_{\text{Ga}}^+$  donors,  $V_{\text{Ga}}^{3-}$ , and  $(\text{Si}_{\text{Ga}} V_{\text{Ga}})^{2-}$  acceptors;  $D_{\text{Si}_{\text{Ga}}^+}$  and  $D_{V_{\text{Ga}}^{3-}}$  are the diffusion coefficients of  $\text{Si}_{\text{Ga}}^+$  and  $V_{\text{Ga}}^{3-}$ , respectively.  $\omega_1$  and  $\omega_2$

are related to the effect of other possible factors like the formation of precipitates at the dislocation.  $\phi$  is the purely radial interaction potential between a Si atom ( $\phi_{\text{Si}_{\text{Ga}}^+}$ ) or a Ga vacancy ( $\phi_{\text{V}_{\text{Ga}}^{3-}}$ ) and a dislocation and simply taken as  $\phi = A/r$  with a constant  $A$  equal to  $3.5 \times 10^{-5}$  eV  $\mu\text{m}$  for  $\phi_{\text{Si}_{\text{Ga}}^+}$  or to  $4.6 \times 10^{-7}$  eV  $\mu\text{m}$  for  $\phi_{\text{V}_{\text{Ga}}^{3-}}$  [38]. The Fermi-level effect is actually considered by explicitly introducing the free-electron concentration in Eqs. (2.22) and (2.23) according to Ref. [35]. Under the assumption that the reaction in Eq. (2.19) is locally in equilibrium at the initial time, the equilibrium concentrations  $C_{\text{Si}_{\text{Ga}}^+}^{\text{eq}}$ ,  $C_{\text{V}_{\text{Ga}}^{3-}}^{\text{eq}}$ , and  $C_{(\text{Si}_{\text{Ga}}\text{V}_{\text{Ga}})^{2-}}^{\text{eq}}$  are introduced in Eq. (2.20) to determine the relationship between  $K^+$  and  $K^-$ .  $K^+$  and  $K^-$  are the reaction constants for the forward and backward reactions of Eq. (2.19).  $K^+$  is given according to the theory of Waite [39],

$$K^+ = 4\pi r_c (D_{\text{Si}_{\text{Ga}}^+} + D_{\text{V}_{\text{Ga}}^{3-}}). \quad (2.24)$$

Here  $r_c$  is the distance between  $\text{Si}_{\text{Ga}}^+$  and  $\text{V}_{\text{Ga}}^{3-}$  and was taken as  $\sqrt{2}/2 a$  ( $a$  is the lattice constant of GaAs);  $D_{\text{Si}_{\text{Ga}}^+}$  and  $D_{\text{V}_{\text{Ga}}^{3-}}$  are functions of the free-electron concentration  $n$  [40],

$$D_{\text{Si}_{\text{Ga}}^+}(n) = D_{\text{Si}_{\text{Ga}}^+}(n_i) \left( \frac{n}{n_i} \right)^3. \quad (2.25)$$

$$D_{\text{V}_{\text{Ga}}^{3-}}(n) = D_{\text{V}_{\text{Ga}}^{3-}}(n_i) \left( \frac{n}{n_i} \right)^3. \quad (2.26)$$

The free-electron concentration  $n$  is dependent on  $C_{\text{Si}_{\text{Ga}}^+}$ ,  $C_{\text{V}_{\text{Ga}}^{3-}}$ , and  $C_{(\text{Si}_{\text{Ga}}\text{V}_{\text{Ga}})^{2-}}$ , as well as on the intrinsic electron concentration  $n_i$  [29],

$$n = \frac{1}{2} \left[ \left( C_{\text{Si}_{\text{Ga}}^+} - 3C_{\text{V}_{\text{Ga}}^{3-}} - 2C_{(\text{Si}_{\text{Ga}}\text{V}_{\text{Ga}})^{2-}} \right) + \sqrt{\left( C_{\text{Si}_{\text{Ga}}^+} - 3C_{\text{V}_{\text{Ga}}^{3-}} - 2C_{(\text{Si}_{\text{Ga}}\text{V}_{\text{Ga}})^{2-}} \right)^2 + 4n_i^2} \right]. \quad (2.27)$$

Although the diffusion of silicon atoms is controlled directly by Ga vacancies, the effect of interstitial arsenic is carefully considered in the present simulations by the reaction,



This reaction was suggested to explain why an increase in the EL2 concentration related to arsenic antisite ( $\text{As}_{\text{Ga}}$ ) is accompanied by the weakening formation of arsenic precipitates [41]. Since the activation energy for the diffusion of  $\text{As}_{\text{Ga}}$  amounts to several electron volts [42], it is reasonable to assume that  $\text{As}_{\text{Ga}}$  is fixed in the simulations so that the spatial variation of its concentration from the matrix to the dislocation is constant except for the effect from the reaction in Eq. (2.28). The formation of arsenic precipitates reduces the concentration of  $\text{I}_{\text{As}}$ , so the reaction in Eq. (2.28) proceeds from the right to the left side to cause an increase in  $C_{\text{V}_{\text{Ga}}^{3-}}$ . TEM investigations of arsenic precipitates at the dislocation confirmed that the formation of arsenic precipitates is correlated with the agglomeration of gallium vacancies [44]. In order to characterize this effect, theoretically, a set of detailed equations must be constructed to describe the reaction in Eq. (2.28) in the diffusion–drift–aggregation processes. However, the diffusivity of  $\text{As}_{\text{Ga}}$  and  $\text{I}_{\text{As}}$  in n-type GaAs:Si are not available. Therefore,  $\omega_2$  is estimated roughly as

$$\omega_2 = \gamma \left( C_{\text{V}_{\text{Ga}}^{3-}} - C_{\text{V}_{\text{Ga}}^{3-}}^{\text{eq}} \right). \quad (2.29)$$

Here  $\gamma$  is an adjustable parameter to determine the rate of forming arsenic precipitates. A larger  $\omega_2$  means a higher rate of forming precipitates and thus of generating gallium vacancies due to

the formation of arsenic precipitates. The concentration of EL2 in undoped GaAs, usually in the order of  $10^{16} \text{ cm}^{-3}$  [43], is far below the doping level studied, so the effect of EL2 on the spatial distribution of point defects is neglected in the simulations. Since the actual solubility of Si in GaAs is extremely large (e.g., about  $1.0 \times 10^{20} \text{ cm}^{-3}$  at  $950^\circ \text{C}$ ) and no silicon precipitate is hence expected in the GaAs:Si samples investigated according to the classical nucleation theory [45],  $\omega_1$  is set to zero.

The parameters of the diffusion of silicon atoms mediated by gallium vacancies are available from the work by You et al [29],

$$D_{\text{Si}_{\text{Ga}}^+}(n_i, 1 \text{ atm}) = 6.77 \times 10^4 \exp\left(-\frac{3.91 \text{ eV}}{k_B T}\right) \text{ cm}^2/\text{s}, \quad (2.30)$$

$$D_{\text{V}_{\text{Ga}}^{3-}}(n_i, 1 \text{ atm}) = 9.9 \times 10^8 T^{5/8} \exp\left(-\frac{4.70 \text{ eV}}{k_B T}\right) \text{ cm}^2/\text{s}. \quad (2.31)$$

The thermal equilibrium concentration of  $\text{V}_{\text{Ga}}^{3-}$  under intrinsic and one arsenic-atmosphere-pressure conditions is

$$C_{\text{V}_{\text{Ga}}^{3-}}^{eq}(n_i, 1 \text{ atm}) = 0.293 \times C_0 T^{-5/8} \exp\left(-\frac{1.30 \text{ eV}}{k_B T}\right) \quad (2.32)$$

Here  $C_0 = 2.215 \times 10^{22} \text{ cm}^{-3}$  is the density of the gallium lattice sites. The concentration of  $(\text{Si}_{\text{Ga}} \text{V}_{\text{Ga}})^{2-}$  complexes can be deduced from reference [46],

$$C_{(\text{Si}_{\text{Ga}} \text{V}_{\text{Ga}})^{2-}}^{eq} = K_C C_{\text{Si}_{\text{Ga}}^+}^{eq} C_{\text{V}_{\text{Ga}}^{3-}}^{eq}. \quad (2.33)$$

and  $K_C$  is a factor determined by

$$K_C = \frac{Z}{N} \exp\left(\frac{E_{b,c}}{k_B T}\right). \quad (2.34)$$

where  $N = 4.43 \times 10^{22} \text{ cm}^{-3}$  is the density of total lattice sites in GaAs.  $E_{b,c}$  is the binding energy of a complex, roughly equal to the Coulomb energy between the donor and  $\text{V}_{\text{Ga}}^{3-}$ . For instance,  $E_{b,c} = 0.77 \text{ eV}$  for  $(\text{Si}_{\text{Ga}} \text{V}_{\text{Ga}})^{2-}$  in GaAs:Si, and  $E_{b,c} = 1.36 \text{ eV}$  for  $(\text{S}_{\text{As}} \text{V}_{\text{Ga}})^{2-}$  in GaAs:S.  $Z$  is the degeneracy factor of the complex, equal to the number of equivalent lattice sites forming the complex, e.g.,  $Z = 12$  for  $(\text{Si}_{\text{Ga}} \text{V}_{\text{Ga}})^{2-}$  and  $Z = 4$  for  $(\text{S}_{\text{As}} \text{V}_{\text{Ga}})^{2-}$ .

## 2.5.2 Diffusion mechanism in n-type GaAs:S

Different from the diffusion of silicon atoms in n-type GaAs:Si, sulfur atoms in GaAs:S diffuse via the kick–out mechanism [47], as shown in Fig. 2.5



where arsenic interstitial  $\text{I}_{\text{As}}$  are assumed to be neutral in the diffusion mechanism;  $i_{\text{S}}^+$  and  $\text{S}_{\text{As}}^+$  represent interstitial sulfur atoms and sulfur atoms on the arsenic lattice sites, respectively.

Since the nearest-neighbor  $(\text{S}_{\text{As}} \text{V}_{\text{Ga}})^{2-}$  complexes have been observed in GaAs:S, their effect must be incorporated into the diffusion–drift–aggregation model. A  $(\text{S}_{\text{As}} \text{V}_{\text{Ga}})^{2-}$  complex is formed by a reaction



In order to acquire information on the spatial distribution of intrinsic and extrinsic point defects,

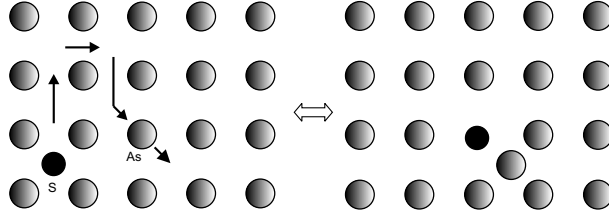


Figure 2.5: Schematic representation of the kick-out mechanism in GaAs:S.

a set of partial differential equations describing the diffusion–drift–aggregation processes of  $S_{As}^+$ ,  $I_{As}$ ,  $V_{Ga}^{3-}$ , and  $(S_{As} V_{Ga})^{2-}$  are solved numerically using the program package ZOMBIE [37],

$$K_{ko}^+ C_{i_S^+}^{eq} = K_{ko}^- C_{S_{As}^+}^{eq} C_{I_{As}}^{eq}, \quad (2.37)$$

$$K^+ C_{S_{As}^+}^{eq} C_{V_{Ga}^{3-}}^{eq} = K^- C_{(S_{As} V_{Ga})^{2-}}^{eq}, \quad (2.38)$$

$$\frac{\partial C_{(S_{As} V_{Ga})^{2-}}}{\partial t} = K^+ C_{S_{As}^+} C_{V_{Ga}^{3-}} - K^- C_{(S_{As} V_{Ga})^{2-}}, \quad (2.39)$$

$$\frac{\partial C_{V_{Ga}^{3-}}}{\partial t} = \frac{\partial}{\partial r} \left[ D_{V_{Ga}^{3-}} \left( \frac{\partial C_{V_{Ga}^{3-}}}{\partial r} - 3 \frac{C_{V_{Ga}^{3-}}}{n} \frac{\partial n}{\partial r} + \frac{C_{V_{Ga}^{3-}}}{k_B T} \frac{\partial \phi_{V_{Ga}^{3-}}}{\partial r} \right) \right] - \frac{\partial C_{(S_{As} V_{Ga})^{2-}}}{\partial t}, \quad (2.40)$$

$$\frac{\partial C_{S_{As}^+}}{\partial t} = K_{ko}^+ C_{i_S^+} - K_{ko}^- C_{S_{As}^+} C_{I_{As}} - \frac{\partial C_{(S_{As} V_{Ga})^{2-}}}{\partial t}, \quad (2.41)$$

$$\frac{\partial C_{i_S^+}}{\partial t} = \frac{\partial}{\partial r} \left( D_{i_S^+} \frac{\partial C_{i_S^+}}{\partial r} + \frac{D_{i_S^+} C_{i_S^+}}{n} \frac{\partial n}{\partial r} + \frac{D_{i_S^+} C_{i_S^+}}{k_B T} \frac{\partial \phi_S}{\partial r} \right) - \left( K_{ko}^+ C_{i_S^+} - K_{ko}^- C_{S_{As}^+} C_{I_{As}} \right) + \omega_1, \quad (2.42)$$

$$\frac{\partial C_{I_{As}}}{\partial t} = \frac{\partial}{\partial r} \left( D_{I_{As}} \frac{\partial C_{I_{As}}}{\partial r} + \frac{D_{I_{As}} C_{I_{As}}}{k_B T} \frac{\partial \phi_{As}}{\partial r} \right) + \left( K_{ko}^+ C_{i_S^+} - K_{ko}^- C_{S_{As}^+} C_{I_{As}} \right) + \omega_2. \quad (2.43)$$

$D_{i_S^+}$ ,  $D_{I_{As}}$ , and  $D_{V_{Ga}^{3-}}$  are the diffusion coefficients of  $i_S^+$ ,  $I_{As}$ , and  $V_{Ga}^{3-}$ , respectively.  $C_i$  are the instant concentrations and  $C_i^{eq}$  the local equilibrium concentrations [ $i = I_{As}$ ,  $i_S^+$ ,  $(S_{As} V_{Ga})^{2-}$ ,  $V_{Ga}^{3-}$ ,  $S_{As}^+$ ].  $\phi_j$  ( $j = S, As, V_{Ga}^{3-}$ ) is the purely radial interaction potential between a sulfur atom, an arsenic atom, or a Ga vacancy and a dislocation.  $K_{ko}^+$ ,  $K_{ko}^-$ ,  $K^+$ , and  $K^-$  are the reaction constants of the forward and backward reactions of Eqs. (2.35) and (2.36).  $K_{ko}^-$  and  $K^+$  are estimated by following the theory of Waite [39],

$$K_{ko}^- = 4\pi r_{ko} D_{I_{As}} \quad \text{and} \quad K^+ = 4\pi r_c D_{V_{Ga}^{3-}}.$$

Here, the capture radius  $r_{ko}$  is in the range of the lattice constant of GaAs;  $r_c$  is the distance between  $S_{As}^+$  and  $V_{Ga}^{3-}$  in a complex and has been taken as  $\frac{\sqrt{3}}{4}a$ . Since the diffusion of sulfur atoms is governed mainly by neutrally interstitial arsenic atoms,  $D_{i_S^+}$  is assumed to be independent of  $n$ , while  $D_{V_{Ga}^{3-}}$  is a function of  $n$ , same as in the case of n-type GaAs:Si indicated by Eq. (2.26).  $n$

depends on  $C_{S_{As}^+}$ ,  $C_{i_S^+}$ ,  $C_{V_{Ga}^{3-}}$ , and  $C_{(S_{As}V_{Ga})^{2-}}$  as well as  $n_1$ ,

$$n = \frac{1}{2} \left( C_{S_{As}^+} + C_{i_S^+} - 3C_{V_{Ga}^{3-}} - 2C_{(S_{As}V_{Ga})^{2-}} \right) + \frac{1}{2} \sqrt{\left( C_{S_{As}^+} + C_{i_S^+} - 3C_{V_{Ga}^{3-}} - 2C_{(S_{As}V_{Ga})^{2-}} \right)^2 + 4n_1^2}. \quad (2.44)$$

According to classic nucleation theory [45], nucleation and growth must occur to form a precipitate from a solid matrix. Whether a precipitate can form or not depends firstly on the total change in the free energy  $\Delta G$  for nucleation of a solid precipitation.  $\Delta G$  includes the contribution of the negative change in the volume free energy, the positive change in the interface free energy, and possible strain energy introduced when a precipitate is formed in a rigid matrix. The three terms of energies are functions of the radius of the precipitate. In order to form a stable precipitate,  $\Delta G$  must be negative. At the early stage of the nucleation and growth, the precipitate is not stable since  $\Delta G$  is positive and increases with the dimension of the precipitate up to a critical size, above which  $\Delta G$  decreases with increasing its dimension so that a stable precipitate can be formed. Therefore, the critical size corresponds to an energy barrier  $\Delta G_{max}$  that has to be overcome for forming precipitates. As a result, the nucleation rate of some atoms in a spherical precipitate with a radius  $r_0$  is [45]

$$\psi_p(r, t) = 4\pi r_0 C^2(r, t) D \exp \left[ -\frac{16}{3} \sigma^3 v^2 / (k_B T (k_B T \ln \Sigma)^2) \right]. \quad (2.45)$$

where  $\sigma$  is the interface energy between the precipitate and the matrix,  $v$  the volume per atom in the precipitate, and  $\Sigma$  the supersaturation ratio.  $D$  and  $C$  are the diffusion coefficient and the concentration of the atomic species, respectively. In order to produce precipitates,  $\Sigma$  must be larger than 1. Following the experimental observation that arsenic precipitates are formed at the dislocation,  $\omega_2$  is set simply as  $\omega_2 = -\gamma^* \psi_p(r, t)$  only within the capture radius of the dislocation, otherwise  $\omega_2 = 0$ .  $\gamma^*$  is a dimensionless parameter to adjust the rate of forming arsenic precipitates. A larger  $\gamma^*$  means a higher rate of forming precipitates.  $\omega_1$  is always set to zero because no sulfur-related precipitates are expected from the classic nucleation theory when the sulfur concentration is far below its solubility.

Since the diffusion of sulfur atoms is mediated mainly by neutrally interstitial arsenic atoms, whose concentration is independent of the Fermi level, no Fermi-level effect on the diffusivity of sulfur atoms and interstitial arsenic atoms is accounted for. However, it is essential to take the same measures as that in GaAs:Si for the Fermi-level dependence of the diffusivity of  $V_{Ga}^{3-}$ . The parameters of the diffusion of defects in GaAs:S are available from the work of Engler [48],

$$D_{I_{As}} = 5.81 \times 10^{-2} \exp \left( -\frac{2.18 \text{ eV}}{k_B T} \right) \text{ cm}^2 \text{ s}^{-1}, \quad (2.46)$$

$$C_{I_{As}}^{\text{eq}} = 2.50 \times 10^{24} \exp \left( -\frac{1.80 \text{ eV}}{k_B T} \right) \text{ cm}^{-3}, \quad (2.47)$$

$$D_{i_S^+} = 3.13 \times 10^{-4} \exp \left( -\frac{1.41 \text{ eV}}{k_B T} \right) \text{ cm}^2 \text{ s}^{-1}, \quad (2.48)$$

$$C_{i_S^+}^{\text{eq}} = C_{S_{As}^+} \cdot 6.50 \times 10^3 \exp \left( -\frac{1.60 \text{ eV}}{k_B T} \right) \text{ cm}^{-3}. \quad (2.49)$$



## 3 Experiments

In this chapter, two main experimental methods, Raman scattering and cathodoluminescence are introduced to show how dislocations and their interactions with point defects are studied and how the related electrical and optical properties of a semiconductor are deduced. An introduction to the other methods such as secondary ion mass microscopy (SIMS), transmission electron microscope (TEM), and positron annihilation technique (PAT) is omitted despite their importance in the present investigations.

### 3.1 Raman Scattering

#### 3.1.1 Fundamental principle of Raman scattering

Raman spectroscopy is based on the analysis of inelastically scattered light. Scattering occurs from optical phonons or other quasi-particles like optical magnons, plasma; even electronic excitations provide similar sources for the Raman process [49]. Macroscopically, if the frequency of the scattered photon,  $\omega_s$ , is smaller than that of the incident photon,  $\omega_i$ , the event is referred to as a Stokes process and a phonon is generated during the process. If  $\omega_s > \omega_i$ , an anti-Stokes process occurs, accompanied with the absorption of a phonon. Energy and Momentum conservation for a light-scattering process with phonon generation or absorption, as shown in Fig. 3.1, can be written as,

$$\hbar\omega_i = \hbar\omega_s \pm \hbar\Omega, \quad (3.1)$$

$$\hbar\mathbf{k}_i = \hbar\mathbf{k}_s \pm \hbar\mathbf{q}, \quad (3.2)$$

where  $\Omega$  is the frequency of a phonon.  $\mathbf{k}_i$ ,  $\mathbf{k}_s$ , and  $\mathbf{q}$  are respectively the wave vector of the incident photon, the scattered photon and the phonon. '+' means the generation of a phonon, '-' means the absorption of a phonon. For  $180^\circ$  backscattering, the maximum allowed value of the wave vector of the phonon is:  $q_{\max} = k_i + k_s \approx 2k_i$ . Since  $k_i$  is the order of  $10^6 \text{ cm}^{-1}$  in the visible and near infrared spectral range, much smaller by about two order of magnitude than the dimension of the first Brillouin zone, only the scattering at or near the center of the Brillouin zone can be accessed by the first-order Raman scattering.\*

Although the expression and diagram seem to suggest that only a phonon-photon interaction is responsible for a Raman scattering process, electrons are actually involved in the process, since the phonon-photon interaction is rather weak unless they both have comparable frequencies. When a visible photon excites Raman scattering in a semiconductor, it would firstly couple to electrons via the electron-photon interaction. Due to the interaction, the total energy of the electron system can be written as

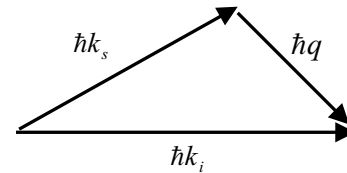


Figure 3.1: Momentum conservation for a light-scattering process with phonon generation.

\*For instance, for a He-Ne laser with the wavelength  $\lambda = 632.8 \text{ nm}$ ,  $k_i = 2\pi/\lambda = 9.9 \times 10^5 \text{ cm}^{-1}$  is far below the first Brillouin zone boundary  $\pi/a \sim 10^8 \text{ cm}^{-1}$ . Therefore, relative to the size of the first Brillouin zone,  $q \approx 0$ .

$$H = H_0 + H_{er}, \quad (3.3)$$

where  $H_0$  is the unperturbed Hamiltonian,  $H_{er}$  is a perturbation term due to the electron–photon interaction [50],

$$H_{er} = -e\mathbf{r} \cdot \mathbf{E}. \quad (3.4)$$

Here  $\mathbf{E}$  is the electric field,  $e$  the electron charge, and  $\mathbf{r}$  the distance between the electron and the phonon.

Considering the electron–photon interaction, the Raman scattering process proceeds in three steps and can be described as follows [50],

- 1.) The incident photon excites the semiconductor into an intermediate state  $|a\rangle$  by creating an electron–hole pair.
- 2.) The electron–hole pair is scattered into another state  $|b\rangle$  by emitting a phonon via the electron–phonon interaction.
- 3.) The electron–hole pair in  $|b\rangle$  recombines radiatively by emission of the scattered photon.

### 3.1.2 Selection rule

In order to obtain the first-order Raman scattering, i.e. a Raman-active vibration, the Raman tensor

$$\mathfrak{R} = (\partial\chi/\partial\mathbf{Q})_0 \hat{\mathbf{Q}}(\mathbf{q}, \Omega) \neq 0, \quad (3.5)$$

is introduced, which states that there must be a net change in the permanent dipole moment during the lattice vibration. In Eq. (3.5),  $\chi$  denotes the elastic susceptibility of the medium.  $\mathbf{Q}$  is the atomic vector displacement from an equilibrium position induced by the phonon, and  $\hat{\mathbf{Q}}$  the unit vector parallel to the phonon displacement. Raman scattering intensity  $I$  is given by

$$I \propto \left| \mathbf{e}_i \cdot (\partial\chi/\partial\mathbf{Q})_0 \hat{\mathbf{Q}}(\mathbf{q}, \Omega) \cdot \mathbf{e}_s \right|^2. \quad (3.6)$$

where  $\mathbf{e}_i$  and  $\mathbf{e}_s$  are the orientations of the polarizations of the incident and scattering lights, respectively. Therefore, if a vibration does not greatly change the polarizability, then  $\mathfrak{R}$  will be nearly zero, and the Raman intensity will be very low. Eq. (3.6) indicates that a definite Raman tensor determines whether the scattered radiation vanishes for certain choices of the scattering geometries. In the case of GaAs, it belongs to the point group  $T_d$ , whose irreducible representations  $A_1$ ,  $E$ , and  $F_2$  are Raman active. The Raman tensors in crystalline coordination (i.e.  $x - [100]$ ,  $y - [010]$ , and  $z - [001]$ ) are

$$A_1 : \begin{pmatrix} a & 0 & 0 \\ 0 & a & 0 \\ 0 & 0 & a \end{pmatrix}, E_1 : \begin{pmatrix} b+c\sqrt{3} & 0 & 0 \\ 0 & b-c\sqrt{3} & 0 \\ 0 & 0 & -2b \end{pmatrix}, E_2 : \begin{pmatrix} c-b\sqrt{3} & 0 & 0 \\ 0 & c+b\sqrt{3} & 0 \\ 0 & 0 & -2c \end{pmatrix},$$

$$F_{21} : \begin{pmatrix} 0 & 0 & 0 \\ 0 & 0 & d \\ 0 & d & 0 \end{pmatrix}, F_{22} : \begin{pmatrix} 0 & 0 & d \\ 0 & 0 & 0 \\ d & 0 & 0 \end{pmatrix}, F_{23} : \begin{pmatrix} 0 & d & 0 \\ d & 0 & 0 \\ 0 & 0 & 0 \end{pmatrix}.$$

where  $a$ ,  $b$ ,  $c$ , and  $d$  represent the linearly independent components deduced from Eq. (3.5). While the Raman tensor components  $A_1$ ,  $E_1$ , or  $E_2$  can be found in the two-phonon or the second-order Raman spectra, no optical phonon belongs to  $A_1$ ,  $E_1$  or  $E_2$  in the first-order Raman scattering of zinc-blende-type crystals such as GaAs [50]. Therefore, the Raman selection rules for the

backscattering geometry in the first-order Raman scattering of zinc-blende-type crystals are determined only by  $F_2$  and shown in Table 3.1(a), where the scattering configurations are represented as  $\mathbf{k}_i^*(\mathbf{e}_i, \mathbf{e}_s)\mathbf{k}_s^*$ , where  $\mathbf{k}_i^*$  and  $\mathbf{k}_s^*$  are the direction of the incident and scattered photons, respectively. The first-order Raman spectrum of GaAs consists of a longitudinal optic (LO) phonon at  $292\text{ cm}^{-1}$  and a transverse optic (TO) phonon at  $270\text{ cm}^{-1}$ . From the selection rule, only the LO mode is allowed in the backscattering geometry of the Raman microprobe for scattering from the (100) surface while it is prohibited for the (110) surface of GaAs. For disorder crystal or amorphous material, the selection rule is broken down.

Scattering geometry	Selection rule	
	TO phonon	LO phonon
(100) surface:		
$x(y, y)\bar{x}, x(z, z)\bar{x}$	0	0
$x(y, z)\bar{x}, x(z, y)\bar{x}$	0	$ d_{LO} ^2$
$x(y', z')\bar{x}, x(z', y')\bar{x}$	0	0
$x(y', y')\bar{x}, x(z', z')\bar{x}$	0	$ d_{LO} ^2$
(110) surface:		
$y'(x, x)\bar{y}'$	0	0
$y'(z', x)\bar{y}'$	$ d_{LO} ^2$	0
$y'(z', z')\bar{y}'$	$ d_{LO} ^2$	0
(111) surface:		
$x''(z'', z'')\bar{x}''$	$\frac{2}{3} d_{LO} ^2$	$\frac{1}{3} d_{LO} ^2$
$x''(z'', y'')\bar{x}''$	$\frac{2}{3} d_{LO} ^2$	0

Table 3.1: (a) Raman selection rules for backscattering geometries in zinc-blende-type crystal. Here,  $x = [100], y = [010], z = [001], y' = [110], z' = [0\bar{1}1], x'' = [111], y'' = [1\bar{1}0], z'' = [11\bar{2}]$ . The scattering configurations are represented as  $\mathbf{k}_i^*(\mathbf{e}_i, \mathbf{e}_s)\mathbf{k}_s^*$ , where  $\mathbf{k}_i^*$  and  $\mathbf{k}_s^*$  are the direction of the incident and scattering photons; and  $\mathbf{e}_i$  and  $\mathbf{e}_s$  are the orientations of the polarizations of the incident and scattering photons, respectively. (b) The first-order phonon modes in wurtzite GaN.

Symmetry	Active in	Raman Shift (cm <sup>-1</sup> )
E <sub>2</sub> low	Raman	144
A <sub>1</sub> (TO)	Raman, IR	533
E <sub>1</sub> (TO)	Raman, IR	561
E <sub>2</sub> high	Raman	569
A <sub>1</sub> (LO)	Raman, IR	735
E <sub>1</sub> (LO)	Raman, IR	743
B <sub>1</sub> low	silent	
B <sub>1</sub> high	silent	

Cubic GaN has a zinc-blende structure and belongs to the point group  $T_d$ , so the optical modes seen by the first-order Raman scattering are similar to GaAs, and comprise a doubly degenerate TO ( $552\text{ cm}^{-1}$ ) and a single LO phonon ( $740\text{ cm}^{-1}$ ). Wurtzite GaN belongs to the point group  $C_{6v}$ , having four atoms per unit cell. Group theory predicts eight sets of phonon modes in the first-order Raman scattering [see Tab. 3.1(b)] [51].

### 3.1.3 Electric effects

The Raman bands are sensitive to the bond length or inter-atomic spacing and can thus be associated with strain/stress in the crystal. A blue shift of the Raman frequency may be associated with a compressive stress, and a red shift with a tensile stress [52]. In semiconductors, the free-carrier concentration can change some Raman bands with respect of linewidth and intensity [53].

In highly doped polar semiconductors, the coupling between the LO phonons and plasma via the macroscopic electric fields splits the LO mode into two branches,  $L^-$  and  $L^+$ , which can inversely be applied to determine the free-carrier concentration from Raman scattering. In the presence of the free carriers, the total dielectric function of the semiconductor with the phonon frequency  $\omega$  is given by [54]

$$\varepsilon(\omega) = \varepsilon_\infty \left( 1 + \frac{\omega_{LO}^2 - \omega_{TO}^2}{\omega_{TO}^2 - \omega^2} - \frac{\omega_p^2}{\omega^2} \right). \quad (3.7)$$

By solving the equation  $\varepsilon(\omega) = 0$ , two LO phonon–plasmon coupled modes,  $\omega_{L^+}$  and  $\omega_{L^-}$ , can be obtained

$$\omega_{L^+}^2 = \frac{1}{2}(\omega_{LO}^2 + \omega_p^2(q)) + \frac{1}{2}[(\omega_{LO}^2 + \omega_p^2(q))^2 - 4\omega_p^2(q)\omega_{TO}^2]^{1/2}, \quad (3.8)$$

$$\omega_{L^-}^2 = \frac{1}{2}(\omega_{LO}^2 + \omega_p^2(q)) - \frac{1}{2}[(\omega_{LO}^2 + \omega_p^2(q))^2 - 4\omega_p^2(q)\omega_{TO}^2]^{1/2}, \quad (3.9)$$

$$\omega_p^2(q) = ne^2/m^* \varepsilon_0 \varepsilon_\infty + \frac{3}{5}q^2 \vartheta_f^2. \quad (3.10)$$

Here  $\omega_{LO}$  and  $\omega_{TO}$  are the LO and TO phonon frequencies, respectively.  $\omega_p(q)$  is the plasmon frequency, depending on  $n$  and the wave vector  $q$  of phonons.\*  $\varepsilon_\infty$  is the high-frequency dielectric constant, and  $\varepsilon_0$  is the vacuum dielectric constant,  $m^*$  the electron or hole effective mass.  $\vartheta_f$  is the Fermi velocity [55],

$$\vartheta_f = \frac{\hbar}{m^*} (3\pi^2 n)^{1/3}. \quad (3.11)$$

The second term in Eq. (3.10) arises from nonlocal effects due to the noncompressibility of the

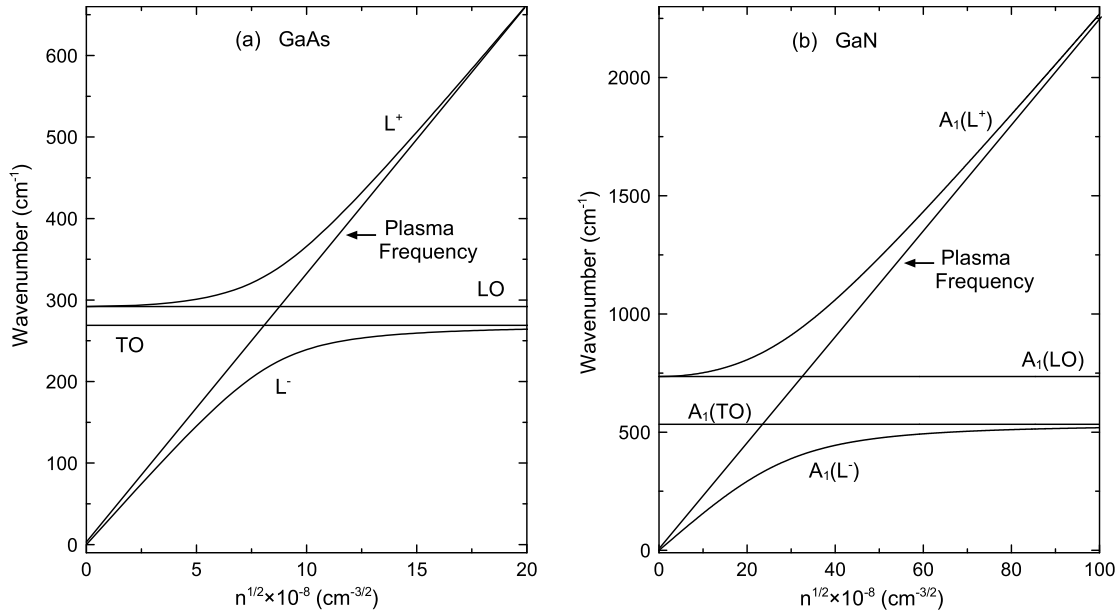


Figure 3.2: Raman frequencies of the coupled plasmon–phonon modes in (a) n-type GaAs and (b) n-type GaN as a function of the free-electron concentration  $n$ .

\*  $\omega_p$  from Eq. (3.10) is actually the angular vibrational frequency of plasma,  $\omega_p = 2\pi\nu_p$  and  $\nu_p$  the clock frequency of plasma. In most Raman spectra, a phonon frequency is generally represented by its wave number; correspondingly, the relationship between the wave number of plasma ( $1/\lambda_p$ ) and  $\omega_p$  is:  $\omega_p = 2\pi c/\lambda_p$ .  $c$  is the light velocity in vacuum.

system [55]. For a low wave vector  $q$ , this term is negligible. The plasmon–phonon coupled modes in GaAs and in GaN were calculated from Eqs. (3.8), (3.9) and (3.10) as a function of the free-carrier concentration and are shown in Fig. 3.2.

Since the LO mode observed arises from the surface top layer, which is carrier depleted while  $L^-$  and  $L^+$  is excited in the bulk region beneath the surface, it is possible to determine the carrier depletion depth or the carrier concentration near the surface by comparing the intensities of the LO and  $L^-$  Raman modes. The intensities of LO and  $L^-$  are governed by the following relationships [55]

$$I(LO) = I_0(LO)(1 - e^{-2\alpha d}), \quad (3.12)$$

$$I(L^-) = I_0(L^-)e^{-2\alpha d}. \quad (3.13)$$

where  $I_0(LO)$  and  $I_0(L^-)$  are the intensities of LO and  $L^-$  in semi-insulating material and heavily doped material with negligible space charge region, respectively. For GaAs,  $I_0(LO)/I_0(L^-)$  is equal to 2.65 [55].  $\alpha$  is the adsorption coefficient for Raman probe light, depending on its wavelength.  $d$  is the surface depletion depth given by

$$d = (2\varepsilon_0\varepsilon_r\Phi_B/e^2n)^{1/2}, \quad (3.14)$$

where  $\Phi_B$  is the built-in surface potential (for GaAs, 0.8 eV) and  $\varepsilon_r$  the static dielectric constant. According to Eqs. (3.12) and (3.13), the ratio between LO and  $L^-$  is

$$I(LO)/I(L^-) = (I_0(LO)/I_0(L^-))(e^{2\alpha d} - 1), \quad (3.15)$$

which allows the estimation of the depletion depth or thus the free-carrier concentration near the surface.

### 3.1.4 Constituents of Raman spectroscopy

An integrated Raman system, LABRAM from the Dilor company, was used in the present studies. The basic parameters of the LABRAM Raman microscope are listed in the following:

- Laser: He–Ne, 20 mW, polarized 500 : 1, wavelength 632.817 nm,
- Confocal hole: 0–1500  $\mu\text{m}$ ; CCD detector with the detection range from 400–1100 nm,
- $z$  resolution:  $\sim 1 \mu\text{m}$ ;  $xy$  resolution:  $< 0.5 \mu\text{m}$ ,
- Spectral resolution:  $< 1 \text{ cm}^{-1}$ .

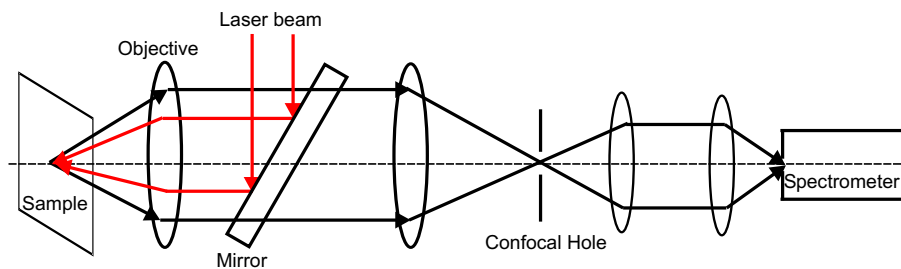


Figure 3.3: Schematic principle diagram of the proceeding of information in Raman spectroscopy.

The principle diagram of the Raman microscope is schematically shown in Fig. 3.3. The confocal hole is actually limiting the region of the sample where the signal is collected from. By using the confocal hole, the analyzed surface is specially defined with the precision down to 0.1  $\mu\text{m}$  at

best and adjustable; and the depth of focus is reduced to about 1  $\mu\text{m}$ . As a result, the contrast in a collected image is increased and the back scattered light is minimized. In general, there are three sorts of resolutions for an optical microscope:

- 1.)  $z$  resolution (depth discrimination)

$$\Delta Z = \frac{R_I \lambda}{4 \cdot NA^2},$$

- 2.)  $xy$  resolution

$$\Delta R = \frac{0.61 \lambda}{NA},$$

- 3.) Spectral resolution

$$\Delta \omega [cm^{-1}] = \frac{10^7}{\lambda^2 [nm]} \Delta \lambda [nm] \text{ and } \Delta \lambda = \frac{\lambda}{m_s N_g}.$$

$R_I$  is the refraction index,  $NA$  the numerical aperture of the objective,  $N_g$  the number of the gratings, and  $m_s$  is the order of the spectrum. In the case of our equipment, the spectral resolution is typically  $1 \text{ cm}^{-1}$ .

## 3.2 Cathodoluminescence (CL)

### 3.2.1 Fundamental principle of CL

Cathodoluminescence is the emission of light under electron bombardment. In general, it results from the radiative recombination of non-equilibrium charge carriers like electron–hole pairs excited by the incident electron beam. In semiconductors, the luminescence can be achieved by several radiative transitions between the conduction band ( $E_c$ ), the valence band ( $E_v$ ), exciton ( $E_e$ ), donor ( $E_d$ ), and acceptor ( $E_a$ ) levels, as shown in Fig. 3.4. Sometimes, the radiative transitions are accompanied by non-radiative processes due to, e.g., the Auger effect or emissions of phonons. The energy of an emitted photon equals the difference between the initial and final energy levels of an excess electrons minus the energy of possibly emitted phonons accompanying the process of the emission of the photons. In particular, for the donor–acceptor pair recombination, the energy of an emitted photon depends further on the pair separation [56],

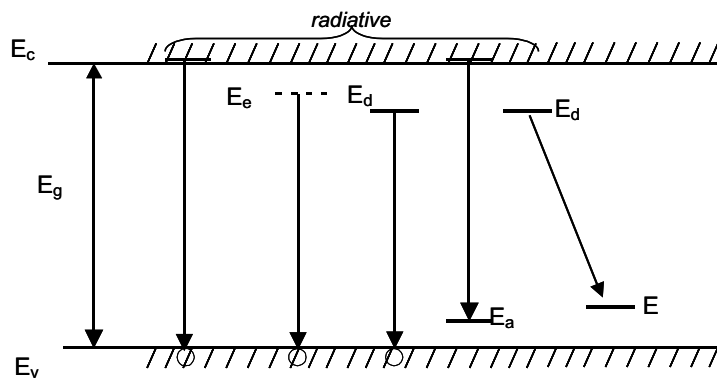


Figure 3.4: Schematic diagram of radiative recombination processes of electron–hole pairs between the conduction band ( $E_c$ ), the valence band ( $E_v$ ), exciton ( $E_e$ ), donor ( $E_d$ ), and acceptor ( $E_a$ ) levels in a semiconductor.

$$h\nu = E_g - E_d - E_a - mE_{ph} + e^2/4\pi\epsilon_0\epsilon r. \quad (3.16)$$

where  $m$  is the number of the emitted phonons with an energy of  $E_{ph}$ , and  $r$  the donor–acceptor pair separation.

In principle, the CL intensity with an energy  $h\nu$  collected by an ideal spectrometer can be mathematically calculated by the integral of the radiative recombination over the volume  $V$  excited by the incident electron beam [57],

$$I_{CL}(h\nu) = Q(h\nu) \int_0^\Theta \sin\Theta d\Theta \int_V d^3r \frac{\tau_e}{\tau_{rad}} \Delta n(r) \exp\left(\frac{\alpha(h\nu)z}{\cos\Theta}\right), \quad (3.17)$$

where  $Q(h\nu)$  is the quantum efficiency of the detector,  $\Theta$  the 3D angle within which the emitted photons can enter the detector,  $\alpha(h\nu)$  the optical absorption coefficient, and  $z$  the incident depth of the electron beam.  $\tau_e$  is the effective lifetime of excess minority carriers,  $\tau_{rad}$  their radiative lifetime, and  $\Delta n(r)$  the density of the electron–hole pairs (excess minority carriers) available to recombination. Eq. (3.17) states that the CL intensity is proportional to  $\Delta n(r)$  and to the ratio of  $\tau_e$  to  $\tau_{rad}$ . Since dislocations are centers with high non-radiative recombination rate,  $\tau_e$  at a dislocation can be calculated by

$$\frac{1}{\tau_e} = \begin{cases} \frac{1}{\tau_{rad}} + \frac{1}{\tau_{nonrad}} & (\text{beyond the dislocation core, i.e. } r > r_0), \\ \frac{1}{\tau_{rad}} + \frac{1}{\tau_{nonrad}} + \frac{1}{\tau_{dislocation}} & (\text{within the dislocation core, i.e. } r < r_0). \end{cases} \quad (3.18)$$

$\tau_{dislocation}$  is the non-radiative lifetime of excess minority carriers associated with dislocations,  $\tau_{nonrad}$  the non-radiative lifetime through the other recombination centers.  $\Delta n$  near a dislocation can be expressed as [58–60]

$$\Delta n(r) = g_r \tau_e [1 - \exp(-r/L_e)], \quad (3.19)$$

where  $g_r$  is the generation rate of the minority carriers, depending on the the electron beam energy  $E_{beam}$  and current  $I_{beam}$ , as well as the ionization energy  $E_i$  (i.e., the energy required for the formation of an electron-hole pair):  $g_r = E_{beam} I_{beam} (1 - \eta_f) / eE_i$ .  $\eta_f$  represents the fractional electron-beam-energy loss due to backscattered electrons [56].  $r$  is the distance from the dislocation,  $L_e = \sqrt{D\tau_e}$  the effective diffusion length of the minority carriers, and  $D$  their diffusion coefficient. If it is assumed that the probability for the recombination of an electron–hole pair through a certain recombination path  $p$  is  $\zeta_p$ , an expression such as

$$I_p \propto \begin{cases} \zeta_p C_p \frac{\tau_e}{\tau_{rad}} \Delta n(r); & (r > r_0), \\ 0; & (r < r_0). \end{cases} \quad (3.20)$$

can be given. Here  $C_p$  is the density of transition paths  $p$ . Since dislocations are widely assumed to be non-radiative recombination centers, almost no luminescence appear at the dislocation core, i.e.  $I_p \approx 0$ . Particularly for shallow-level-donor doping in GaAs, Eq. (3.20) is valid only when the concentration of the shallow-level donors is below its solubility limit, above which the luminescence intensity decreases with increasing dopant concentration because of the formation of dopant-related precipitates acting as non-radiative centers [61, 62].

### 3.2.2 Effect of external conditions on CL spectra

Since CL spectra are connected to the band gap or to the energy levels in the band gap, any variation of these levels must have an important influence on a luminescence band in the CL spectra.

The intensity and peak position of a luminescence band depend on several external parameters, such as temperature, pressure and the free-carrier concentration. Therefore, by monitoring the energy positions of the luminescence bands in the CL spectra, the information on the influence of temperature, pressure and the free-carrier concentration on the band gap and the energy levels in the band gaps can be obtained. As well known, the band gap becomes narrower to result in a red shift of the band-to-band luminescence with increasing temperature.

Some studies have found that the band gap or the defect-related luminescence bands become wider and shift up to a higher-energy position with increasing pressure. As an example, Fig. 3.5 displays the band gap and the yellow luminescence (YL) band in GaN as a function of pressure.

As pointed out by Sernelius [65], there are three possible kinds of near band gaps contributing to the near-band-edge (NBE) transitions in doped semiconductors: the first band gap  $E_{g,1}$  is the distance in energy from the bottom of the conduction band to the top of the valence band. The second band gap  $E_{g,2}$  means the energy distance between a shallow-level donor state (or the bottom of the conduction band) and the top of the valence band (or a shallow-level acceptor state). Finally,  $E_{g,3}$  denotes the energy difference between a shallow-level donor and a shallow-level acceptor states if the vertically optical transition between them is allowed. Given the unperturbed band gap is  $E_g$ , the band-gap shift is defined as

$$\Delta E_{g,i} = E_{g,i} - E_g, \quad i = 1, 2, 3 \quad (3.21)$$

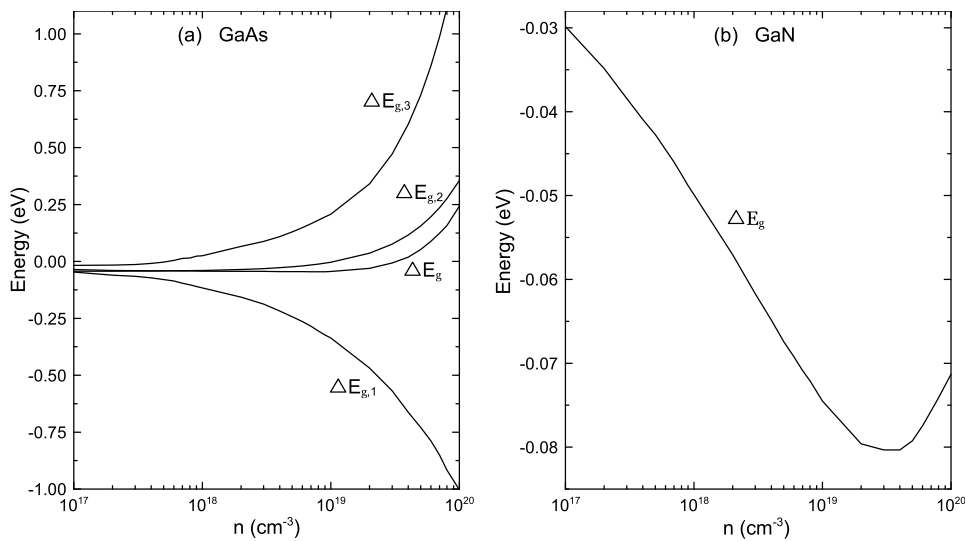


Figure 3.6: Calculated band-gap shift of (a) GaAs and (b) GaN as a function of the free-carrier concentration. The data on GaAs are taken from Ref. [65] and on GaN from Ref. [66].

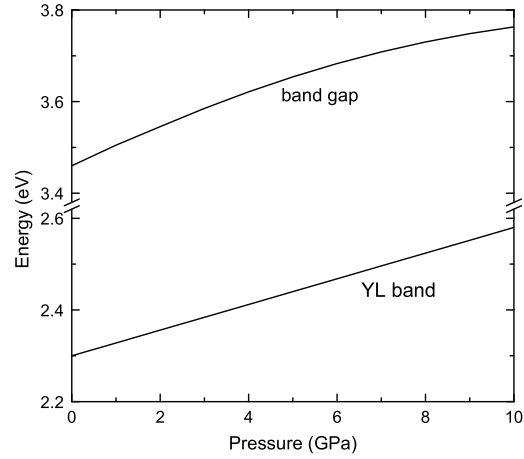


Figure 3.5: The hydrostatic pressure dependence of the band gap and the yellow luminescence (YL) band in GaN at 300 K. The data on the band gap and the YL band are taken from Refs. [63] and [64], respectively.

In heavily doped semiconductors, where donor or acceptor states enter the conduction or the valence band,  $\Delta E_{g,3}$  equals the so-called Burstein–Moss shift when no interactions are present between electrons (holes) and ions, i.e.  $\Delta E_{g,3}$  increases with the free-carrier concentration [65]. The various band gaps in GaAs are shown in Fig. 3.6(a) as a function of the free-carrier concentration. On average, the total band-gap shift  $\Delta E_g = (\Delta E_{g,1} + \Delta E_{g,2} + \Delta E_{g,3})/3$  decreases firstly with the free-carrier concentration up to about  $2.0 \times 10^{19} \text{ cm}^{-3}$ , above which it increases with the free-carrier concentration, similar to the case in GaN [compare (a) and (b) in Fig. 3.6].

The present CL investigations were carried out on a JSM 6400 or a BS 300 scanning electron microscope (SEM). A photomultiplier, a germanium (Ge), or a charge coupled device (CCD) detector and a computer-controlled monochromator were used to process the corresponding CL images or spectra. It is sometimes necessary to correct the spectra obtained by cathodoluminescence microscopy according to the quantum efficiency of the detector used in order to determine accurately the energy position and the intensity of a luminescence band. The range of the detected wavelengths depends on the type of the detectors. The effective wavelength detected by a Ge detector ranges from 800 nm to 1800 nm. The CCD used at present is front illuminated CCDs with the effective range of the detected wavelengths from 400 to 1100 nm. The efficiencies of the Ge and the CCD detectors as a function of the wavelength are shown in Fig. 3.7.

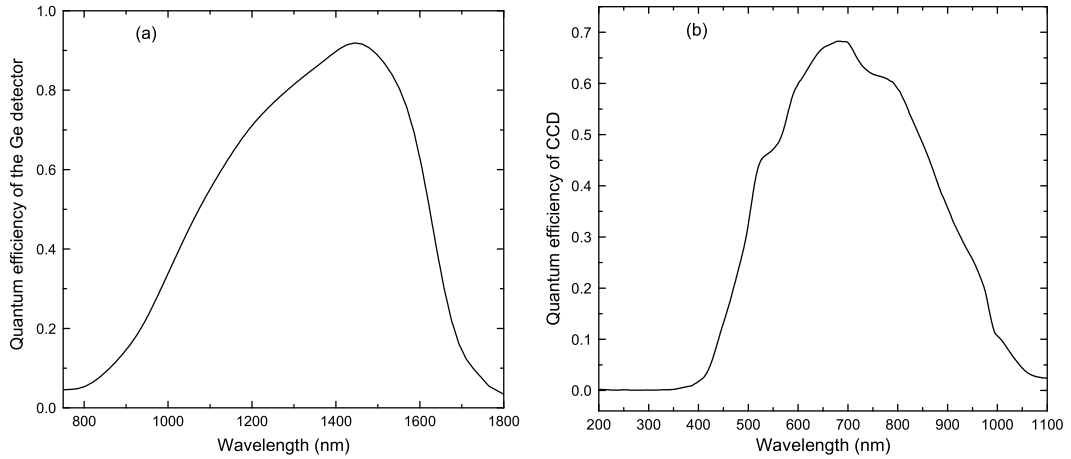


Figure 3.7: Quantum efficiency of (a) the Ge detector and (b) the CCD used as a function of the wavelength



## 4 Interactions of Point Defects with Dislocations in GaAs:Si

A dislocation is well known as a sink of point defects so that a point-defect atmosphere is formed at the dislocation. This point-defect atmosphere result in an inhomogeneous distribution of the electrical and optical properties of the material. Although extensively experimental investigations have been performed, there are still some issues to need clarifying further. For example, the reduction in the concentration of  $\text{Si}_{\text{As}}^-$  ( $\text{Te}_{\text{As}}^+$ ) acting as acceptors (donors) has recently been suggested to explain the significant increase (decrease) in the free-electron concentration from the matrix to the dislocations in n-type GaAs:Si (Te) [44, 67]. However, the explanation is problematic especially for n-type GaAs:Si, since the  $\text{Si}_{\text{As}}^-$  concentration in n-type GaAs:Si is much low compared to the  $\text{Si}_{\text{Ga}}^+$  concentration so that the reduction in the  $\text{Si}_{\text{As}}^-$  concentration cannot vary drastically the spatial distribution of the free-electron concentration. Moreover, there are various point defects acting as acceptors or donors in doped GaAs, whose concentrations must increase or decrease with the distance from the dislocation. Therefore, the variation in the free-electron concentration must be determined from total change in the concentrations of various point defects, not simply by one kind of point defects such as  $\text{Si}_{\text{As}}^-$  ( $\text{Te}_{\text{As}}^+$ ). In fact, the conclusion mentioned above conflicts with the experimental observations of n-type GaAs:S as shown later, where sulfur, similar to Te, occupies the arsenic site and the free-electron concentration increases from the matrix to the dislocation, in contrast to GaAs:Te. On the other hand, defect complexes have attracted a long-term attention due to their technological and scientific interest. Investigations have found that donors at arsenic lattice sites like  $\text{Te}_{\text{As}}^+$  in GaAs:Te and in GaAs:S or at gallium sites like  $\text{Si}_{\text{Ga}}^+$  in n-type GaAs:Si are combined with gallium vacancies to form nearest-neighbor or second-nearest-neighbor complexes [68–71]. However, the effect of dislocations on the complexes have hardly been studied. In particular, although arsenic precipitates were observed to be frequently formed at dislocations in GaAs doped with Cr, O, Si and Zn [67, 72], it is not still clear to what extent they can influence the spatial distribution of point defects and of the free-electron concentration.

### 4.1 Experimental methods

Samples of n-type Si doped GaAs(100) with about  $1.0 \times 10^{18}$  silicon atoms/cm<sup>3</sup> were grown by vertical gradient freezing (VGF) technique under arsenic-rich environment. The dislocation density is about  $10^4$  cm<sup>-2</sup>. Prior to the experimental observation and characterization, the samples were mechano-chemically polished to obtain smooth and clean sample surfaces. Then they were photoetched by a photo-assisted diluted sirtl-like (DSL) technique to reveal the dislocations at the surface [73]. The solution used for DSL is HF (with a concentration of 48%):CrO<sub>3</sub> (with a concentration of 33%):H<sub>2</sub>O=1 : 1 : 8 in volume. The etching of GaAs in the DSL solution occurs by a mechanism of oxidative dissolution of a GaAs molecule that requires six holes h<sup>+</sup>,



The holes are initially supplied by the etching solutions. The etching velocity is largely enhanced by illuminating the sample with light. Then the dissolution of the GaAs molecules is mostly due

to the holes generated by light inside the sample and reaching the sample surface. The density of holes at the sample surface depends on the band bending at the interface between GaAs and the etching solution according to

$$p_s = (p_0 + p_{scr} + p_b) \exp(-eV_{sc}/k_B T), \quad (4.2)$$

where  $p_0$  is the equilibrium density of the holes in the bulk,  $p_{scr}$  the density of the holes photo-generated in the surface space charge region,  $p_b$  the density of the holes photogenerated in the bulk and reaching the sample surface, and  $V_{sc}$  the surface band bending potential [see Fig. 4.1(a)]. Given a dislocation recombines holes, reducing the hole density, the etching rate is lower and the dislocation appears as a hillock. Similarly, the higher doping level in n-type GaAs, i.e. the higher free-electron density ( $n$ ) suppresses the hole density ( $p$ ) by the relation  $np=n_i^2$  to reduce the etching rate. Therefore, an etch hillock (depression) at the smooth surface of an n-type GaAs sample corresponds to an increased (decreased) free-electron concentration in the vicinity of dislocations. In Fig. 4.1(b) is an example of a dislocation in GaAs:Si revealed by the DSL technique.

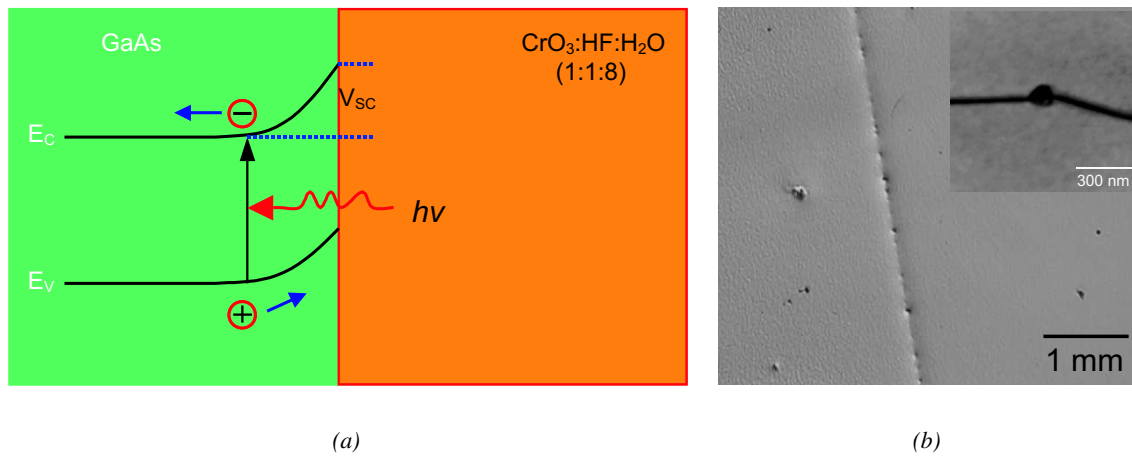


Figure 4.1: (a) Sketch of the DSL etching mechanism of GaAs. (b) Light microscopy image of a dislocation line in GaAs:Si revealed by DSL etching; the dislocation is decorated by arsenic precipitates appearing as dots along the dislocation line. In the inset of (b), a TEM image shows an arsenic precipitate on the dislocation line.

In addition to the DSL technique, etching of GaAs in molten KOH is also regarded as the reliable and unambiguous method for revealing dislocations on the (100) surface of GaAs [74]. However, it is not suitable to reveal changes in the free-carrier concentration or the decoration of dislocations with precipitates. Although the A/B etchant has been applied to reveal dislocations on the surface, it has not been convincing, since this procedure is usually accompanied with the production of ridges and grooves [75].

After DSL etching, the samples were transferred to the Raman and SEM-CL microscopes to acquire the relevant information. All Raman spectra were recorded in backscattering geometry at room temperature. The samples were further observed in the secondary electron (SE) and cathodoluminescence (CL) modes in a JSM 6400 scanning electron microscope (SEM) equipped with an Oxford monochromatic CL system at a temperature of 75 K. A 20 keV electron beam was selected to excite the samples.

## 4.2 Results and discussion

In Fig. 4.2(a), a high-intensity TO-like mode can be observed at about  $263\text{ cm}^{-1}$ . The fact that the weak LO mode contrasts with the strong TO-like peak seems in contrast to the general selection rule, according to which only the LO mode is Raman active for the GaAs(100) surface. The x-ray diffraction indicates that the surface of GaAs is indeed (100). To confirm these measurements, another Raman scattering study on semi-insulating GaAs(100) has been made to show a good agreement with the selection rule, i.e. only the LO phonon can be observed in the backscattering geometry. The appearance of the TO-like peak can thus be attributed to the doping effect, in which the LO mode is split into two submodes: a low frequency branch  $L^-$  and a high frequency one  $L^+$  introduced by the phonon-plasmon coupling (see Sec. 3.1.3). Therefore, the contribution to the TO-like peak comes mainly from the  $L^-$  mode. Fig. 4.2(a) shows further that the  $L^+$  peak at the dislocation is at a higher frequency than that in the matrix, which implies a higher free-electron

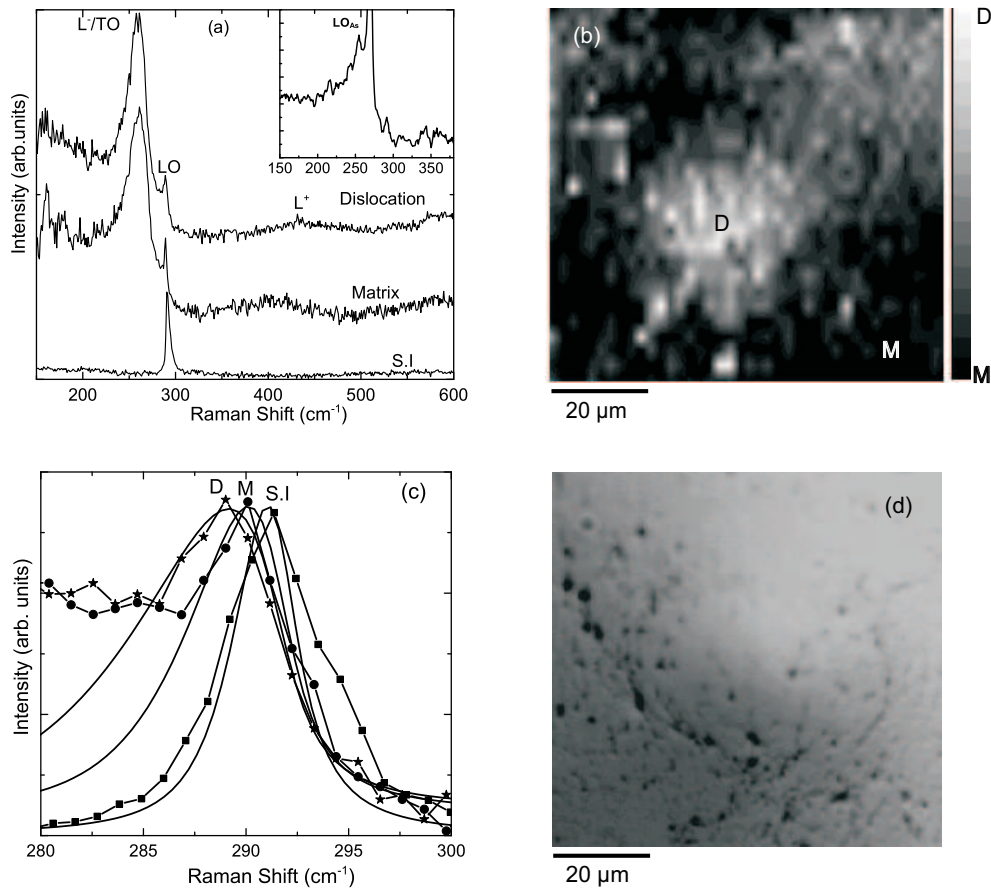


*Figure 4.2:* (a) Raman spectra in the matrix of semi-insulating (S.I) GaAs(100), of GaAs(100):Si, and around the dislocation in GaAs:Si; in the inset is shown a typical spectrum detected at a dislocation exhibiting arsenic precipitates. The Raman intensities at low frequencies below  $285\text{ cm}^{-1}$  for GaAs:Si are pronouncedly lifted due to the strong noise. (b) A map of the spatial distribution of the free-electron concentration from the matrix [M:  $n = (9.70 \pm 0.50) \times 10^{17}\text{ cm}^{-3}$ ] to the dislocation [D:  $n = (1.15 \pm 0.35) \times 10^{18}\text{ cm}^{-3}$ ]. (c) The fitted LO peak (smooth curve) according to the Raman correlation model. For comparison, experimental data are also plotted (curve+symbol). The two peaks obtained by fitting and experiment on the right are related to semi-insulating GaAs (S.I), the peaks in the middle to the matrix (M) and the ones on the left to the dislocation (D) in GaAs:Si. (d) A light microscopy image around the dislocation in GaAs:Si, appearing as a hillock after etching. The position is the same as in (b).

concentration at the dislocation than in the matrix. By calculating the ratio of the integrated intensity of the  $L^-$  to the LO peak [55] or the position of the  $L^+$  peak [76] (also see Sec. 3.1.3), the free-electron concentration can be obtained as  $9.5 \times 10^{17} \text{ cm}^{-3}$  in the matrix and increases from the matrix to the dislocation [Fig. 4.2(b)]. Additionally, the inset of Fig. 4.2(a) displays a Raman peak at the spectral position of  $257 \text{ cm}^{-1}$  occasionally detected at the dislocations, which has been assigned to the LO mode of rhombohedral arsenic precipitates [67]. The TO mode of arsenic precipitates cannot be found in the present Raman spectra possibly due to the strong noise there.

The detailed examination of the LO peak in Fig. 4.2(a) indicates that this peak shifts down by  $1.5 \text{ cm}^{-1}$  in the matrix and  $2.5 \text{ cm}^{-1}$  at the dislocation in GaAs:Si compared to that for semi-insulating GaAs. Although the feature has been observed in p-type GaAs (e.g. GaAs:Zn [53] and GaAs:Be [77]), it has usually been overlooked in the case of n-type GaAs. A negative frequency shift would imply the existence of tensile strain. If a conversion factor of  $0.0034 \text{ cm}$  from the Raman shift to the strain is applied [78], a strain of  $0.51\%$  in the matrix and of  $0.80\%$  at the dislocation would be achieved. Although early experiments have found that the lattice constant of GaAs increases linearly with the silicon concentration at a rate of  $2.0 \times 10^{-24} \text{ nm/cm}^{-3}$  when the free-electron concentration is below  $2.0 \times 10^{18} \text{ cm}^{-3}$  [79], a tensile strain based on this relationship is too small to explain the pronounced shift of the LO peak. There are thus other factors responsible for the negative frequency shift. It is well known that only single phonons near the center of the Brillouin zone (wave vector  $q \approx 0$ ) can contribute to the Raman spectra in an infinite crystal because the momentum of phonons and photons must be conserved. However, phonons can be confined in defects in a real crystal, which results in non-conserved momenta and thus allows phonons with  $q \neq 0$  to contribute to the Raman spectra [80]. As a result, the line shape of Raman spectra may be broadened and asymmetric. Considering this, a so-called spatial correlation model was constructed [80]. According to this model, the Raman line shapes can be calculated by superimposing Lorentzian curves centered at  $\omega(q)$ , weighted by the wave-vector uncertainty caused by the defects [80],

$$I(\omega) \propto \int_0^1 \frac{\exp(-q^2 L^2/4) 4\pi q^2 dq}{[\omega - \omega(q)]^2 + (\Gamma_0/2)^2}, \quad (4.3)$$

where the wave vector  $q$  is in units of  $2\pi/a$ ,  $L$  the correlation length in unit of  $a$ , and  $\Gamma_0 = 3.0 \text{ cm}^{-1}$  the natural full width at half maximum (FWHM) of the intrinsic line shape of the defect-free material at room temperature [80]. The phonon dispersion curve  $\omega(q)$  of the LO phonon in GaAs was taken as [80]

$$\omega(q) = A + \{A^2 - B[1 - \cos(\pi q)]\}^{1/2} \quad (4.4)$$

with  $A = 4.26 \times 10^4 \text{ cm}^{-2}$  and  $B = 7.11 \times 10^8 \text{ cm}^{-4}$ .

Fig. 4.2(c) shows the Raman line shape of the LO modes fitted by Eqs. (4.3) and (4.4), which exhibit a reasonable agreement with experimental results. Therefore, the negative frequency shift originates probably from an enhanced wave-vector nonconservation scattering induced by some defects to imply the aggregation of the defects around the dislocation [53].

Panchromatic CL images over a wavelength range from 400 to 900 nm were acquired by a photomultiplier [Fig. 4.3(a)]. The image exhibits dark dots corresponding to the dislocations, as non-radiative recombination centers, contrasting the bright surrounding. Similarly, Fig. 4.3(c) displays another panchromatic CL image for the same spatial region obtained with a Ge detector, whose sensitivity range is from 800 to 1600 nm, exhibiting the same trend for the CL intensity as Fig. 4.3(a), i.e. the total CL intensity decreases from the matrix to the dislocation. In addition to the near-band-edge (NBE) transitions, two more peaks at 940 nm (1.33 eV) and at 1080 nm

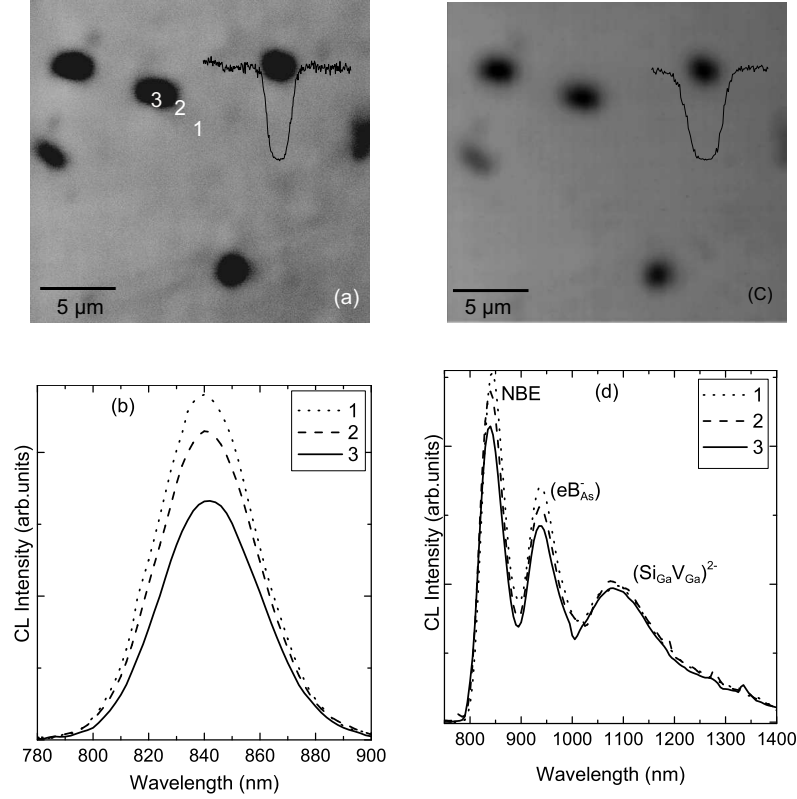


Figure 4.3: (a) A panchromatic CL image taken by the photomultiplier, whose effective detection range is from 400 to 900 nm, so the image comes mainly from the near-band-edge emission [see (b)]. (c) Correspondingly, a panchromatic CL image detected by the Ge detector, whose effective detection range is from 800 to 1600 nm, so the image comes from the NBE, the  $(eB_{As}^-)$  and the  $(Si_{Ga}V_{Ga})^{2-}$  transitions [see (d)]. (b) and (d) CL spectra of GaAs(100) at 75 K taken from points 1 to 3 marked in (a) by the photomultiplier and by the Ge detector, respectively. The spectra have not been corrected by the sensitivity curves of the detectors.

(1.15 eV) have been measured in the CL spectra [Fig. 4.3(d)]. The 1.15 eV band has been identified as the transitions within  $(Si_{Ga}V_{Ga})^{2-}$  complexes [68], while the 1.33 eV band is believed to be due to the recombination from the states near the conduction band, to the acceptor  $B_{As}^-$  states, i.e.  $(eB_{As}^-)$  [82]. Therefore, as indicated in Figs. 4.3(b) and (d), the CL images in Figs. 4.3(a) and (c) are connected to the NBE, the  $B_{As}^-$  acceptor-related, and the  $(Si_{Ga}V_{Ga})^{2-}$ -complex-related emissions, respectively. The  $(Si_{Ga}V_{Ga})$  complex is believed to have a double negative charge state because the previous studies showed that  $V_{Ga}^{3-}$  is the most favorable state of a gallium vacancy in n-type GaAs:Si [35] [81]. In Chapter 6, it will be confirmed that a gallium vacancy is triply charged, especially at a high doping level. Fig. 4.3(b) shows that the NBE band lies at 840 nm (1.47 eV), indicating a red shift from 820 nm (1.51 eV) in semi-insulating GaAs at 75 K due to the doping effect and possibly a higher concentration of  $B_{As}^0$  acceptors. Boron is contributed by the encapsulant (boron oxide) during crystal growth of GaAs. A boron atom may form a neutral acceptor ( $B_{As}^0$ ) or a singly charged one ( $B_{As}^-$ ). The energy level of  $B_{As}^0$  and  $B_{As}^-$  is expected to be respectively around 71 meV and 188 meV above the valence band maximum [114, 115]. The transitions from the states near the conduction band to  $B_{As}^0$  states contribute to the NBE band while the  $eB_{As}^-$  transitions result in the 1.33 eV luminescence band.

Eq. (3.18) states that  $\tau_e/\tau_{rad}$  is not larger than one, because of the contribution of non-radiative recombination centers like dislocations. Eq. (3.19) indicates that the density of excess minority

carriers  $\Delta n(r)$  decreases from the matrix to the dislocation (see Sec. 3.2.1). Therefore, the difference in the experimental CL intensities of a given luminescence band cannot indicate whether the corresponding defect concentration increases or not. If  $\tau_e/\tau_{rad}$  outside the dislocation core (i.e.  $r > r_0$ ), where the non-radiative effect of the dislocation should be accounted for, is assumed to keep constant from the matrix to the dislocation, the integral intensities of the three bands are divided simply by  $\Delta n(r)$  to eliminate the passivation effect of a dislocation for evaluating the spatial variation of the defect concentrations as suggested by Eqs. (3.19) and (3.20). In this way, Fig. 4.4 displays a distinct increase in the concentrations of point defects such as  $B_{As}^-$  and  $(Si_{Ga}V_{Ga})^{2-}$  complexes around the dislocations.

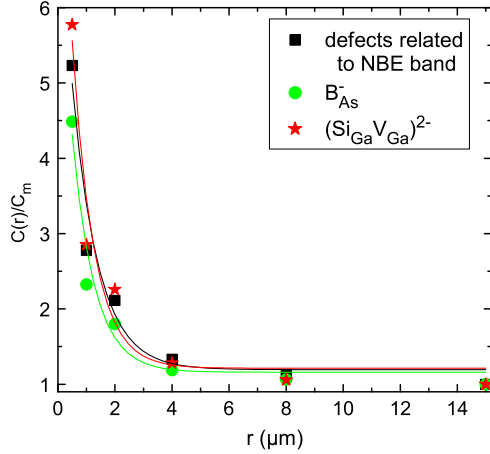


Figure 4.4: The defect concentrations from the matrix to the dislocation deduced by Eqs. (3.19) and (3.20) (symbols). The curves are the fit to show the exponential decay of the defect concentration with the distance from the dislocation. The diffusion length  $L_e$  of excess minority carriers is obtained as  $2.5 \mu\text{m}$ .  $C(r)$  and  $C_m$  are the defect concentrations at the distance  $r$  from the dislocation and in the matrix far from the dislocation, respectively.

In order to explain why the free-electron and the  $(Si_{Ga}V_{Ga})^{2-}$  complex concentrations increase from the matrix to the dislocation, computer simulations based on the diffusion–drift–aggregation model as described in Eqs. (2.20)–(2.26) were performed. In spite of the amphoteric nature of the group-IV elements, it is known that nearly all Si atoms take up only Ga sites when the silicon concentration is below  $5 \times 10^{18} \text{ cm}^{-3}$ , as in the present GaAs:Si samples. Therefore, the conversion of the  $Si_{Ga}^+$  species into the  $Si_{As}^-$  is neglected in the simulations. At the initial time ( $t = 0$ ), the silicon donors were distributed homogeneously from the matrix to the dislocation and the silicon concentration was selected as  $1.0 \times 10^{18} \text{ cm}^{-3}$  so that the free electron concentration in the matrix is nearly the same as the experimental one. Annealing at high temperatures from  $700 \text{ }^\circ\text{C}$  to  $1000 \text{ }^\circ\text{C}$  has been revealed to be effective for arsenic precipitation at the dislocation [41, 83]. Arsenic precipitates were found to be dissolved at the temperature above  $1000 \text{ }^\circ\text{C}$  [44]. It is found that a longer time is needed at a lower temperature in the simulations in order to achieve the free-electron concentration comparable with Raman scattering from the matrix to the dislocation. The simulations of the diffusion–drift–aggregation processes presented here were carried out for 4 hours at  $950 \text{ }^\circ\text{C}$ . The simulations show that  $C_{Si_{Ga}^+}$ ,  $C_{V_{Ga}^{3-}}$ , and  $C_{(Si_{Ga}V_{Ga})^{2-}}$  increase from the matrix to the dislocation within a short-range increasing distance, i.e. only about  $0.03 \mu\text{m}$  if no precipitate is formed ( $\gamma = 0$ ), (Fig. 4.5). Due to the aggregation around the dislocation,  $C_{Si_{Ga}^+}/C_0$  in the matrix is actually a bit below 1 to conserve the total amount of  $Si_{Ga}^+$  donors in the whole region. Especially, in addition to the interaction between a Ga vacancy and a dislocation assumed in the diffusion–drift–aggregation process [see Eq. (2.23)], the Fermi-level effect under consideration enhances the aggregation of  $V_{Ga}^{3-}$  and  $(Si_{Ga}V_{Ga})^{2-}$  complexes around the dislocation. In fact, an increase in the silicon concentration causes a higher Fermi level and thus reduces the formation energies of a Ga vacancy and a  $(Si_{Ga}V_{Ga})^{2-}$  complex to increase their concentrations [36]. As a competition of the amount of  $Si_{Ga}^+$  donors with that of  $V_{Ga}^{3-}$  and  $(Si_{Ga}V_{Ga})^{2-}$  acceptors, the free-electron concentration also becomes higher near the dislocation. However, the extent of about  $0.03 \mu\text{m}$  in the simulation is too small to match the experimental results from the Raman scattering study [see

Fig. 4.2(b)], which shows an extent of about  $10\ \mu\text{m}$  around the dislocation.

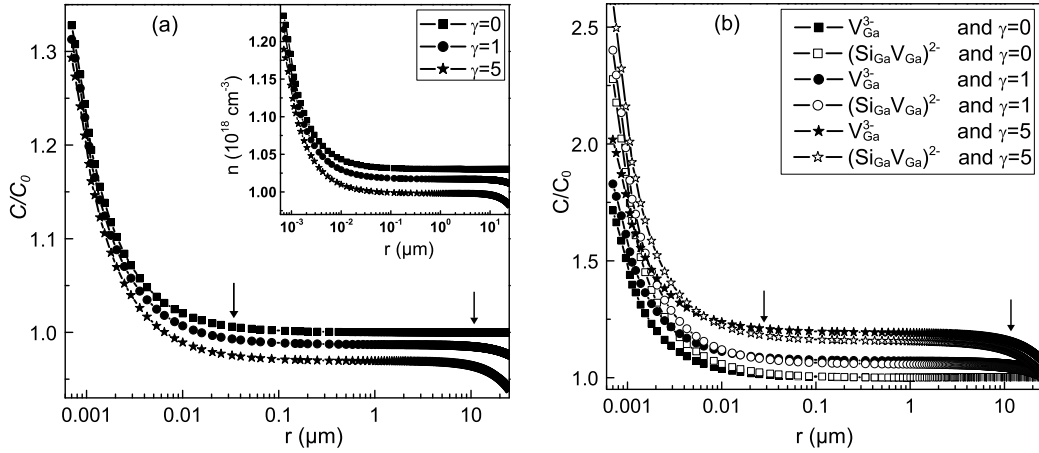


Figure 4.5: (a) The simulated spatial distribution of  $\text{Si}_{\text{Ga}}^+$  and (b) the simulated spatial distribution of  $\text{V}_{\text{Ga}}^{3-}$  and  $(\text{Si}_{\text{Ga}}\text{V}_{\text{Ga}})^{2-}$  after 4 hours at  $950^\circ\text{C}$  ( $C_0$  is the respective equilibrium concentration at the initial time); the corresponding distribution of the free-electron concentration is shown in the inset of (a).  $r$  is the distance from the dislocation. A log scale is used for  $r$  to clearly distinguish the long-range and short-range effects due to precipitation and the interactions between point defects and the dislocation.  $\gamma$  is in unit of  $\text{s}^{-1}$ . The arrows are drawn to guide the eyes (same below).

Assuming the formation of arsenic precipitates at the dislocation ( $\gamma = 1$  and  $\gamma = 5$ ), the increase in  $C_{\text{Si}_{\text{Ga}}^+}$ ,  $C_{\text{V}_{\text{Ga}}^{3-}}$ , and  $C_{(\text{Si}_{\text{Ga}}\text{V}_{\text{Ga}})^{2-}}$ , as well as in the free-electron concentration is extended significantly up to a radius of  $10\ \mu\text{m}$  or so. A larger  $\gamma$  means a higher precipitation rate. Comparison of the three cases with different values of  $\gamma$  states that the higher formation rate of arsenic precipitates reduces further the number of  $\text{Si}_{\text{Ga}}^+$  donors but increases that of  $\text{V}_{\text{Ga}}^{3-}$  and  $(\text{Si}_{\text{Ga}}\text{V}_{\text{Ga}})^{2-}$ , so the free-electron concentration decreases with increasing  $\gamma$  at the same distance from the dislocation. In fact, the free-electron concentration is determined mainly by  $\text{Si}_{\text{Ga}}^+$ , so a similar trend to  $\text{Si}_{\text{Ga}}^+$  appears, because the concentrations of both  $\text{V}_{\text{Ga}}^{3-}$  and  $(\text{Si}_{\text{Ga}}\text{V}_{\text{Ga}})^{2-}$  are far below that of  $\text{Si}_{\text{Ga}}^+$ . Experimentally, Raman scattering shows that the free-electron concentration increases from the matrix to the dislocation and, particularly, that the region of the increase is broad, i.e. about  $10\ \mu\text{m}$  from the dislocation [Fig. 4.2(b)], comparable to the simulations with  $\gamma = 5$ . Therefore, the direct comparison of computer simulations with Raman scattering indicates that the formation of arsenic precipitates is critical for the spatial redistribution of free electrons. Comparing Fig. 4.5 with Fig. 4.4 indicates that the simulated spatial distribution of point defects is qualitatively, not quantitatively, in agreement with that deduced from CL measurements. The difference may possibly be related to the fact that the effect of the other non-radiative recombination centers such as EL2 and precipitates on the CL intensity has been neglected in evaluating the defect concentration through CL measurements.

In summary, the interactions of point defects with dislocations in the case of n-type Si doped GaAs(100) have been studied by means of Raman scattering and cathodoluminescence, in combination with computer simulations based on a microscopic diffusion–drift–aggregation model. The studies elucidate that the interactions induce silicon dopants, gallium vacancies and  $(\text{Si}_{\text{Ga}}\text{V}_{\text{Ga}})^{2-}$  complexes to diffuse to and to accumulate at the dislocations. Computer simulations reveal that the experimentally extended increase of the free-electron and  $(\text{Si}_{\text{Ga}}\text{V}_{\text{Ga}})^{2-}$  concentrations originates from the formation of arsenic precipitates at the dislocation. It should be stressed that the effect of arsenic precipitates on the spatial distribution of point defects from the matrix to the dislocation is rather rough in the simulations because Eq. (2.29) was not obtained strictly from the detailed ki-

netic process as indicated by Eq. (2.28). As has been pointed out in Sec. 3.2.1, precipitates may act as non-radiative recombination centers to reduce the luminescence. Therefore, the experimental evaluation of the defect concentrations around the dislocation based on Eq. (3.20) is not accurate. This may be one reason why the simulations are only qualitatively, not quantitatively, in agreement with the CL data (compare Figs. 4.4 and 4.5). However, the results of Raman spectroscopy, where the distribution of the free-electron concentration at the dislocation was deduced from, are in a good quantitative agreement with the simulations.

# 5 Interactions of Point Defects with Dislocations in GaAs:S

In this chapter, the interactions of point defects with in-grown and fresh dislocations will be studied in GaAs:S. Moreover, the influence of the dislocations on the spatial distribution of point defects as a function of the sulfur concentration will be discussed. The diffusion of sulfur atoms into GaAs has been investigated in various studies [84], but information on the interactions between the point defects and dislocations in GaAs:S have not been given up to now although this directly affects some technological applications of sulfur in some certain GaAs-based devices. Different from n-type GaAs:Si, where most silicon atoms occupy gallium sublattice sites and their diffusion is mediated by gallium vacancies, sulfur atoms in GaAs:S take up arsenic sublattice sites. They diffuse via the kick-out mechanism mediated by interstitial arsenic atoms. In spite of the different diffusion mechanism from GaAs:Si, the whole characters of the dislocations in GaAs:S will be found to be similar to in GaAs:Si. This means that an extended region of increased free-electron concentration around the dislocation is also the case in GaAs:S. Although dislocations act as non-radiative recombination centers to passivate the luminescence, whether the dislocations appear dark or bright in the CL images contrasting their surroundings will be elucidated in this chapter as the competition between radiative and non-radiative recombination channels.

## 5.1 Effect of in-grown dislocations on electrical and optical properties

Similar to the case of GaAs:Si, samples of n-type sulfur doped GaAs with (110) surfaces were grown by the VGF technique under arsenic-rich conditions. The sulfur concentration is about  $1.65 \times 10^{18}$  atoms/cm<sup>3</sup>. The samples were firstly cleaned by mechano-chemical polishing. Then they were etched by the DSL photoetching procedure as described in Chapter 4 in order to reveal the in-grown dislocations at the sample surface in Raman scattering experiments. Raman scattering at room temperature and cathodoluminescence experiments at 75K were carried out to determine the spatial distribution of the free-electron concentration and luminescence due to interactions between point defects and dislocations. The experimental procedures are the same as the ones in Chapter 4.

The x-ray Laue pattern confirms that the surface of GaAs used here is nearly of the (110) orientation. According to the selection rules, the LO phonon is prohibited, while the TO mode is allowed in the Raman scattering from (110) surfaces of a perfect GaAs crystal. A certain disorder around the dislocation or a small deviation from the (110) orientation may result in the appearance of the LO phonon in Raman scattering [Fig. 5.1(a)]. The  $L^-$  and  $L^+$  peaks are the two submodes of the split LO phonon due to the phonon-plasmon coupling. The  $L^-$  submode probably degenerates with the TO phonon present in the Raman spectra, so it is no more suitable to take the ratio of the intensity of the  $L^-$  mode to that of the LO mode for the calculation of the free-electron concentration by Eqs. (3.14) and (3.15). Alternatively, the peak position of the  $L^+$  mode is utilized for this purpose according to Eqs. (3.8) and (3.10). Fig. 5.1(c) shows a hillock in the optical image after the DSL etching, indicating an increased free-electron concentration around the dislocation,

as is confirmed by the spatial mapping of the free-electron concentration calculated from the peak position of the  $L^+$  mode [see Fig. 5.1(d)]. The free-electron concentration increases from the matrix ( $1.64 \times 10^{18} \text{ cm}^{-3}$ ) to the dislocation ( $1.75 \times 10^{18} \text{ cm}^{-3}$ ) with a radius of about  $10 \mu\text{m}$ , similar to that in n-type GaAs:Si. One more Raman mode around  $200 \text{ cm}^{-1}$  occasionally appears in the Raman spectra [Fig. 5.1(b)]. This mode, generally attributed to the TO phonon of rhombohedral arsenic precipitates, suggests their formation at the dislocations [67]. The LO phonon of arsenic precipitates at  $257 \text{ cm}^{-1}$  cannot be distinguished in the present Raman spectra, possibly because of its submergence into the broad TO/ $L^-$  peak.

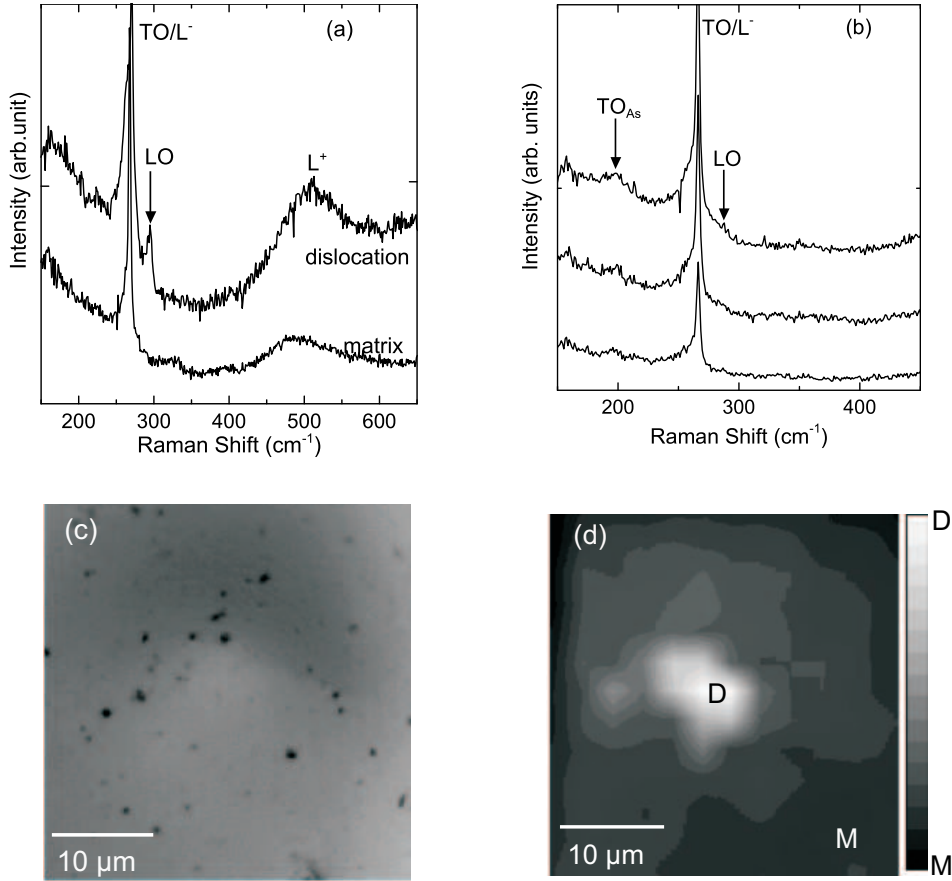


*Figure 5.1:* (a) Raman spectra around the dislocation and in the matrix in (110)-orientation GaAs:S. (b) Arsenic-precipitate-related feature appears in the Raman spectra at the dislocation. For better resolution of the  $\text{TO}_{\text{As}}$  peak, a smaller confocal hole and thus a smaller focus diameter at the surface of the sample than in (a) was selected. (c) Light microscopy image of a hillock at the dislocation after the DSL etching. (d) A map of the spatial distribution of the free-electron concentration around the dislocation revealed by Raman scattering. It increases from  $1.64 \times 10^{18} \text{ cm}^{-3}$  in the matrix (M) to  $1.75 \times 10^{18} \text{ cm}^{-3}$  at the dislocation (D). The position is the same as in (c).

Panchromatic CL images at a wavelength range from 400 to 900 nm were acquired by a photomultiplier. One of them is shown in Fig. 5.2(a). The image exhibits dark dots, corresponding to dislocations, contrasting the bright surrounding. Similarly, Fig. 5.2(c) shows another panchromatic CL image of the same spatial region. This picture is obtained by the Ge detector, whose sensitivity range is from 800 to 1600 nm. As a matter of fact, as indicated in Fig. 5.2(b) and (d), the CL images in Figs. 5.2(a) and (c) are connected to the NBE,  $\text{B}_{\text{As}}^-$  acceptor-related, and  $(\text{S}_{\text{As}}\text{V}_{\text{Ga}})^{2-}$  complex-related emissions, respectively.  $\text{B}_{\text{As}}^-$  is contributed by the encapsulant (boron

oxide) during the growth of GaAs. The luminescence band at 830 nm (1.49 eV) is correlated with the NBE transition. The other two bands at 930 nm (1.33 eV) and at 1050 nm (1.18 eV) have been observed by the Ge detector [Fig. 5.2(d)]. The 1.18 eV band is identified as the transitions within the  $(S_{As}V_{Ga})^{2-}$  complexes [68], while the 1.33 eV band is due to the recombination from the states near the conduction band to the  $B_{As}^-$  acceptor states, about 180 meV above the valence band [82].

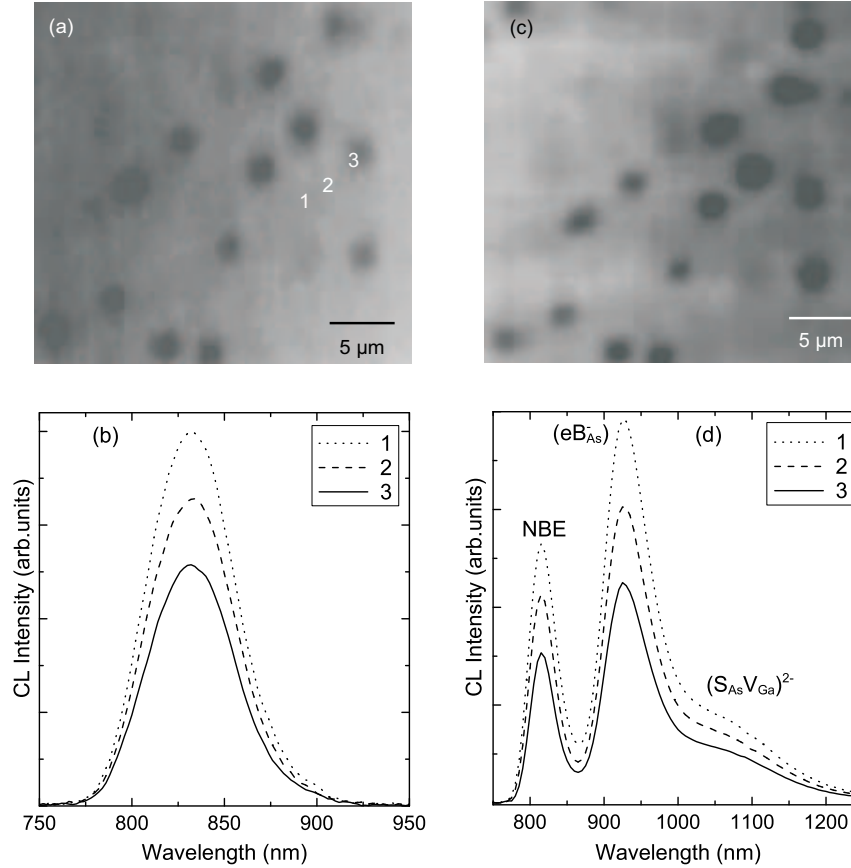


*Figure 5.2:* (a) A panchromatic CL image of GaAs:S taken by the photomultiplier. The image comes mainly from the NBE emission [see (b)]. (c) A panchromatic CL image for the same region as in (a) taken by the Ge detector. The image comes mainly from the NBE, the  $(eB_{As}^-)$ , and  $(S_{As}V_{Ga})^{2-}$  transitions [see (d)]. (b) and (d) CL spectra of GaAs:S at 75 K taken at different positions 1, 2, and 3 marked in (a) by the photomultiplier or by the Ge detector. The spectra and images weren't corrected according to the sensitivity of detectors.

Similar to the treatment of the CL results of GaAs:Si in Chapter 4, the integral intensities of the three bands are divided by  $\Delta n(r)$  so as to eliminate the passivation effect of a dislocation. In this way, the spatial variation of the defect concentrations is evaluated, as suggested by Eq. (3.20). Fig. 5.3 shows a distinct increase in the concentrations of point defects such as  $B_{As}^-$  and  $(S_{As}V_{Ga})^{2-}$  complexes around the dislocations, similar to that in n-type GaAs:Si discussed in Chapter 4.

As will be shown in Sec. 5.3, the interaction of point defects with dislocations and arsenic precipitation at the dislocation result in the spatially extended increase in the free-electron concentration from the matrix to the dislocation in GaAs:S, as revealed by Raman scattering [see Fig. 5.1(d)]. Additional investigations of n-type GaAs:Te show that the free-electron concentration decreases from the matrix to the dislocation although tellurium atoms occupy arsenic lattice

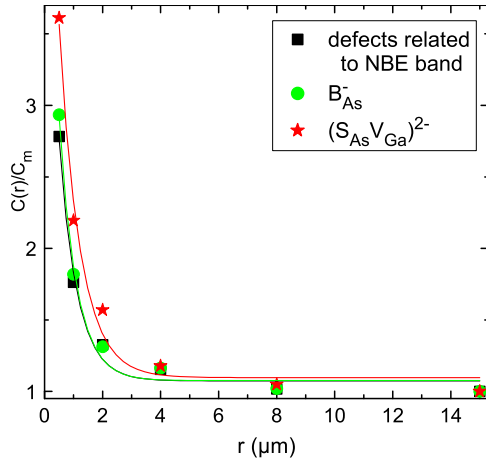
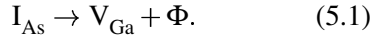


Figure 5.3: Variation of defect concentrations from the matrix to the dislocation in GaAs:S. The symbols represent the values deduced by Eqs. (3.19) and (3.20) from the experimental intensity of the corresponding CL bands; the curves are the fit and show an exponential increase in the concentrations of various defects from the matrix to the dislocation. The effective diffusion length  $L_e$  of excess carriers is obtained as  $2.5 \mu\text{m}$ .  $C(r)$  and  $C_m$  are the defect concentrations at the distance  $r$  from the dislocation and in the matrix far from the dislocation, respectively.

sites as sulfur atoms. It has been found that there are much more dislocation loops in GaAs:Te than in GaAs:S. Fig. 5.4 shows a TEM bright-field image of n-type GaAs:Te to reveal interstitial dislocation loops at the in-grown dislocation. The formation of a lot of interstitial dislocation loops may largely consume the interstitial arsenic so that no arsenic precipitate can be formed. Accompanying the formation of interstitial dislocation loops, gallium vacancies acting as acceptors, are pronouncedly generated,



where  $\Phi$  represents an interstitial dislocation loop. As a result, the free-electron concentration near the dislocation becomes lower than in the matrix. Therefore, these studies elucidate that the increase or decrease in the free-electron concentration from the matrix to the dislocation cannot be simply attributed to a dilution of the concentration of acceptors or donors occupying the arsenic sublattice sites at the dislocation suggested in Refs. [44] and [67]. Isolated gallium vacancies are not stable at low temperatures. They combine with  $\text{Te}_{\text{As}}^+$  donors to form  $(\text{Te}_{\text{As}} V_{\text{Ga}})^{2-}$  complexes in GaAs:Te. Correspondingly, a luminescence band at about 1.20 eV, originating from internal transitions within  $(\text{Te}_{\text{As}} V_{\text{Ga}})^{2-}$  complexes, has been observed in GaAs:Te, as in n-type GaAs:Si and GaAs:S.

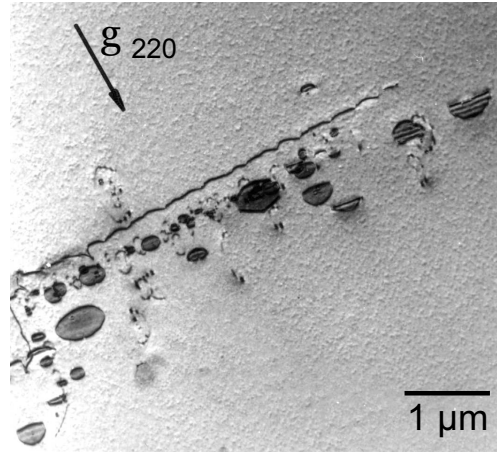


Figure 5.4: A TEM bright-field image of n-type GaAs:Te shows the decoration of interstitial dislocation loops at the in-grown dislocation.  $\mathbf{g}$  denotes the diffraction vector.

## 5.2 GaAs:S with fresh dislocations

In order to further understand the effect of dislocations on electric and optical properties of GaAs with respect to their interaction with point defects, a set of GaAs:S samples with fresh dislocations have been prepared as follows. In such a way, the influence of parameters such as temperature, arsenic pressure, and dopant concentration on the interaction can be determined. In-diffusion experiments were carried out with sulfur of different quantities solved in benzene ( $C_6H_6$ ). Semi-insulating GaAs wafers with (001) surfaces grown by the VGF technique were used. The in-diffusion experiments were performed under 1 atmosphere arsenic pressure at 1100 °C for 12 hours in quartz ampoules after evacuating them to a pressure below  $1.5 \times 10^{-6}$  Torr. After 12 hours at 1100 °C, the samples were quenched immediately in water. As a third step, fresh dislocations were created by scratching the (001) surface along the [100] direction using a diamond scribe at room temperature. The applied load was 6 mN. The orientation of the scratch and the character of the dislocations are shown in Fig. 5.5. Finally, the samples were annealed at 900 °C for 2 hours in sealed quartz ampoules still under 1 atmosphere arsenic pressure and then cooled down at a rate of 0.6 K/s. In this way, the diffusion, drift, and aggregation of point defects at the dislocation is realized. It is well known that a scratch in the  $\langle 100 \rangle$  direction on a (001) surface leads mainly to dislocations on  $(1\bar{1}1)_{As}$  and  $(111)_{Ga}$  slip planes [48]. Before each thermal processes, the quartz ampoules used were cleaned by RCA1 ( $H_2O : H_2O_2 : NH_3 = 5 : 1 : 1$ ) and RCA2 ( $H_2O : H_2O_2 : HCl = 6 : 1 : 1$ ) solutions to remove the carbon and other organic residuals (RCA1) and metals (RCA2) possibly existing in the quartz ampoules. The GaAs samples were cleaned by HCl to remove oxide at the surface. Afterwards, secondary ion mass spectroscopy (SIMS) was performed to evaluate the sulfur concentrations in the final samples.\* The samples were observed by Raman scattering, TEM, and CL.

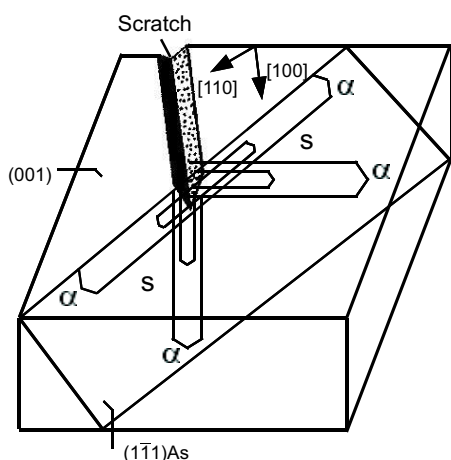


Figure 5.5: The schematic diagram of the formation of dislocations at a scratch on a GaAs(001) surface. With the scratch along the [100] direction, elongated loops with leading  $60^\circ$   $\alpha$  or  $\beta$  and long screw dislocations may be formed on the  $(1\bar{1}1)_{As}$  or  $(111)_{Ga}$  slip planes. Only one slip plane is shown here.

### 5.2.1 Effect of dislocations on the luminescence of GaAs:S with doping levels

SIMS reveals that the sulfur concentration near the surface of GaAs increases from sample 1# ( $1.0 \times 10^{16} \text{ cm}^{-3}$ ), 2# ( $2.5 \times 10^{17} \text{ cm}^{-3}$ ) to 3# ( $1.5 \times 10^{18} \text{ cm}^{-3}$ ) and that the concentration of boron atoms acting as acceptors is  $5.0 \times 10^{17} \text{ cm}^{-3}$ .

Figs. 5.6, 5.7 and 5.8(a) and (b) show some dislocations which appear as dark dots to indicate that the dislocations end at (001) surface of GaAs. The other dark lines in CL images represent

\*SIMS was performed at RTG Mikroanalyse GmbH Berlin.

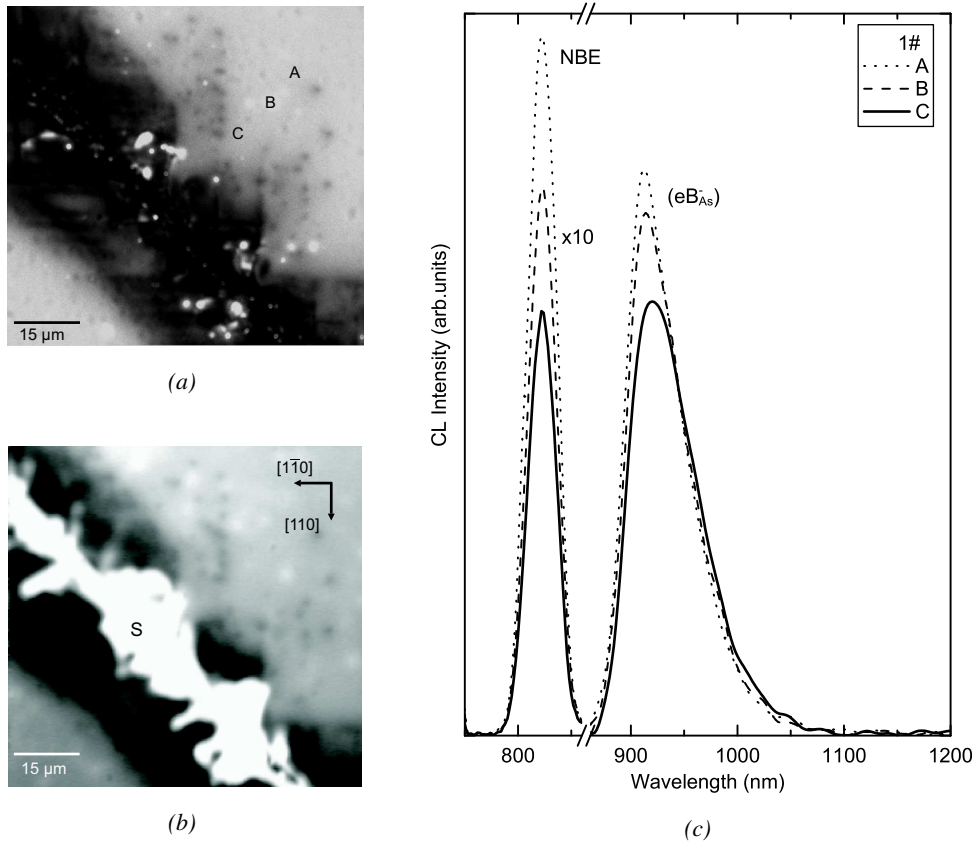


Figure 5.6: (a) A panchromatic CL image taken by the photomultiplier. (b) A panchromatic CL image in the same region as (a) taken by the Ge detector. (c) CL spectra of GaAs(001):S with a sulfur concentration of  $1.0 \times 10^{16} \text{ cm}^{-3}$  (sample 1#) at 75 K taken at different positions, A, B, and C marked in (a), from the matrix to the dislocation-rich region. In (b), S denotes scratch.

dislocations inclined or parallel to the (001) surface. Both the dark dots and lines are aligned in  $\langle 110 \rangle$  directions from the scratched line.

The CL images in Figs. 5.6, 5.7 and 5.8 (a) are correlated with the NBE luminescence while those in Figs. 5.6, 5.7 and 5.8(b) are contributed mainly by the deep-level defect-related recombination with a wavelength of the emitted luminescence larger than 900 nm. With increasing sulfur concentration, the defect-related luminescence band and thus possibly their origin vary [compare (c) of Figs. 5.6, 5.7 and 5.8]. The defect-related luminescence will be discussed in more detail in Chapter 6, where the bands at 930 nm, at 950 nm and at 1080 nm are determined to be connected to  $B_{As}^-$ ,  $(S_{As}V_{Ga})^-$ , and  $(S_{As}V_{Ga})^{2-}$ , respectively. Since the sulfur concentration in sample 1# is so low that it is nearly semi-insulating, the defect-related luminescence is mainly from the transition of  $(eB_{As}^-)$  [see Fig. 5.6(c)]. When the sulfur concentration is high enough ( $2.5 \times 10^{17} \text{ cm}^{-3}$ ) in sample 2#, the transitions within the  $(S_{As}V_{Ga})^-$  complexes are dominant. Although the sulfur concentration and thus the  $(S_{As}V_{Ga})^-$ -complex concentration in sample 2# is still below the boron concentration ( $5.0 \times 10^{17} \text{ cm}^{-3}$ ), the luminescence band around 930 nm related to  $B_{As}^-$  is rather weak so that it is submerged in the band around 950 nm due to the transitions within the  $(S_{As}V_{Ga})^-$  complexes [see Fig. 5.7(c)]. The fact indicates that the recombination probability through the channel of  $(eB_{As}^-)$  is smaller than the one through the channel of the complexes [see Eq. (3.20)]. At the highest sulfur concentration (sample 3#), mainly the transitions within the

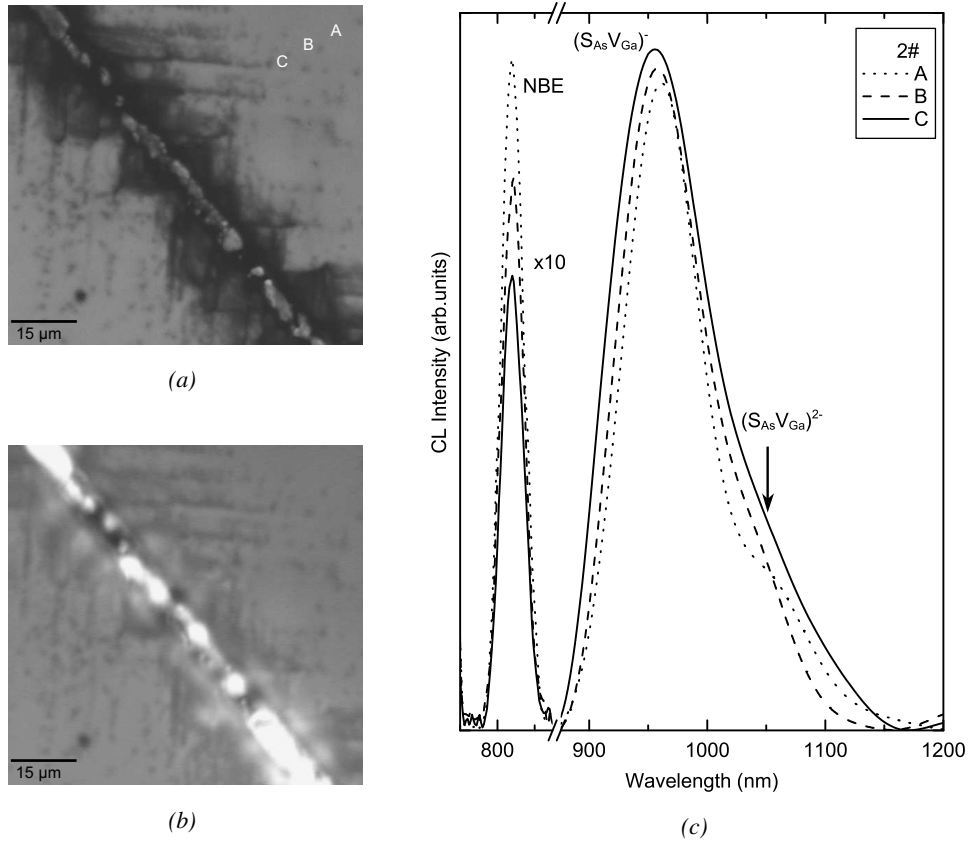


Figure 5.7: (a) A panchromatic CL image taken by the photomultiplier. (b) A panchromatic CL image in the same region as (a) taken by the Ge detector. (c) CL spectra of GaAs(001):S with a sulfur concentration of  $2.5 \times 10^{17} \text{ cm}^{-3}$  (sample 2#) at 75 K taken at different positions, A, B, and C marked in (a), from the matrix to the dislocation-rich region.

$(S_{\text{As}}V_{\text{Ga}})^{2-}$  complexes contribute to the defect-related luminescence band around 1080 nm [see Fig. 5.8(c)]. Engler et al. found that the radiative recombination within the  $(S_{\text{As}}V_{\text{Ga}})^{2-}$  complexes could exceed the non-radiative channels at the dislocations so that the dislocations have a bright contrast when the concentration of the sulfur atoms and the  $(S_{\text{As}}V_{\text{Ga}})^{2-}$  complexes is high enough [85].

Although the dark dislocations contrast with their locally bright surroundings, the contrast for the defect-related luminescence from the matrix to dislocation-rich region is different from a low to a high sulfur concentration, that is, the intensity of the defect-related luminescence band from the matrix to the dislocation-rich region decreases at the lowest sulfur concentration [sample 1#, see Figs. 5.6(b) and (c)], then weakly increases at the modest sulfur concentration [sample 2#, see Figs. 5.7(b) and (c)], and increases at the high sulfur concentration [sample 3#, see Figs. 5.8(b) and (c)]. The density of the dislocations generated near the scratch is high so that they are very close to each other, so the luminescence around an individual dislocation may be influenced by the neighboring ones. Therefore, it is not meaningful to identify the effect of a single dislocation on the luminescence. Comparisons of the luminescence between the dislocation-free matrix and the dislocation-rich region are made.

Given that the excess electron-hole pairs available for the NBE transition are assumed to keep constant from the matrix to the dislocation region, and that  $\tau_e/\tau_{\text{rad}}$  at the same position is the

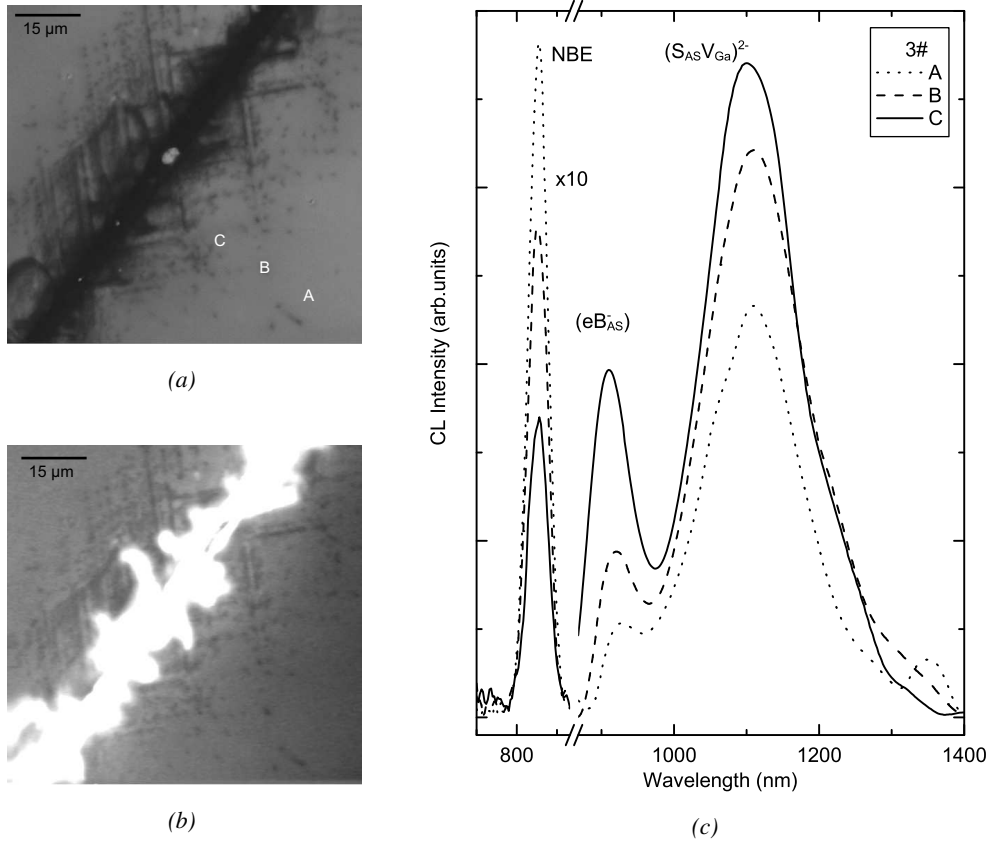


Figure 5.8: (a) A panchromatic CL image taken by photomultiplier. (b) A panchromatic CL image the same region as (a) taken by the Ge detector. (c) CL spectra of GaAs(100):S with a sulfur concentration of  $1.5 \times 10^{18} \text{ cm}^{-3}$  (sample 3#) at 75 K taken at different positions, A, B, and C marked in (a), from the matrix to the dislocation-rich region.

same for the different luminescence bands, a parameter  $C_{\text{CL}}^*$  is introduced in order to eliminate the passivation effect of dislocations to connect roughly CL intensity directly to the concentration of the corresponding point defects,

$$C_{\text{CL}}^* = \frac{I(r)/I_{\text{NBE}}(r)}{I^M/I_{\text{NBE}}^M} \propto \frac{C(r)}{C^M} \quad (5.2)$$

In Eq. (5.2),  $I(r)$  and  $I_{\text{NBE}}(r)$  or  $I^M$  and  $I_{\text{NBE}}^M$  represent the integral intensity of a defect-related luminescence band and the NBE band at the distance  $r$  from the dislocation, or in the matrix far from the dislocation, respectively.  $C(r)$  or  $C^M$  denotes the concentration of defects at the distance  $r$  from the dislocation or in the matrix. It is worth noting that the direct application of Eqs. 3.19 and (3.20) for evaluating the difference in the defect concentration from the matrix to the dislocation-rich region is no longer suitable here since the distance  $r$  from an individual dislocation in the dislocation-rich region is ambiguous. For accurately evaluating the integrated CL intensity of the luminescence band, the CL spectra have actually been decomposed into four bands, i.e. NBE,  $(eB_{\text{As}}^-)$ -related,  $(S_{\text{As}}V_{\text{Ga}})^-$ -related, and  $(S_{\text{As}}V_{\text{Ga}})^{2-}$ -related bands. Fig. 5.9 shows that the CL contrast from the matrix to the dislocation-rich region and thus the aggregation of  $(S_{\text{As}}V_{\text{Ga}})^{2-}$ -complexes around the dislocation is enhanced with increasing sulfur concentration, comparable to the simulated results, where the arsenic precipitates are assumed to be formed at individual

dislocations in accordance with Sec. 2.5.2.

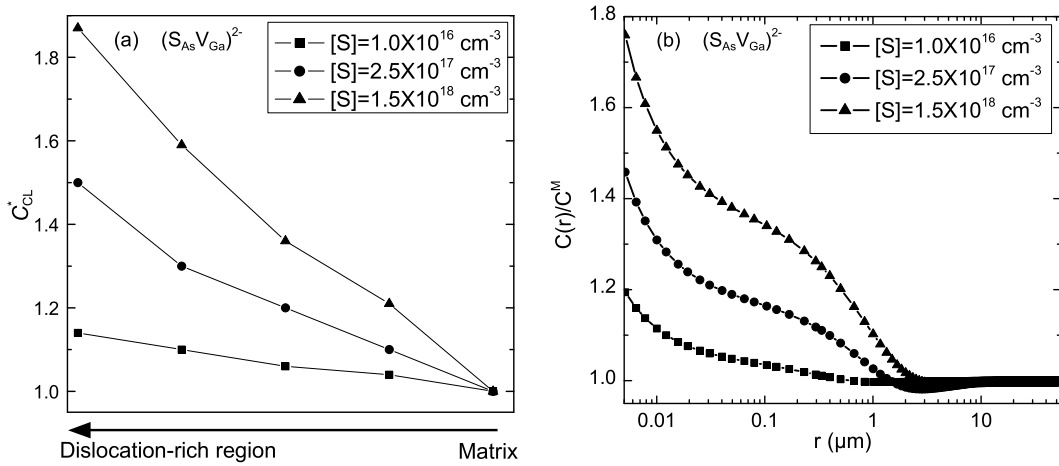


Figure 5.9: (a) The CL contrast of the 1.20 eV-luminescence band, originating from the transitions within  $(S_{As}V_{Ga})^{2-}$  complexes, as a function of position from the matrix to the dislocation-rich region. The separation between two neighboring points is about  $4 \mu\text{m}$ . (b) Simulated spatial distribution of the  $(S_{As}V_{Ga})^{2-}$  complexes at an individual dislocation with different sulfur concentrations in the matrix.  $r$  is the distance from the dislocation. The simulation were carried out at  $900 \text{ }^\circ\text{C}$  for 2 hours based on the diffusion–drift–aggregation model built in Sec. 2.5.2. Arsenic precipitation at the dislocation was assumed in the simulations ( $\gamma^* = 1$ ).

The simulations can interpret qualitatively, but not quantitatively the experimental results. Several limitations should be considered. 1.) The samples after thermal processing might contain some defects in non-thermal equilibrium so that the defect concentration is higher than in the simulation, where the defect concentration at thermal equilibrium was utilized at initial time. 2.) Dislocation climb is not included in the simulations although it may be a very important process when annealing the sample with fresh dislocations. In practice, dislocation climb would induce the absorption of Ga vacancies (As interstitials) plus the simultaneous emission of As interstitials (Ga vacancies) [33]. Moreover, the dislocation density as shown in CL images is so high that the dislocation-dislocation interactions should have been taken into account in the simulations. 3.) The possible effect of the residual stress due to the deformation on the luminescence is not experimentally accounted for. 4.) Arsenic precipitation around the dislocation may actually be accompanied by emission of vacancies for accommodating the precipitates although the process was neglected in the simulations.

## 5.2.2 TEM observations of fresh dislocations

Transmission electron microscopy (TEM) with a 1000 kV high voltage microscope (JEM 1000) was applied to characterize the nature of the dislocations. Fig. 5.10 shows a series of dislocations as dark lines in the TEM bright-field (BF) diffraction contrast. Stacking faults are also visible, appearing as fringes in Figs. 5.10(a) and (c). The nature of the dislocations created by scratch is determined from the TEM bright-field images by using  $\mathbf{g} \cdot \mathbf{b} = 0$  invisible rule, where  $\mathbf{g}$  is the diffraction vector and  $\mathbf{b}$  is the Burgers vector.

The dislocations are found to be mixture of Shockley partial dislocations, having Burgers vectors of  $a/6 \langle 112 \rangle$ , and perfect dislocations with Burgers vectors of  $a/2 \langle 110 \rangle$ . The dislocations at different glide planes may attract each other to intersect each other at some segments, as AB and CD dislocations in Fig. 5.10(d). The extinction length  $\xi_g$  for the  $\langle 220 \rangle$  and  $\langle 040 \rangle$  diffraction vec-

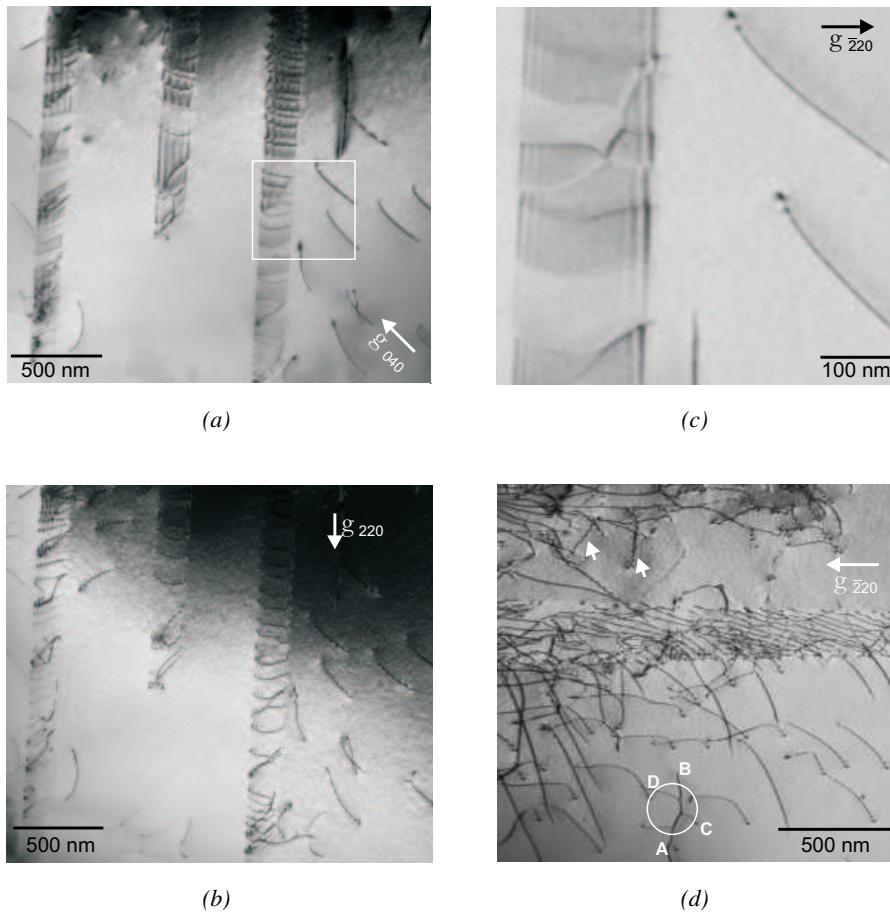


Figure 5.10: TEM bright-field images of the GaAs:S sample 2#. (a) and (b) are taken at the same positions but with the different diffraction vectors  $\mathbf{g}$ . (c) A higher magnification of the marked region in (a) to show the stacking fault. (d) The intersection of two dislocations (circle). The typical characters of dislocations are the same for the samples 1# and 3#.

tors is about 50 nm, so the width of a dislocation dark contrast in TEM BF contrast is  $\xi_g/\pi$ , about 17 nm. This implies that the diameter of a precipitate at the dislocation must be larger than 17 nm in order to be observed from the TEM BF contrast. The diffusion–drift–aggregation process was experimentally carried out at 900 °C for 2 hours. This temperature may be low and the time may be short for arsenic precipitates to be significantly formed at the dislocations. This may be the reason why TEM BF contrast cannot systematically detect precipitates.

No interstitial or vacancy dislocation loops are systematically observed in the GaAs:S samples under investigation, although it is the case in group-VI (Te) doped GaAs [86, 87]. In-diffusion experiments of sulfur in GaAs showed that the amount of dislocation loops depends on the annealing conditions and they can be formed only when the gallium vacancies are supersaturated [88].

## 5.3 Why are arsenic precipitates formed at dislocations

Metal-semiconductor composites, in which metal precipitates are dispersed in a crystalline semiconductor, present a fruitful field of investigation for various electrical and optical properties with some potential applications. Special attention has been paid to arsenic precipitates in GaAs. Arsenic precipitates are assumed to be semimetallic in nature and to form buried Schottky barriers [89]. Many investigations have shown that arsenic precipitates could be formed after annealing above 550 °C of low-temperature-grown (LT) GaAs containing 2 vol.% excess arsenic in the form of  $\text{As}_{\text{Ga}}^+$  antisites and  $\text{I}_{\text{As}}$  interstitials [90]. The semimetallic nature of arsenic precipitates was exploited to modify the electronic properties of LT-GaAs [91]. Other works reported that arsenic precipitates exist at dislocations, despite their absence in the matrix of semi-insulating or doped bulk GaAs [41, 67, 72]. As it is revealed in Raman spectra from n-type GaAs:Si and GaAs:S in the former sections, the free-electron concentration increases from the matrix to the dislocation in a cylinder having a radius as large as 10  $\mu\text{m}$ , which was preliminarily explained by considering the formation of arsenic precipitates at dislocations. It is thus of fundamental interest to further clarify why arsenic precipitates prefer to stay at dislocations, but not in the matrix and to what extent they can influence the spatial distribution of point defects and the free-electron concentration. The computer simulations presented here will show that it is energetically and kinetically favorable for arsenic precipitates to stay at dislocations. Two kinds of simulations have been carried out. The first approach is molecular dynamics (MD) simulations to explore the difference in the total energy of the As–GaAs system as a function of the distance of the arsenic precipitate from the dislocation. In the second approach, the microscopic diffusion–drift–aggregation processes of point defects are simulated to elucidate i.) whether there are kinetic reasons to form arsenic precipitates at dislocations, but not in the matrix, and ii) why the free-electron concentration obtained in previous Raman scattering experiments increases from the matrix to the dislocation in a cylinder having a radius as large as 10  $\mu\text{m}$  in n-type GaAs such as GaAs:Si and GaAs:S.

### 5.3.1 Energetic factor

Molecular dynamics simulations have been performed to elucidate whether the formation of arsenic precipitates at the dislocation in GaAs is energetically favorable or not. Simply, MD is a computer simulation technique where the time evolution of a set of interacting atoms is completely determined by integrating their equations of motion, given a set of initial positions and velocities. In MD, the classical equation of motion of an atom  $i$  is the usual Newtonian equation

$$m_i \frac{d^2 \mathbf{r}_i}{dt^2} = \mathbf{F}_i = -\nabla_i E, \quad (5.3)$$

where  $m_i$  is the mass of atom  $i$ ,  $\mathbf{r}_i$  its coordinate and  $\mathbf{F}_i$  the force acting upon it due to the interactions with other atoms;  $E$  is the interaction potential of the system containing  $N$  atoms. Eq. (5.3) can be solved by numerical integration to produce the atomic trajectories. The velocity Verlet algorithm was applied for this purpose in the present MD simulations [92].

In most semiconductors, the atoms are bound by forming covalent or predominantly covalent bonds. The covalent bonds typically have a strong directional dependence with some preferred angles between the bonds because of the nature of the hybridization of the electron orbitals. So the interaction potential should have an angular dependence, and thus they are at least three-body potentials. Several empirical potentials such as Stillinger–Weber [93] and Tersoff-type [94] potentials, especially for C, Si, Ge, GaAs and InAs, have been developed to allow one to simulate a large atomic system. The common character of the potentials is that they explicitly consist of two-body and three-body interactions. A so-called Sayed potential based on the Tersoff-potential formalism is used here to construct the interactions between Ga–Ga, As–As and Ga–As, depending

on the local environment [95]. The total potential energy of the system is

$$E = \frac{1}{2} \sum_{i \neq j} f_c(r_{ij}) \left[ E_{rep}(r_{ij}) - B_{ij} E_{bond}(r_{ij}) \right], \quad (5.4)$$

where  $f_c(r_{ij})$  is a smooth cutoff function,

$$f_c(r_{ij}) = \begin{cases} 1, & (\text{for } r_{ij} < R_{ij}) \\ \frac{1}{2} + \frac{1}{2} \cos \left[ \pi(r_{ij} - R_{ij}) / (S_{ij} - R_{ij}) \right], & (\text{for } R_{ij} < r_{ij} < S_{ij}) \\ 0, & (\text{for } r_{ij} > S_{ij}) \end{cases}, \quad (5.5)$$

$$E_{rep}(r_{ij}) = A_{ij} \exp(-\lambda_{ij} r_{ij}) \text{ and } E_{bond}(r_{ij}) = -B_{ij} \exp(-\mu_{ij} r_{ij}), \quad (5.6)$$

$$B_{ij} = (1 + \beta_{ij}^{n_{ij}} \zeta_{ij}^{n_{ij}})^{\frac{1}{2n_{ij}}}. \quad (5.7)$$

Here,

$$\zeta_{ij} = \sum_{k \neq i, j} f_c(r_{ik}) g(\theta_{jik}) \exp \left[ \eta_{ik}^3 (r_{ij} - r_{ik})^3 \right], \quad (5.8)$$

$$g(\theta_{jik}) = 1 + \frac{c_{ik}^2}{d_{ik}^2} - \frac{c_{ik}^2}{d_{ik}^2 + (h_{ij} - \cos \theta_{jik})^2}. \quad (5.9)$$

Here  $r_{ij}$  is the distance between atoms  $i$  and  $j$ .  $B_{ij}$  measures the relative strength of the attraction between atoms  $i$  and  $j$ , which depends on the parameters  $\beta$ ,  $n$ , and the function  $\zeta_{ij}$ , which measures the total effect of all nearby atoms on the interaction.  $\theta_{jik}$  is the angle between  $r_{ij}$  and  $r_{ik}$ . The parameters  $A$ ,  $B$ ,  $R$ ,  $S$ ,  $c$ ,  $d$ ,  $\lambda$ ,  $\mu$  and  $h$  are determined by fitting experimental data such as lattice constant, cohesive energy, elastic constants of bulk GaAs, as well as of small As precipitates and of GaAs dimers. Table. 5.1 gives Sayed's potential parameters for Ga–Ga, Ga–As and As–As interactions used in the present molecular dynamics simulations. From Sayed's potential with the original parameters, the zinc-blende structure is not in the ground state of a bulk GaAs crystal, and vanishingly small values of the Young's modulus and elastic constant  $C_{44}$  are obtained. However, by setting the parameter  $\eta = 0$ , the potential gives a fairly reasonable behavior [96].

Table 5.1: Parameter values for Sayed's potential used in the present MD simulations [95]

	Ga–Ga	Ga–As	As–As
$n$	3.4729041	6.317410	0.60879133
$c$	0.07629773	1.226302	5.27313100
$d$	19.796474	0.790396	0.75102662
$h$	7.1459174	-0.518489	0.15292354
$\beta$	0.23586237	0.357192	0.00748809
$\lambda$	2.50842747	2.82809263	2.384132239
$\mu$	1.490824	1.72301158	1.728726300
$\eta$	0	0	0
$A$	993.888094	2543.29720	1571.86084
$B$	136.123032	314.459660	546.4316579
$R$	3.4	3.4	3.4
$S$	3.6	3.6	3.6

A perfect GaAs matrix was built as a  $7\sqrt{2}a \times 8\sqrt{6}a \times 6\sqrt{3}a$  block in  $[1\bar{1}0]$ ,  $[11\bar{2}]$ , and  $[111]$  directions (lattice parameter  $a = 5.65 \text{ \AA}$ ). It contains 16128 atoms. Next, all the atoms were dis-

placed according to the isotropic elasticity theory to generate a  $90^\circ$  partial glide dislocation in the center of the supercell. According to the isotropic elasticity theory, due to the existence of an edge dislocation, an atom is displaced from its equilibrium position only in the directions perpendicular to the dislocation line. The displacement depends on the Burgers vector, Poisson's ratio, and its coordination from the dislocation [97]. Although most crystals are elastically anisotropic, it is simpler to use linear isotropic elasticity theory. This still results in a good approximation, except for the dislocation core, for energy of the dislocation, the interaction force between two dislocations and the interaction energy between the dislocation and the point defect [97]. In the MD simulations, the matrix is divided into two regions, boundary and core regions. The thickness of the boundary region is larger than the cutoff radius in order to avoid that atoms in the core region feel the finiteness of the system. The atoms in the boundary region are fixed and those in the core region are allowed to move freely. There are hence 9086 movable and 7042 fixed atoms in the supercell. A periodic boundary condition has been applied in the  $[1\bar{1}0]$  direction, and a fixed boundary conditions has been imposed in the  $[11\bar{2}]$  and  $[111]$  directions. The newly constructed GaAs matrix with a dislocation has been equilibrated at a temperature  $T = 0\text{K}$ . Next, an arsenic precipitate with 83 atoms was embedded into the GaAs matrix at some position. The precipitate must be large enough. Otherwise, if the precipitate is too small, such as a few atoms, the total energy of the system depends further on the detailed sites (e.g. bond center, hexagonal or tetrahedral sites) occupied by the precipitate in addition to the distance of the precipitate from the dislocation. The structure of the modeled precipitate is rhombohedral, in accordance with experiments [98]. Afterwards, the system was relaxed by means of MD energy minimization at 0 K (i.e. the velocity is set to zero when the dot product of force and momentum is negative. Otherwise, the velocity is unchanged) for a time long enough that its total internal energy no longer varies with time.

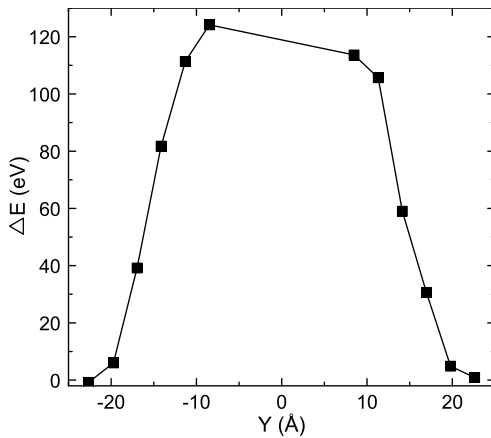


Figure 5.11: MD calculation of the difference in the total energy of the  $\text{As}_{83}$ -GaAs system as a function of the distance of the  $\text{As}_{83}$  precipitate from the dislocation in the  $[11\bar{2}]$  direction. The  $90^\circ$  partial dislocation lies at  $Y = 0$  in the  $[11\bar{2}]$  direction and at  $Z = 0$  in the  $[111]$  direction. The line is drawn to guide the eye.

The arsenic precipitate was placed at several positions  $Y$  in the  $[11\bar{2}]$  direction with the precipitate center-of-mass coordinates  $X = 0$  in the  $[1\bar{1}0]$  and  $Z = 0$  in the  $[111]$  direction for calculating the total internal energy  $E_{\text{total}}(Y)$  of the As-GaAs system. Fig 5.11 shows the difference in the total internal energy,  $\Delta E = E_{\text{total}}^{\text{m}} - E_{\text{total}}(Y)$  as a function of the position  $Y$  of the precipitate from the dislocation.  $E_{\text{total}}^{\text{m}}$  corresponds to the total energy in the matrix far from the dislocation. Since the internal energy is negative, a larger  $\Delta E$  means that the As-GaAs system has a smaller total energy and thus lies in a more stable state. Therefore, it can be concluded from Fig. 5.11 that it is energetically favorable for arsenic precipitates to stay at the dislocation. From observations by transmission electron microscopy [98], arsenic precipitates have been found with diameters of at least several tens of nanometers, by far larger than the simulated  $\text{As}_{83}$ . However, it is still impossible for the processing capability of present computers to simulate such a large-precipitate-matrix system. In general, large precipitates originate mainly from the coarsening of smaller precipitates, or from small aggregates acting as capture sites for single atoms. Although the MD simulation

does not take into account the nucleation of precipitates and the coarsening, it is expected that larger precipitates prefer to stay at dislocations as well.

### 5.3.2 Kinetic factor

As a second step, the simulations of the diffusion–drift–aggregation processes of point defects have been carried out for a time of 4 h at 1000 °C by applying the model constructed in Sec. 2.5.2. The dislocation-core radius is taken as 7 Å. A capture radius of 14 Å for forming precipitates is used in the simulations. The possible size effect of precipitates on the diffusion–drift–aggregation processes is ignored. Sulfur with a concentration of  $C_S^{\text{eq}} = 2.0 \times 10^{18} \text{ cm}^{-3}$  is evenly distributed throughout the matrix regardless of the presence of dislocations at the initial time  $t = 0$ . Correspondingly,  $C_{\text{I}_{\text{As}}}^{\text{eq}}$ ,  $C_{\text{V}_{\text{Ga}}}^{\text{eq}}$  and  $C_{(\text{S}_{\text{As}}\text{V}_{\text{Ga}})^{2-}}^{\text{eq}}$  are estimated to be  $5.0 \times 10^{17} \text{ cm}^{-3}$ ,  $8.6 \times 10^{16} \text{ cm}^{-3}$ , and  $2.3 \times 10^{16} \text{ cm}^{-3}$ , respectively [84]. These initial concentrations have been selected on the assumption that point defects are in local thermal equilibrium at  $t = 0$ . The result of the simulations (Fig. 5.12) indicates that the concentration of  $\text{I}_{\text{As}}$  increases from the matrix to the dislocation within a short distance if no precipitate is formed at the dislocation ( $\gamma^* = 0$ ). This is known as a Cottrell atmosphere around the dislocation.\* Provided that the solubility of interstitial arsenic atoms at any position is assumed to be the same as that in the matrix ( $C_{\text{I}_{\text{As}}}^{\text{eq}}$ ), the aggregation of  $\text{I}_{\text{As}}$  at the dislocation increases the supersaturation ratio  $\Sigma$  and thus the probability to form arsenic precipitates according to the classic nucleation theory [see Eq. (2.45)]. It should be noticed that  $C_{\text{I}_{\text{As}}}/C_{\text{I}_{\text{As}}}^{\text{eq}}$  in the matrix is actually smaller than 1 since an increase of  $C_{\text{I}_{\text{As}}}$  at the dislocation must be accompanied by its reduction in the matrix in order to conserve the total amount of  $\text{I}_{\text{As}}$ . It is found that the increase in  $C_{\text{I}_{\text{As}}}$  near the dislocation is immediately followed by a depletion region at the early stage of the time evolution of the system (within 1 min). In the simulations, the arsenic atoms incorporated into arsenic precipitates are assumed to be immobile and are excluded from the calculations of  $C_{\text{I}_{\text{As}}}$ . So the formation of arsenic precipitates at the dislocation ( $\gamma^* = 1$ ) decreases the concentration of arsenic atoms available to the diffusion–drift–aggregation processes at any position from the dislocation, compared with the case  $\gamma^* = 0$  (see Fig. 5.12).

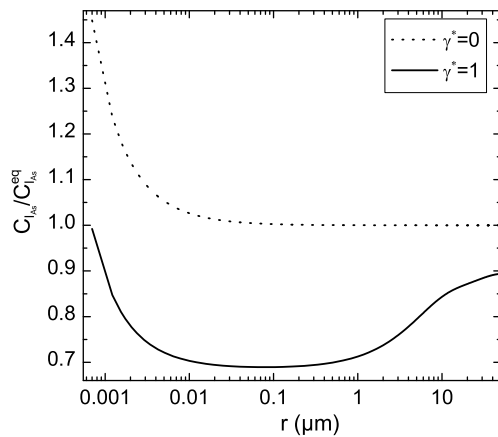
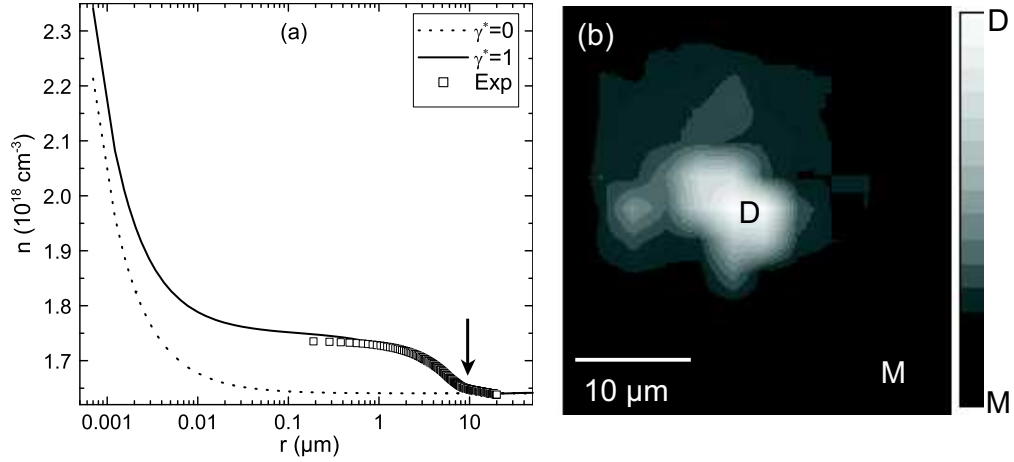


Figure 5.12: Simulated spatial distribution of interstitial arsenic from the matrix to the dislocation in GaAs:S without ( $\gamma^* = 0$ ) and with ( $\gamma^* = 1$ ) arsenic precipitates formed at the dislocation. The concentration  $C_{\text{I}_{\text{As}}}$  of interstitial arsenic is normalized to the local equilibrium concentration  $C_{\text{I}_{\text{As}}}^{\text{eq}}$  at initial time.  $r$  is the distance to the dislocation core. In all simulations, the dislocation core radius is taken as 7 Å.

The distinct increase in the free-electron concentration with no arsenic precipitate formed at the dislocation ( $\gamma^* = 0$ ) is limited to a small distance from the dislocation core [about 0.05  $\mu\text{m}$ , see Fig. 5.13(a)], which cannot explain the experimental findings by Raman microscopy. Raman scattering reveals that the radius of increased free-electron concentration around the dislocation amounts to about 10  $\mu\text{m}$  [Fig. 5.13(b)]. Experimentally, the free-electron concentration is deter-

\*More precisely, the atmosphere formed by interstitials is called Snoeck atmosphere while the aggregation of substitutional atoms at dislocations is called the Cottrell atmosphere [97].

mined by the peak position of the  $L^+$  mode in the Raman spectrum (see Secs. 3.1.3 and 5.1) [14]. The formation of arsenic precipitates ( $\gamma^* = 1$ ) in the simulation extends the radius of the increased free-electron concentration up to  $10 \mu\text{m}$  beyond the dislocation [see Fig. 5.13(a)], in agreement with the Raman scattering experiments. Therefore, the comparison of computer simulations with experiments states that the formation of arsenic precipitates at dislocations is essential for the spatial distribution of the free-electron concentration at dislocations.



*Figure 5.13:* (a) Simulated spatial distribution of the free-electron concentration in GaAs:S without ( $\gamma^* = 0$ ) and with ( $\gamma^* = 1$ ) arsenic precipitates formed at the dislocation. The experimental free-electron concentration (symbols) is obtained by averaging the free-electron concentrations over several directions from the dislocation in the two dimensional mapping in (b). The spatial distribution of the free-electron concentration (b) has been obtained by Raman microscopy in GaAs:S. It increases from  $1.64 \times 10^{18} \text{ cm}^{-3}$  in the matrix (M) to  $1.75 \times 10^{18} \text{ cm}^{-3}$  at the dislocation (D). Since the spatial resolution of the Raman microscope is above  $0.1 \mu\text{m}$ , the strong increase in the free-electron concentration for  $r < 0.01 \mu\text{m}$  in the theoretical calculation is not resolved in the experiment. For a better visualization of the long- and short-range effects, a log scale is used for  $r$  in (a). The arrow is drawn in (a) to guide the eye.

In conclusion, computer simulations elucidate that the formation of arsenic precipitates at the dislocation is energetically and kinetically preferred, compared to that in the matrix. Its formation is necessary to result in an extended region of the increased free-electron concentration. Finally, it should be mentioned that the interface energy between a precipitate and the GaAs matrix may be reduced due to the dislocation strain field to enhance further the formation of the precipitates at dislocations according to Eq. (2.45).

## 5.4 Computer simulations of spatial distribution of point defects

In this section, the effect of external conditions such as temperature and arsenic pressure on the spatial distribution of point defects from the matrix to the dislocation is theoretically elucidated. Starting from the diffusion–drift–aggregation model described in Sec. 2.5.2, the spatial distribution of point defects in GaAs:S with the evolution time, temperature, and arsenic pressure is discussed. The sulfur concentration at initial time is arbitrarily set as  $1.8 \times 10^{18} \text{ cm}^{-3}$  in all the simulations. This value does not affect the general understanding of the topics issued here. It is assumed that all of point defects are locally at equilibrium and are homogeneously distributed from the matrix to the dislocation at initial time. As mentioned in Sec. 5.3.2, the possible size effect of precipitates is ignored in the simulations. In fact, a change in the local volume of the host (GaAs) is expected

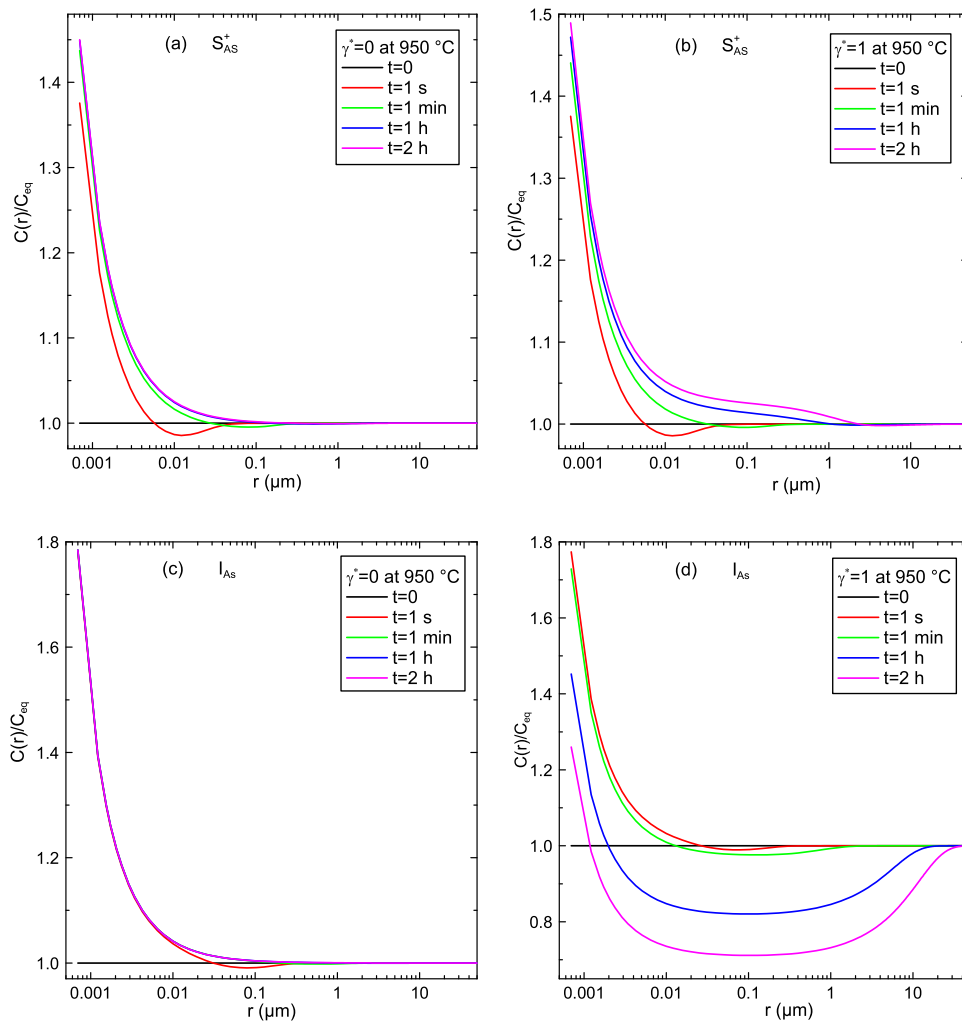


*Figure 5.14:* Spatial distribution of substitutional sulfur atoms ( $S_{\text{As}}^+$ ) from the matrix to the dislocation as a function of evolution time at 950 °C: (a) no arsenic precipitate is formed at the dislocation ( $\gamma^* = 0$ ); (b) arsenic precipitates are formed at the dislocation at a certain nucleation rate ( $\gamma^* = 1$ ). Spatial distribution of interstitial arsenic atoms ( $I_{\text{As}}$ ) from the matrix to the dislocation as a function of evolution time at 950 °C: (c) no arsenic precipitate is formed at the dislocation ( $\gamma^* = 0$ ); (d) arsenic precipitates are formed at the dislocation ( $\gamma^* = 1$ ).  $C(r)$  is the defect concentration at the distance  $r$  from the dislocation and  $C_{eq}$  is the local equilibrium concentration of corresponding point defects at initial time.

when precipitates are formed there. Therefore, a precipitate may give rise to either a compressive or tensile stress field, in addition to that originating from the dislocation, according to whether there is an increase or a decrease in volume, respectively. As a result, the force exerted on point defects through the stress field can be changed more or less (see Sec. 2.2).

#### 5.4.1 Time evolution of the system

The simulations were made firstly under the condition of 1 atm arsenic pressure. Fig. 5.14 shows that the increase in the number of  $S_{As}^+$  at the dislocation is followed immediately by a depletion region at the early stage ( $t < 1$  min) whenever there are arsenic precipitates formed at the dislocation or not. A depletion region is pronouncedly formed from the initial time ( $t = 0$ ) to  $t = 1$  s and its depth reaches maximum at  $t = 1$  s. Evolving from  $t = 1$  s to  $t = 1$  min, the depletion region is gradually shifting outwards the dislocation and its depth is reducing (compare the curve at  $t = 1$  s with the one at  $t = 1$  min) until it is eventually eliminated. The system with no arsenic precipitate formed at the dislocation ( $\gamma^* = 0$ ) reaches quickly a new equilibrium state within 1 h. A Cottrell atmosphere with an extension of  $0.1 \mu\text{m}$  is formed at the dislocation [see Fig. 5.14(a)]. As discussed in Sec. 2.2, the amount of  $S_{As}^+$  in the new equilibrium state obeys the Maxwell distribution from the matrix to the dislocation. However, the formation of arsenic precipitates ( $\gamma^* = 1$ ) extends the radius of point-defect atmosphere up to  $4 \mu\text{m}$  after 2 h while no equilibrium state can be expected in this case. In the evolution from 1 min to 2 h, the sulfur concentration at the dislocation is actually enhanced and the radius of the enhancement is extended continuously from  $0.05 \mu\text{m}$  after 1 min,  $1 \mu\text{m}$  after 1 h to  $4 \mu\text{m}$  after 2 h [see Fig. 5.14(b)]. Experimentally, when the system is cooled down quickly from high to low temperatures, the diffusivity of each species of point defects rapidly decreases so that their spatial distribution from the matrix to the dislocation keeps nearly the properties at high temperatures. Therefore, the simulations are equivalent to an annealing at  $900 \text{ }^\circ\text{C}$  for 2 h and a rapid cooling to room temperature.

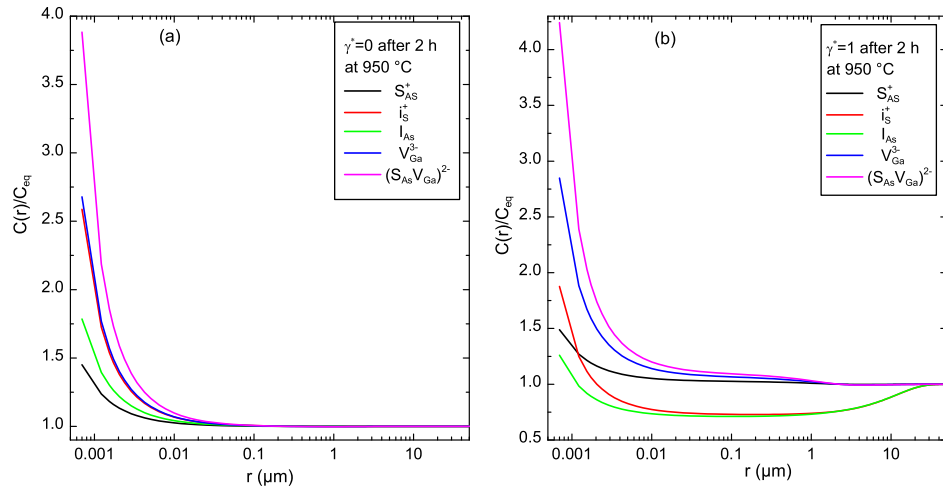


Figure 5.15: Spatial distribution of various defects from the matrix to the dislocation after evolving for 2 h at  $950 \text{ }^\circ\text{C}$ . (a) No arsenic precipitate is formed at the dislocation ( $\gamma^* = 0$ ); (b) arsenic precipitates are formed at the dislocation ( $\gamma^* = 1$ ).  $C(r)$  is the defect concentration at the distance  $r$  from the dislocation and  $C_{eq}$  is the local equilibrium concentration of corresponding point defects at initial time.

It is also the case for interstitial arsenic atoms to form a depletion region at the early stage of the time evolution when no arsenic precipitate is formed at the dislocation ( $\gamma^* = 0$ ). The formation of arsenic precipitates ( $\gamma^* = 1$ ) enhances the formation of the depletion region of interstitial arsenic

atoms, as shown in Fig. 5.14(d), where  $C_{I_{As}}(r)$  at the same position from the dislocation decreases while the depth and extension of the depletion are growing larger with time (see Fig. 5.14).

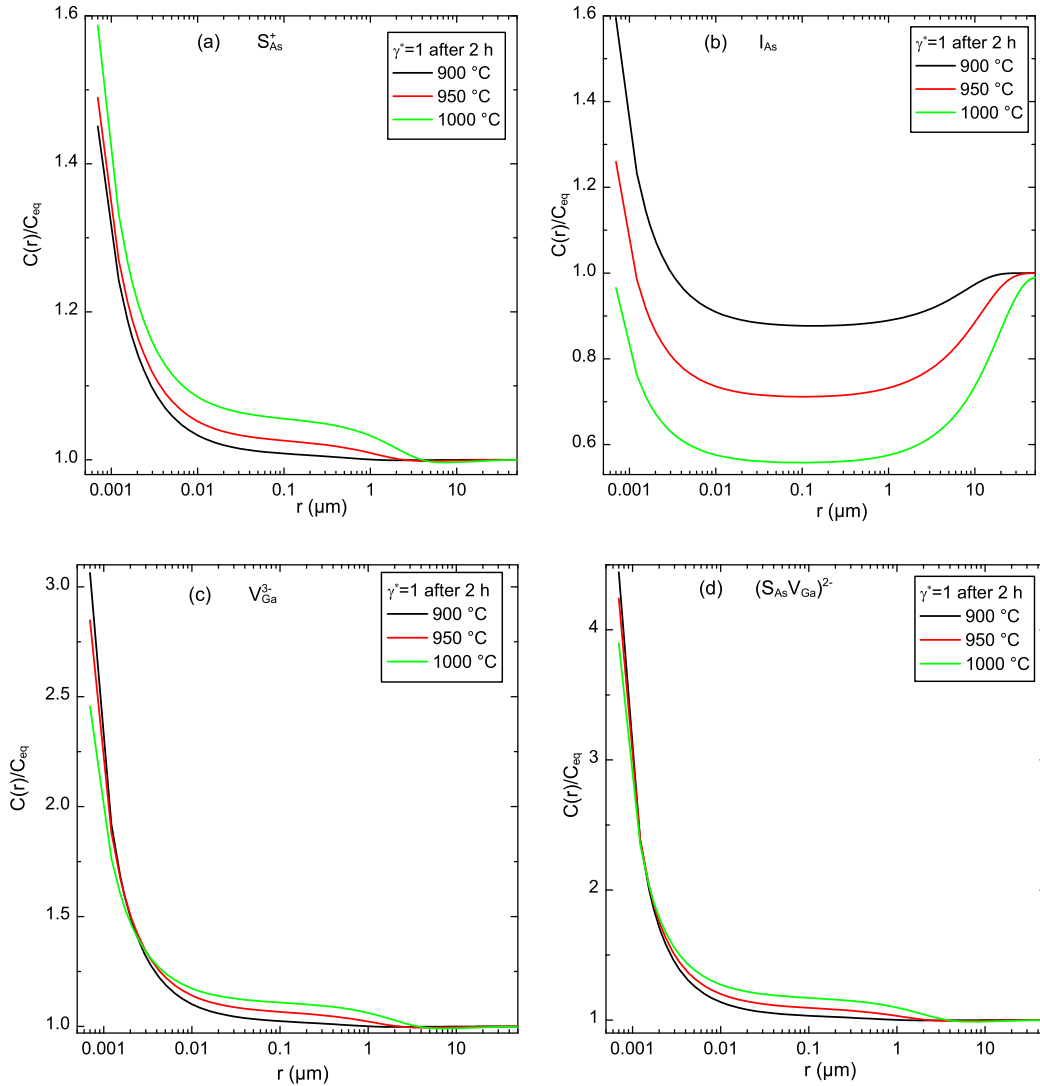


Figure 5.16: Spatial distribution of (a)  $S_{As}^+$ , (b)  $I_{As}$ , (c)  $V_{Ga}^{3-}$ , and (d)  $(S_{As}V_{Ga})^{2-}$  from the matrix to the dislocation as a function of temperature after evolving for 2 h with arsenic precipitates formed at the dislocation at a certain nucleation rate ( $\gamma^* = 1$ ).  $C(r)$  is the defect concentration at the distance  $r$  from the dislocation and  $C_{eq}$  the local equilibrium concentration of corresponding point defects at initial time.

Under the condition that no arsenic precipitate is formed at the dislocation ( $\gamma^* = 0$ ), the system reaches completely the equilibrium, and the concentration of various defects increases from the matrix to the dislocation with a small increased radius ( $< 0.1 \mu\text{m}$ ) after time evolution of 2 h (see Fig. 5.15). This aggregation of point defects around the dislocation due to their interaction is usually characterized as a Cottrell atmosphere with a narrow extension. The formation of arsenic precipitates ( $\gamma^* = 1$ ) results in an increase in the concentration of  $S_{As}^+$ ,  $V_{Ga}^{3-}$  and  $(S_{As}V_{Ga})^{2-}$  with an extended radius of  $4 \mu\text{m}$  but different amplitudes from the matrix to the dislocation, and in a strong depletion following an increase in the concentrations of  $i_S^+$  and  $I_{As}$  around the dislocation. In addition to the effect from the interaction of point defect with dislocations, the increase in the concentration of  $S_{As}^+$ ,  $V_{Ga}^{3-}$ , and  $(S_{As}V_{Ga})^{2-}$  comes partly from the contribution of the formation

of arsenic precipitates ( $\gamma^* = 1$ ) so that their amplitudes at the dislocation are higher than that for  $\gamma^* = 0$  [compare Figs. 5.15(a) and (b)]. This confirms definitely the former conclusion from TEM observations that the formation of arsenic-precipitates is correlated with the agglomeration of gallium vacancies [44].

Fig. 5.16 shows that the aggregation of  $S_{As}^+$ ,  $V_{Ga}^{3-}$ , and  $(S_{As}V_{Ga})^{2-}$  around the dislocation is enhanced, while the depletion in  $I_{As}$  becomes more significant with increasing temperature due to the formation of arsenic precipitates.

#### 5.4.2 As-pressure effect

In the following, the arsenic-pressure dependent concentration of intrinsic point defects already discussed in Sec. 2.4 is treated in detail to elucidate its influence on the spatial distribution of various defects from the matrix to the dislocation. From the mass-conservation law over reaction (2.35), a relationship

$$\frac{C_{S_{As}^+}^{eq} C_{I_{As}}^{eq}}{C_{i_S^+}^+} = \text{constant} \quad (5.10)$$

can be obtained, whatever the external condition such as temperature and arsenic pressure is. Table. 2.1 indicates that

$$C_{I_{As}}^{eq}(p_{As_4}) = p_{As_4}^{1/4} C_{I_{As}}^{eq}(p_{As_4} = 1 \text{ atm}). \quad (5.11)$$

Since  $C_{S_{As}^+}^{eq}$  is always far larger than  $C_{i_S^+}^+$ ,  $C_{S_{As}^+}^{eq}$  is approximately equal to the concentration of all sulfur atoms, which can be manually controlled provided that it is below its solubility limit. Thus,  $C_{S_{As}^+}^{eq}$  is independent of the arsenic pressure and  $C_{i_S^+}^+(p_{As_4}) = p_{As_4}^{1/4} C_{i_S^+}^+(p_{As_4} = 1 \text{ atm})$  from Eqs. (5.10) and (5.11). Since the diffusion coefficient  $D_{i_S^+}$  of sulfur interstitials is always lower than that of arsenic interstitials, the diffusion via the kick-out mechanism proceeds under equilibrium or quasi-equilibrium conditions of arsenic interstitials, except for the case of high sulfur concentrations ( $> 10^{19} \text{ cm}^{-3}$ ). Otherwise, the diffusion is under non-equilibrium conditions of arsenic interstitials so that a significant supersaturation of arsenic interstitials occurs [84]. The effective diffusion coefficient of sulfur atoms under the (quasi)-equilibrium or non-equilibrium conditions of arsenic interstitials is respectively expressed as

$$D_S^{eff.eq} = \frac{D_{i_S} C_{i_S}^{eq}}{C_S^{eq}}, \quad (5.12)$$

and

$$D_S^{eff.noneq} = \frac{D_{I_{As}} C_{I_{As}}^{eq}}{C_S^{eq}} \left( \frac{C_S^{eq}}{C_S} \right)^2. \quad (5.13)$$

Therefore,  $D_S^{eff}(p_{As_4}) = p_{As_4}^{1/4} D_S^{eff}(p_{As_4} = 1 \text{ atm})$ . The arsenic pressure also influences the arsenic and gallium diffusivity.  $D_{As}^I = D_{I_{As}} C_{I_{As}}^{eq} / C_0$  represents the contribution of  $I_{As}$  to the arsenic diffusion while  $D_{Ga}^V = D_{V_{Ga}} C_{V_{Ga}}^{eq} / C_0$  represents the contribution of  $V_{Ga}$  to the gallium diffusion in GaAs. Here  $C_0 = 2.215 \times 10^{22} \text{ cm}^{-3}$  denotes the density of arsenic or gallium sublattice sites. Since  $C_{I_{As}}^{eq} \propto P_{As}^{1/4}$  and  $C_{V_{Ga}}^{eq} \propto P_{As}^{1/4}$  (see Table. 2.1),

$$D_{As}^I(p_{As_4}) = p_{As_4}^{1/4} D_{As}^I(p_{As_4} = 1 \text{ atm}), \quad (5.14)$$

and

$$D_{Ga}^V(p_{As_4}) = p_{As_4}^{1/4} D_{Ga}^V(p_{As_4} = 1 \text{ atm}). \quad (5.15)$$

are obtained.

Fig. (5.17) indicates that the aggregation of  $S_{As}^+$ ,  $V_{Ga}^{3-}$  and  $(S_{As}V_{Ga})^{2-}$  around the dislocation is enhanced, while the depletion in  $I_{As}$  becomes more pronounced with increasing arsenic pressure. At 1000 °C, the arsenic pressure under Ga-rich conditions is  $6.6 \times 10^{-5}$  atm given by the expression [121].

$$p_{As_4}(\text{Ga-rich}) = 3.38 \times 10^{16} \exp(-5.35 \text{ eV}/k_B T). \quad (5.16)$$

Comparison of Fig. (5.16) with Fig. (5.17) indicates that temperature and arsenic pressure play a similar role. That is, a higher temperature or a higher arsenic pressure leads to a stronger aggregation of  $S_{As}^+$ ,  $V_{Ga}^{3-}$  and  $(S_{As}V_{Ga})^{2-}$  around the dislocations, accompanied by a broader extension

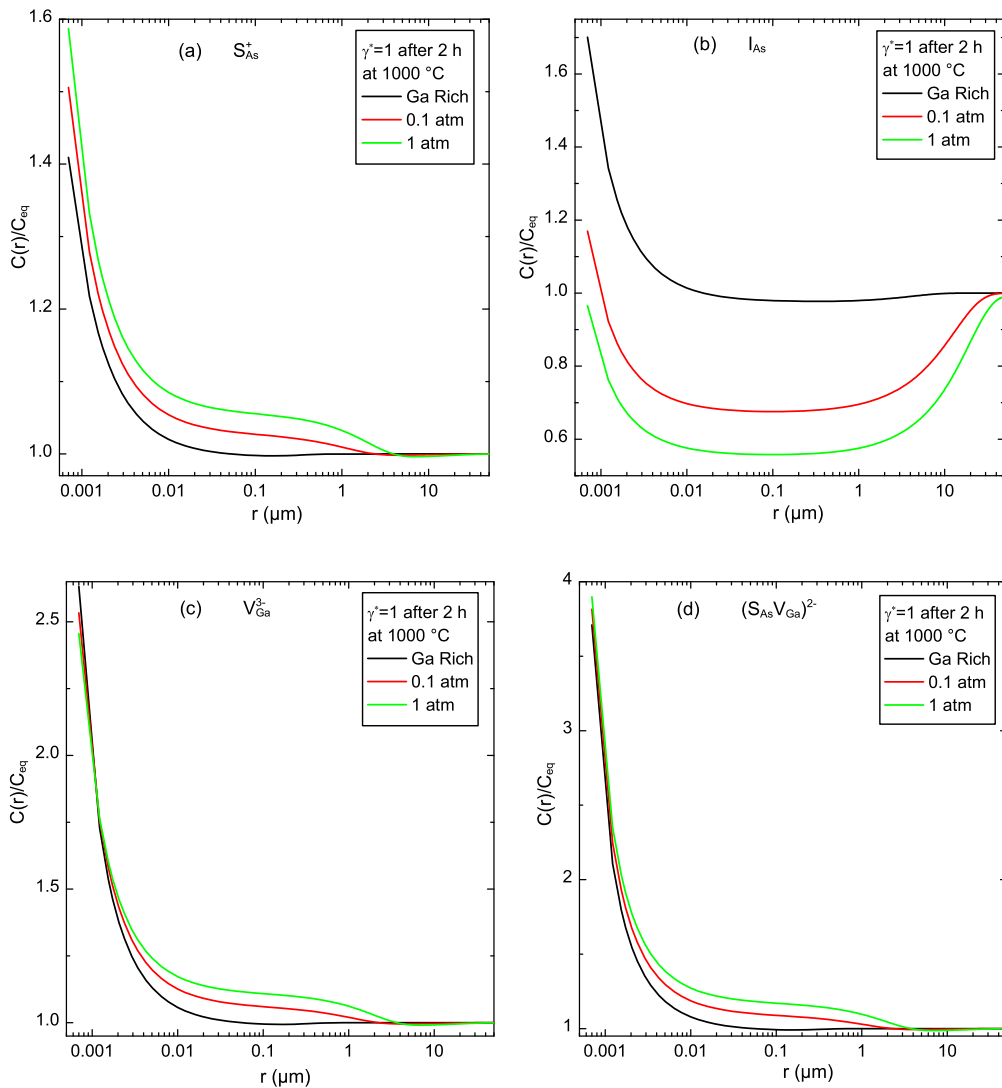


Figure 5.17: Spatial distribution of (a)  $S_{As}^+$ , (b)  $I_{As}$ , (c)  $V_{Ga}^{3-}$ , and (d)  $(S_{As}V_{Ga})^{2-}$  from the matrix to the dislocation as a function of the arsenic pressure after evolving for 2 h at 1000 °C with arsenic precipitates formed at the dislocation ( $\gamma^* = 1$ ).  $C(r)$  is the defect concentration at the distance  $r$  from the dislocation and  $C_{eq}$  is the local equilibrium concentration of corresponding point defects at initial time.

in the aggregation area, and to a deeper and broader depletion in the number of interstitial arsenic atoms beyond the dislocations.

It must be noted that dopant-related precipitates such as  $\text{Ga}_2\text{S}_3$  or  $\text{As}_2\text{S}_3$  may be formed at the dislocation in heavily doped GaAs, because the aggregation of dopants at the dislocation can easily lead to an increase in the dopant concentration above its solubility limit and thus the formation of precipitates according to Eq. (2.45). In the present simulations, the climb of dislocations was neglected. The so-called Petroff–Kimerling mechanism has not been incorporated in evaluating the effect of the dislocations on spatial distribution of point defects. The Petroff–Kimerling mechanism indicates that dislocation climb causes absorption of Ga vacancies (As interstitials) plus the simultaneous emission of As interstitials (Ga vacancies) [33]. The absorption or emission of vacancies may increase or decrease the local stress around the dislocation and affect the interaction of point defects with dislocations.

As a summary, the simulations presented here indicate that the aggregation amplitude of point defects around the dislocations depends on several factors such as their diffusivity, the rate of forming precipitates, annealing temperature, and evolution time as well as vapor pressure.



## 6 Identification of luminescence bands in n-type GaAs

The defect-related luminescence bands in the range of 0.95–1.30 eV in n-type GaAs doped, e.g., with silicon, sulfur, or tellurium have been known for a long time, but their origins are still controversial. The defect-related luminescence bands at 0.95 eV in n-type GaAs was suggested to be correlated to acceptors [99, 100], to the  $V_{As}Si_{Ga}V_{Ga}$  complexes [101] or to the  $Si_{Ga} - Si_{As}$  pairs [102]. Most theoretical calculations [81] and experiments [121, 122] predicted that negative gallium vacancies are dominant vacancies in n-type GaAs while positive arsenic vacancies were found to exist in a significant amount in undoped and lightly doped n-type GaAs [103]. Isolated gallium vacancies usually combine with donors by Coulomb interactions to form donor- $V_{Ga}$  complexes. The donor- $V_{Ga}$  complexes are frequently related to the luminescence band around 1.20 eV [68]. However, several research groups have identified that the band seemingly related to the donor- $V_{Ga}$  complexes can be located at very different energy positions, from 1.10 eV to 1.30 eV [68–71]. The big difference may originate, on the one hand, from sample treatments during preparation, and on the other hand, from different doping levels. Systematic investigations of the effect of these factors on the luminescence are not available. So it is not clear whether the luminescence bands observed are really related to donor-Ga vacancy complexes. Therefore, further efforts are necessary to elucidate from what kind of defects the bands really originate. In this chapter, at first, n-type GaAs:Si is dealt with to determine the origin of the 0.95 eV band, and then GaAs:S is investigated with respect of the effect of the doping level on the luminescence. A suggestion is presented which defects are responsible for the 1.30 eV band.

### 6.1 Luminescence bands in n-type GaAs:Si

Two kinds of n-type GaAs:Si wafers (No. n3# and w2#) were grown by the VGF technique. The wafers were supplied by Freiburger Compound Materials. The average free-electron concentration was determined by Hall effect measurements to be  $1.0 \times 10^{17} \text{ cm}^{-3}$  and  $7.8 \times 10^{17} \text{ cm}^{-3}$  in the samples n3# and w2#, respectively. The total silicon and boron concentrations in w2# were determined by SIMS to be  $1.5 \times 10^{18} \text{ cm}^{-3}$  and  $5.5 \times 10^{18} \text{ cm}^{-3}$ . The samples were investigated by CL microscopy at temperatures from 20 to 100 K. Positron lifetime spectroscopy was performed by using a conventional fast-fast spectrometer at temperature from 30 K to 500 K. A  $^{22}\text{NaCl}$  source was deposited on a thin aluminum foil and placed between a sandwich of identically treated samples. More than  $1.0 \times 10^7$  events were collected for a complete positron lifetime spectrum. The annihilation-momentum distribution of positrons was measured by Doppler broadening coincidence spectroscopy using a setup of two Ge detectors.

The luminescence bands in the samples n3# and w2# are shown in Fig. 6.1(a). The band A at 1.50 eV is due to the NBE emission; the band B at 1.33 eV originates from the transition from states near conduction band to  $B_{As}^-$  states, i.e.  $(eB_{As}^-)$  [82]; the band C at 1.14 eV is connected to  $(Si_{Ga}V_{Ga})^{2-}$  complexes [68–71]. The origin of the band D at 0.95 eV can not be determined at this stage. It might be related to  $(V_{Ga}Si_{Ga}V_{As})$  complexes [101], to  $Si_{Ga} - Si_{As}$  pairs [102] or to others. For convenience, later we call this defect X. The band C correlated to the  $(Si_{Ga}V_{Ga})^{2-}$

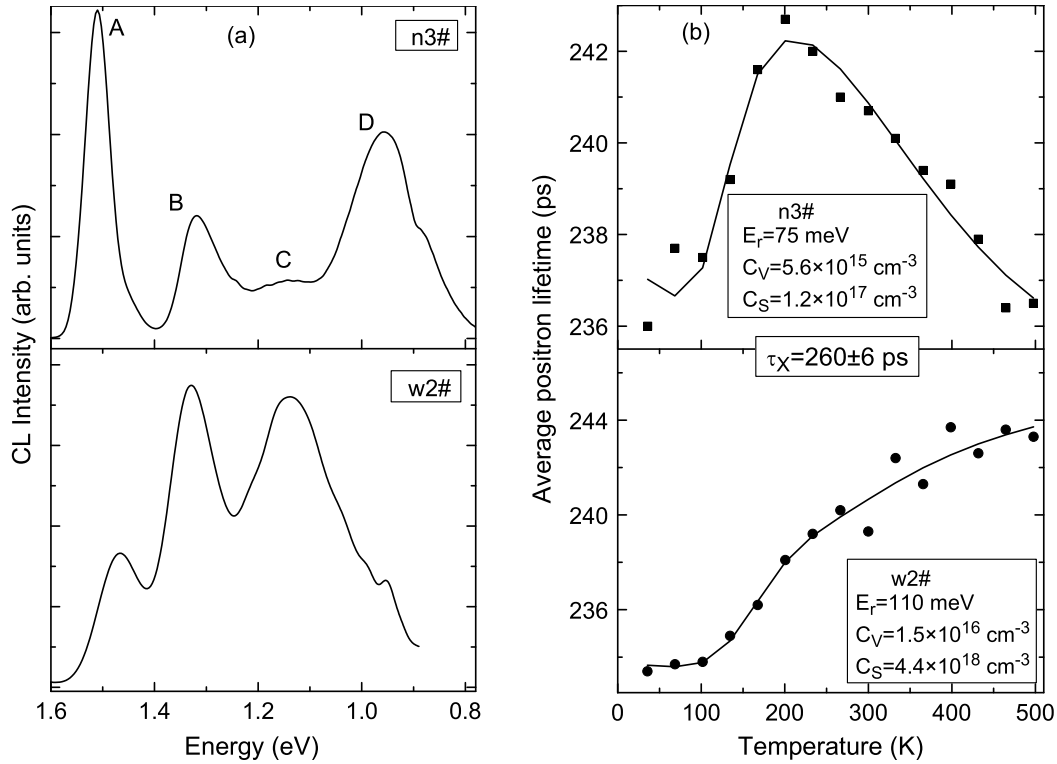


Figure 6.1: (a) CL spectra of GaAs:Si taken by the Ge detector at 75 K. (b) Average positron lifetime as a function of temperature. The symbols are experimental data and the lines are the results of fit. The CL spectra are not corrected according to the sensitivity of the Ge detector used.

complexes is much stronger in the sample w2# than in n3#. As a matter of fact, the band A has shifted from 1.51 eV in n3# to 1.47 eV in w2#. The reason may be a higher doping level (see Fig. 3.6) and a higher concentration of shallow-level  $B_{As}^0$  acceptors (71 meV above the valence band) in w2#. A large number of boron atoms ( $5.5 \times 10^{18}$  cm $^{-3}$ ) in w2# result in a high intensity of the band B. It is worth noting that boron may form a neutral acceptor ( $B_{As}^0$ ) or a singly charged one ( $B_{As}^-$ ). As it will be revealed by positron lifetime spectra, the concentration of shallow positron traps, mainly attributed to  $B_{As}^-$  acceptors, is about  $4.4 \times 10^{17}$  cm $^{-3}$  in w2#, much higher than the concentration of shallow positron traps with  $1.2 \times 10^{16}$  cm $^{-3}$  in n3#. This is the reason why the sample w2# is still n-type despite a lower silicon concentration ( $1.5 \times 10^{18}$  cm $^{-3}$ ) than the boron concentration ( $5.5 \times 10^{18}$  cm $^{-3}$ ).

Positron lifetime spectra were processed to study further the characters of defects in the samples n3# and w2#. Fig. 6.1(b) shows a typical temperature dependence of the average positron lifetime. It can be explained by positrons trapped in negatively charged vacancies in competition to trapping in shallow positron traps [104]. The trapping coefficient of negatively charged vacancies decreases with increasing temperature due to the temperature dependence of the diffusion-limited trapping so that the average positron lifetime decreases with increasing temperature above 200 K in sample n3#. Below 200 K, the effect of shallow traps becomes dominant, and the average positron lifetime decreases with decreasing temperature. The two-component lifetime fitting gives the positron lifetime of vacancy-related defects  $\tau_X = 260 \pm 6$  ps. This is the same as the value at  $V_{Ga}$  or  $(Si_{Ga}V_{Ga})$  complexes [105]. It can thus be deduced that the dominating defects X responsible for the band D includes a negatively charged vacancy. It is certainly a gallium vacancy because an arsenic vacancy is always positively charged in n-type bulk GaAs [106]. Theoretical calculations showed that the positron lifetime at  $(V_{As}Si_{Ga}V_{Ga})$  complexes is about 320 ps [105], far larger

than the value of 260 ps measured here. Therefore, it is concluded that there is no arsenic vacancy included in X. From the different pressure dependence of the polarizations for the band D in n-type GaAs doped with different donors, Reshchikov et al. concluded that the main dopant ( $\text{Si}_{\text{Ga}}^+$  here) is one component constituting X [101].

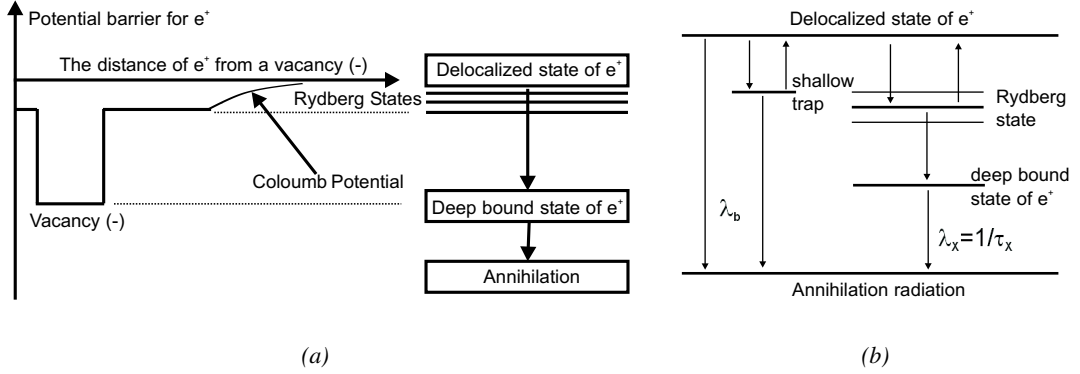


Figure 6.2: (a) Scheme of the positron potential for a negatively charged vacancy. The shallow Rydberg states acting as precursor trapping states are indicated. (b) Scheme of the two-stage trapping into a negatively charged vacancy. The positron may also annihilate through shallow positron traps at the nearly same annihilation rate  $\lambda_b$  as that in defect-free bulk. A negatively charged vacancy results in both Rydberg states and a deep bound state to capture positrons.

The course of the average positron lifetime in the sample w2# is similar to that in the sample n3# below 200 K. A fit of the temperature dependence of the average positron lifetime has been made for both samples. This fit is based on the model of competitive trapping and detrapping in a shallow positron trap and a negatively charged vacancy [104, 107]. The characteristic quantities of the fit are the positron binding energy  $E_r$  to the Rydberg state of the vacancy, the concentration of shallow positron traps, and the concentration of the vacancy-related defects X. The Coulomb interaction between a negatively charged vacancy and a positron gives rise to Rydberg states acting as precursor positron traps for the deep bound state of the vacancy (see Fig. 6.2). In the fitting, not a series of Rydberg states, but only one effective shallow state with the positron binding energy  $E_r$  is assumed. A stronger Coulomb potential between a positron and a negatively charged vacancy shifts down the potential barrier for positrons, and thus results in deeper Rydberg states and a larger  $E_r$ . Considering positron trapping and detrapping at the shallow positron traps and the Rydberg states according to the model of Ref. [107], the fit of the average positron lifetime gives  $E_r = 110$  meV for w2# and  $E_r = 75$  meV for n3#. Therefore, the charge state of X in n3# should be smaller than 2-, which corresponds to the charge state of a  $(\text{Si}_{\text{Ga}}\text{V}_{\text{Ga}})$  complex in w2# [81, 120–122]. Taking into account the concrete condition in n-type GaAs:Si, it is suggested that  $\text{Si}_{\text{Ga}}^+$  be one component of X. As a result, X must consist of a gallium vacancy ( $\text{V}_{\text{Ga}}$ ) and two  $\text{Si}_{\text{Ga}}^+$  donors forming a  $(\text{Si}_{\text{Ga}}\text{V}_{\text{Ga}}\text{Si}_{\text{Ga}})^-$  complex. Although a gallium site has twelve nearest-neighbor gallium sites, the Coulomb repulsion between the two  $\text{Si}_{\text{Ga}}^+$  donors separates them in a distance as large as possible to result in a linear atomic structure of a  $(\text{Si}_{\text{Ga}}\text{V}_{\text{Ga}}\text{Si}_{\text{Ga}})^-$  complex. The distance between the two  $\text{Si}_{\text{Ga}}^+$  donors is  $\sqrt{2}a$  and  $\text{V}_{\text{Ga}}$  lies at the midpoint between them, as shown in Fig. 6.3(b). The fit of the positron lifetime additionally indicates that the concentrations of gallium vacancies ( $C_V$ ) and shallow positron traps dominated by  $\text{B}_{\text{As}}^-$  ( $C_S$ ) are higher in w2# than in n3# [see Fig. 6.1(b)].

In order to acquire more information on positron annihilation at gallium vacancies, positron annihilation-momentum distribution was measured at 200 K for n3# and at 400 K for w2# by

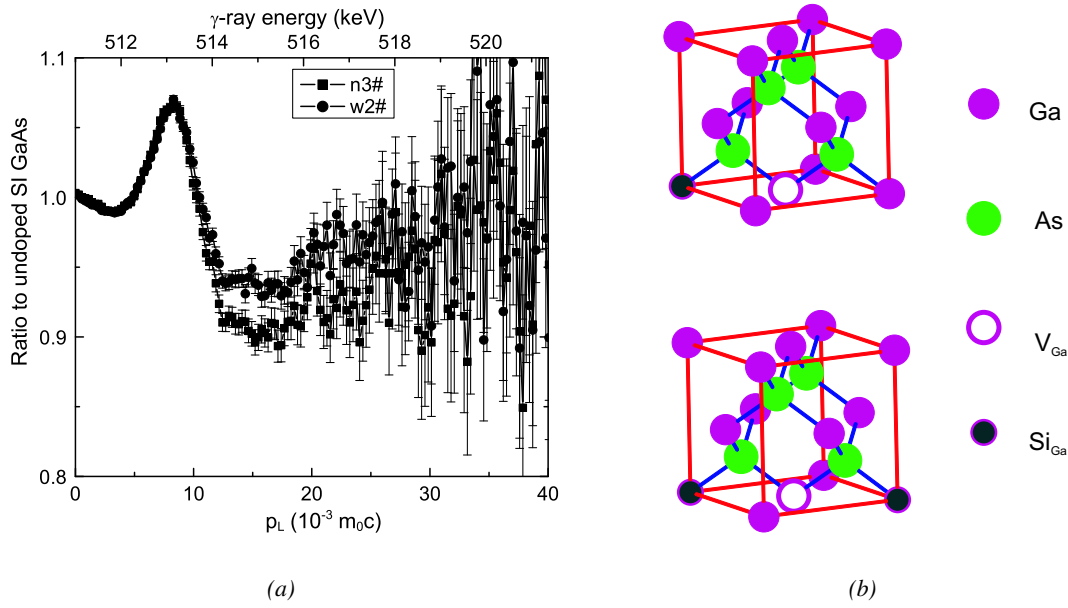


Figure 6.3: (a) Positron annihilation momentum distribution measured at 200 K for sample n3# and at 400K for sample w2#. The intensity is normalized by taking the ratio to undoped semi-insulating (SI) GaAs reference. (b) The atomic configurations of  $(\text{Si}_{\text{Ga}} \text{V}_{\text{Ga}})$  (above) and  $(\text{Si}_{\text{Ga}} \text{V}_{\text{Ga}} \text{Si}_{\text{Ga}})$  (below).

Doppler-broadening coincidence spectroscopy. The temperatures chosen correspond to maximum trapping in vacancies, as shown in Fig. 6.1(b). Fig. 6.3 shows the positron annihilation-momentum distribution in the samples w2# and n3#. The data are normalized by taking the ratio to undoped semi-insulating GaAs reference. In semi-insulating GaAs, there is no positron trapping in defects, thus representing the positron-annihilation character in bulk GaAs. In a vacancy, the fraction of valence electrons taking part in the annihilation process increases to result in a narrower momentum distribution with a higher annihilation intensity at low annihilation momentum (i.e.  $p_L < 10 \times 10^{-3} m_0 c$ ), compared to that in the bulk GaAs ( $m_0$  is the positron rest mass). At high annihilation momentum ( $p_L > 10 \times 10^{-3} m_0 c$ ), the positron annihilation with the core electrons is much more intense than with valence electrons. The core electrons are tightly bound to the nuclei and thus the high-momentum part of the positron annihilation momentum reflects the chemical environment where the annihilation event takes place. In bulk GaAs, the dominant contribution to the core annihilation comes from 3d electrons of Ga and As atoms. The core annihilation at Ga 3d is stronger than at As 3d [108]. The positron annihilation at a gallium vacancy occurs mainly with 3d electrons of As atoms which are closest to this gallium vacancy. Therefore, the intensity of the high momentum at the two kinds of complexes is smaller than the one in bulk GaAs, as shown in Fig. 6.3(a). The chemical environments at  $(\text{Si}_{\text{Ga}} \text{V}_{\text{Ga}})$  and  $(\text{Si}_{\text{Ga}} \text{V}_{\text{Ga}} \text{Si}_{\text{Ga}})$  are almost the same so that their momentum distributions are very similar.

The luminescence bands in the sample n3# were measured at temperatures from 20 K to 100 K. Their CL intensities are shown in Fig. 6.4 as a function of temperature. It is obtained that the CL intensities of the four bands always follow an approximately exponential decay with increasing temperature, as expected by the relationship

$$I = I_0 [1 + f \cdot \exp(-\Delta E/k_B T)]^{-1}. \quad (6.1)$$

where  $f$  is a temperature-independent constant.  $\Delta E$  represents an activation energy for thermal

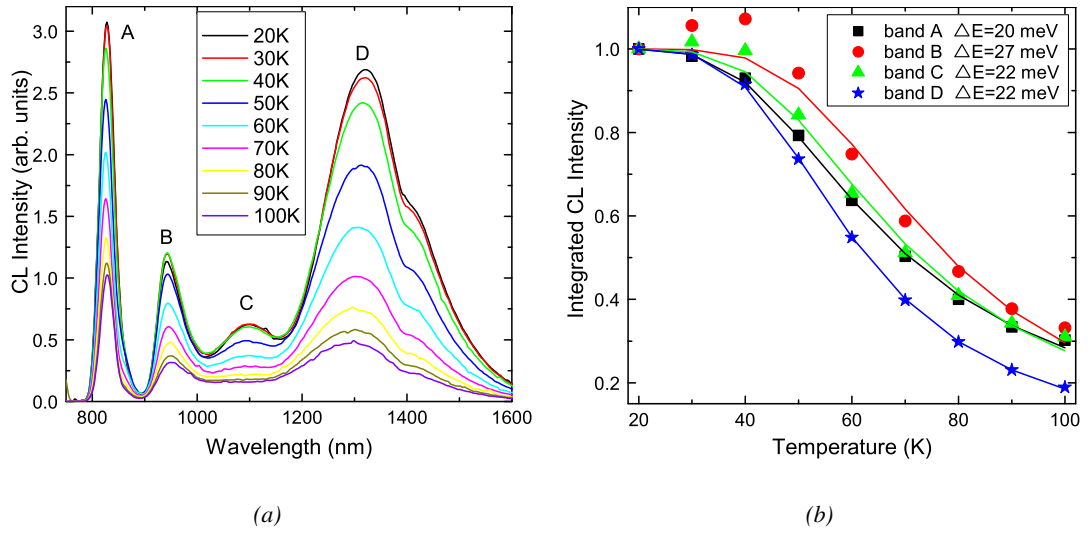


Figure 6.4: CL intensity as a function of temperature in the sample n3# taken by the Ge detector. The spectra in (a) are not corrected according to the sensitivity of the Ge detector. The integral CL intensity in (b) has been normalized to the one at 20 K. The symbols represent experimental data and line the fit based on Eq. (6.1).

quenching processes. Eq. (6.1) states that the CL intensity of the luminescence band decays with temperature in the form of Fermi–Dirac-like statistics [109], which is consistent with the statistic characters of the electrons and holes. But this fit on the band C is inconsistent with that by Williams [68] and by Sauncy et al [70], who obtained a Boltzmann-type decay with temperature. From a least square fit of the experimental data,  $\Delta E$  for the different luminescence bands have been obtained and they are almost the same (see Fig. 6.4). In addition to the possible increase in the fraction of non-radiative transitions with temperature, i.e.  $\tau_e/\tau_{rad}$  decreases with increasing temperature [110], the decrease in the number of the electron–hole pairs available to the radiative recombinations in unit volume due to an enhanced thermal activation may reduce the CL intensity of the bands. As a matter of fact, if we assume that the radiative recombination over a certain path involves at least a trap in the band gap which captures a electron or a hole,  $\Delta E$  can be understood as the energy level of the trap lying below the conduction band, above the valence band, or the activation energy for a non-radiative relaxation process in terms of the configurational coordinate model [68, 70] (also see Fig. 6.8 in Sec. 6.2).

In general, the band C is due to the transition from the upper (excited state) to lower (ground state) energy level of a molecule-like ( $\text{Si}_{\text{Ga}}\text{V}_{\text{Ga}}$ ) complex [68, 70]. The lower energy level of the molecule-like ( $\text{Si}_{\text{Ga}}\text{V}_{\text{Ga}}$ ) complex is a deep state, at about 0.3 eV above the valence band [70]. Thus, it is difficult for the hole trapped in the complex to escape from this level to the valence band. So it must be the electron lying  $\Delta E$  below the conduction band which are thermally activated and enter the conduction band in the probability given by Eq. (6.1). This reduces the number of the electrons available to the radiative transitions and suppresses the intensity of the luminescence band C with temperature. In other words, Fig. 6.4(b) implies that the upper level of a ( $\text{Si}_{\text{Ga}}\text{V}_{\text{Ga}}$ ) complex lies at 22 meV below the conduction band. Similarly, the upper level of a ( $\text{Si}_{\text{Ga}}\text{V}_{\text{Ga}}\text{Si}_{\text{Ga}}$ ) complex is estimated at 22 meV below the conduction band and the lower level at about 0.5 eV above the valence band. The analysis indicates additionally that the lower level of a molecule-like ( $\text{Si}_{\text{Ga}}\text{V}_{\text{Ga}}$ ) or a ( $\text{Si}_{\text{Ga}}\text{V}_{\text{Ga}}\text{Si}_{\text{Ga}}$ ) complexes is different from the energy level of an isolated  $\text{V}_{\text{Ga}}$ .

The detailed examination of the peak energy position of each band (see Fig. 6.5) indicates that

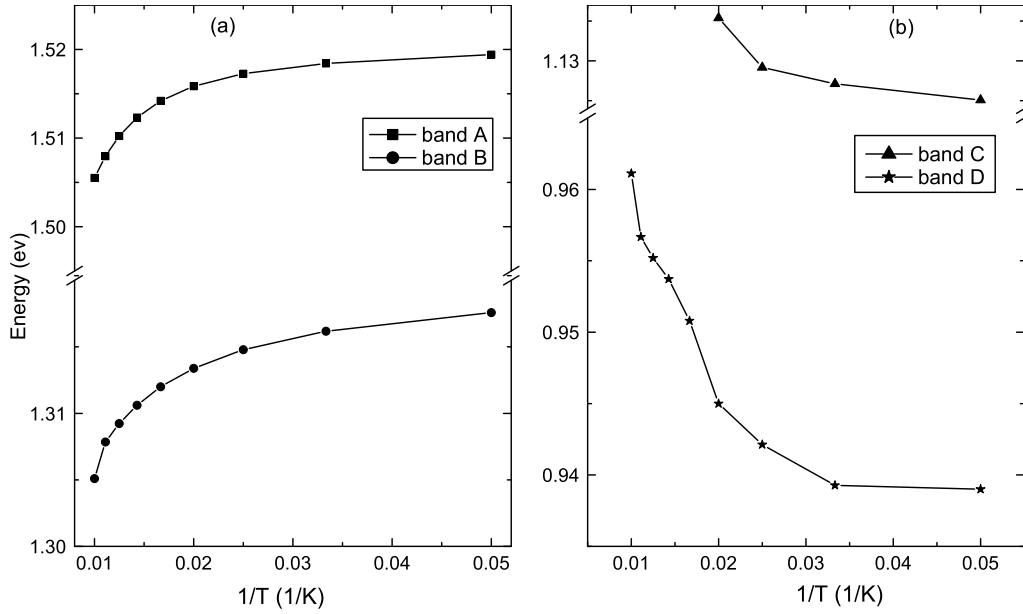


Figure 6.5: Energy position of each luminescence band on the sample n3# as a function of inverse temperature.

the peak positions of the NBE and ( $eB_{As}^-$ ) bands shift to lower energies with increasing temperature similar to the band gap. Unlike the band gap, the peaks positions of both bands C and D shift to higher energies with increasing temperature. This implies that the effect of the temperature on the energy levels responsible for the two bands C and D is different from that for the band gap. Since the CL intensity of the band C is too weak to be distinguished at the temperature above 50 K, no peak position is given in Fig. 6.5(b). The shallow donor (acceptor) levels are known to shift rigidly with the conduction (valence) bands [111]. Since the upper level of the complex is a shallow level below the conduction band and its lower level is a deep level, it should be the lower level that shifts down towards the valence band with increasing temperature to result in the blue shifts of the bands C and D.

In conclusion, the combination of CL with positron annihilation suggests that there are two possible kinds of the gallium vacancy-related complexes,  $(Si_{Ga}V_{Ga})^{2-}$  and  $(Si_{Ga}V_{Ga}Si_{Ga})^-$ . They result in the luminescence bands at 1.14 eV and at 0.95 eV in n-type GaAs:Si, respectively. The ground states (the lower level) of the two kinds of complexes lie at 0.3 eV and 0.5 eV, respectively, above the valence band. Their excited states (the upper level) are shallow levels, about 20 meV below the conduction band. It is well known that light with the wavelengths ranging from 1300 nm (0.96 eV) to 1550 nm (0.80 eV) traveling through quartz fibers suffers minimum energy loss. So the existence of the band at 0.95 eV allows GaAs to be applied in the field of optical-fiber communications. Further efforts are necessary to systematically explore which conditions are essential to grow GaAs that can result in a strong luminescence band at 0.95 eV, as the sample n3# used here. Since  $V_{Ga}$  is triply charged at high doping levels in n-type GaAs:Si [81, 121, 122] and the luminescence band at 1.14 eV is certainly related to the  $(Si_{Ga}V_{Ga})^{2-}$ , it can be deduced that the energy level of  $V_{Ga}^{3-}$  is at least 0.3 eV above the valence band, in agreement with theoretical calculations [81, 120]. At this point, further discussions will be made below in the case of GaAs:S.

## 6.2 Luminescence bands in n-type GaAs:S

The samples were prepared step by step in the same way as described in Section 5.2. In this Section, it is stressed that the collected spectra have been corrected by the corresponding sensitivity of the detectors in order to accurately determine the energy positions of luminescence bands (see Fig. 3.7 in Sec. 3.2).

SIMS measured the depth profile of sulfur concentration within the range of 2–4  $\mu\text{m}$  below the surface, indicating that the sulfur-depth profile has very small gradient after long-time diffusion (12 hours) at 1100 °C. The sulfur concentration near the surface is given in Table. 6.1. The computer simulations of in-diffusion profiles of sulfur state that the small gradient is valid only when the depth below the surface is smaller than 10  $\mu\text{m}$ , above which the sulfur concentration decreases rapidly to zero, implying a semi-insulating (SI) internal region of the samples (see Fig. 6.6). Since the 20 keV incident electron beam used in CL equipments can penetrate 2  $\mu\text{m}$  into GaAs material, any information achieved by CL is from the near-surface region of the samples, consistent with SIMS measurements. The concentration of boron atoms acting as acceptors, which is contributed by the encapsulant (boron oxide) during crystal growth, was also measured by SIMS and is spatially homogeneous from the surface to the internal region of the samples.

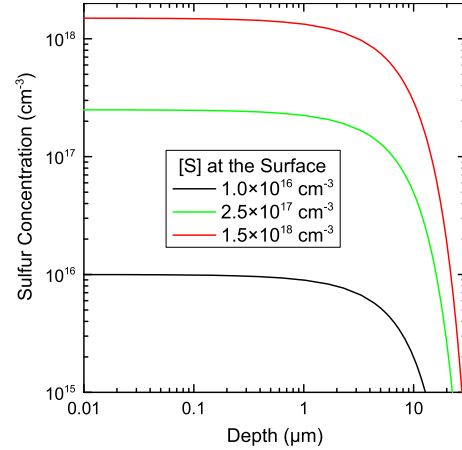


Figure 6.6: The in-diffusion profile of sulfur simulated at 1100 °C for 12 hours. The figure shows that the gradient of the in-diffusion profile near the surface is small and independent of the sulfur concentration [S] near the surface of GaAs.

Table 6.1: The free electron concentration in samples 1#, 2#, and 3# determined by Hall-effect measurements ( $\bar{n}$ ) and Raman scattering ( $n$ ). The electron resistivity ( $\rho$ ) and the carrier mobility ( $\mu$ ) determined by Hall-effect measurements. The sulfur and boron concentrations are from SIMS. Raman scattering overestimates the free-electron concentration (see text for the reason).

No.	$\bar{n}$ (cm <sup>-3</sup> )	$\rho$ ( $\Omega\cdot\text{cm}$ )	$\mu$ (cm <sup>2</sup> /Vs)	$n$ (cm <sup>-3</sup> )	[S] (cm <sup>-3</sup> )	[B] (cm <sup>-3</sup> )
1#	~SI	39	312	$\sim 2.0 \times 10^{16}$	$1.0 \times 10^{16}$	
2#	$9.0 \times 10^{14}$	2.87	2410	$\sim 3.8 \times 10^{17}$	$2.5 \times 10^{17}$	$5.0 \times 10^{17}$
3#	$5.9 \times 10^{15}$	0.37	2848	$\sim 8.5 \times 10^{17}$	$1.5 \times 10^{18}$	

Hall-effect measurements were carried out to determine the average free-carrier concentration  $\bar{n}$  over the whole region of a sample.\* The optical absorption coefficient of the laser wavelength (632.8 nm) applied in the present Raman scattering spectroscopy is  $4.0 \times 10^4 \text{ cm}^{-1}$  for GaAs, which corresponds to a laser penetration depth of 0.25  $\mu\text{m}$ . Therefore,  $n$  obtained by Raman scattering is the value near the surface and should be larger than the value by Hall-effect measurements. In Raman scattering,  $n$  is determined by calculating the ratio of the Raman intensity of the  $L^-$  mode to that of the LO mode on the basis of Eqs. (3.14) and (3.15), but not by peak position of the  $L^+$  mode. Due to the contamination during preparations, the sample surface is rough and the  $L^+$  mode is strongly damped. The measured  $L^-$  mode actually contains the contribution of the

\*The Hall-effect measurements were performed by B. Gründig, TU Bergakademie, Freiberg.

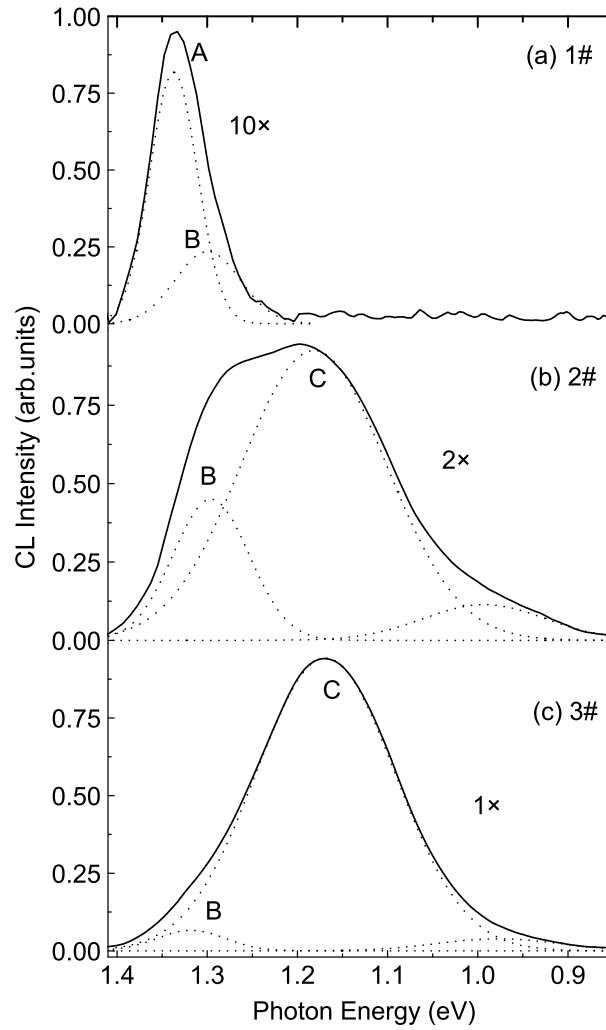


Figure 6.7: CL spectra of GaAs:S by samples 1#, 2# and 3# at 75 K. The solid lines are from experiments and the dot lines are obtained from fit. The CL intensity has been magnified by 10 times for 1#, 2 times for 2# and 1 time for 3#. The band at 0.99 eV appearing in (b) and (c) is suggested to be related to  $(S_{As}V_{Ga}S_{As})^-$  complexes, similar to the case of n-type GaAs:Si in Sec. 6.1. The spectra have been corrected by the sensitivity of the Ge detector used for the measurements.

TO mode. This results in a larger  $n$  from Raman spectra than the real one. It is the reason why  $n$  obtained by Raman scattering is abnormally larger than  $[S]$  obtained by SIMS (see Table. 6.1).

The CL spectrum from the sample with a lowest sulfur concentration (sample 1#) shows a broad luminescence band around 1.33 eV [Fig. 6.7(a), solid line]. The CL spectrum from sample 2# exhibits a band around 1.20 eV and a shoulder around 1.30 eV [Fig. 6.7(b), solid line]. The CL spectrum from sample 3# shows one band around 1.20 eV [Fig. 6.7(c), solid line]. Thus three luminescence bands can be detected in these samples. In addition to the three bands, two more bands around 1.51 eV related to the NBE emission and around 0.99 eV, probably related to  $(S_{As}V_{Ga}S_{As})^-$  complexes (see discussion in Sec. 6.1), have also been observed by CL although they will not be discussed further here. For better identifying the properties of the luminescence bands, the luminescence bands from 1.40 eV to 1.0 eV are decomposed into three subbands. One is expected to be around 1.33 eV (band A for convenience), the second one around 1.30 eV (band B), and the third one around 1.20 eV (band C). The decomposition is based on a Gaussian fit.

Boron-related defects are frequently used to explain the luminescence bands A and B [82, 112–114]. Boron occupying an arsenic lattice site may form a neutral acceptor ( $B_{As}^0$ ) or a singly charged one ( $B_{As}^-$ ). Since the energy level of  $B_{As}^0$  and  $B_{As}^-$  is expected to be respectively around 71 meV and 188 meV above the valence band maximum [114, 115], the band A can be attributed to the  $eB_{As}^-$  transition [82]. The emission of one phonon (36 meV for the LO phonon of GaAs) possibly shift the photon energy from the band A to the band B. However, the expectation on the band B cannot interpret why the CL intensity of the band A relative to the band B decreases from sample 1# to 2#, in which direction the sulfur concentration and the free-electron concentration go higher. The CL intensity of the band A relative to the band B or C is reduced probably due to the enhanced competition of the radiative recombinations resulting in the bands B and C with increasing sulfur concentration.

Since the CL intensity of the bands B and C increases from sample 1# to 2#, it is natural to turn to sulfur-related or sulfur-induced defects to be responsible for the two bands. The bands B and C may originate from the transition within molecule-like donor ( $S_{As}^+$ )-Ga vacancy complexes in GaAs treated under As-rich environment [68–71]. However, it is not clear what the charge states of the complexes are at this stage. By measuring the compensation ratio in n-type GaAs:S, Se and Te grown by chloride vapor phase epitaxy (VPE), Wolfe and Stillman found that the compensation ratio is independent of the free-electron concentration (FEC) when the FEC is below  $1 \times 10^{18} \text{ cm}^{-3}$  and thus deduced a double charge state for the Ga vacancy [116]. The doubly charged Ga vacancies were also deduced from measurements by electron-paramagnetic-resonance (EPR) [117] and electrochemical C–V profiling [118] of p-type GaAs. However, theoretical calculations [81, 119, 120] and gallium self-diffusion experiments [121] predicted a triply negative charge state within band gap. Based on earlier suggestions and the present fact that the band B is enhanced from sample 1# to 2#, but is weakened from sample 2# to 3#, while the band C is always enhanced from sample 1#, 2# to 3#, it is assumed that the band B originates from the  $(S_{As}V_{Ga})^-$  complexes formed by  $S_{As}^+$  and  $V_{Ga}^{2-}$  and the band C from the  $(S_{As}V_{Ga})^{2-}$  complexes formed by  $S_{As}^+$  and  $V_{Ga}^{3-}$ .

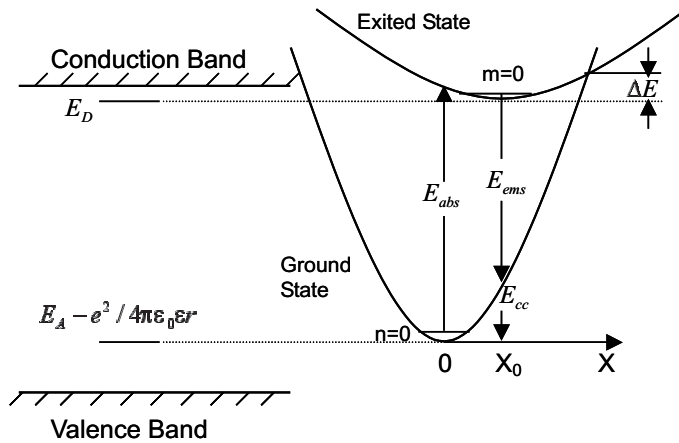
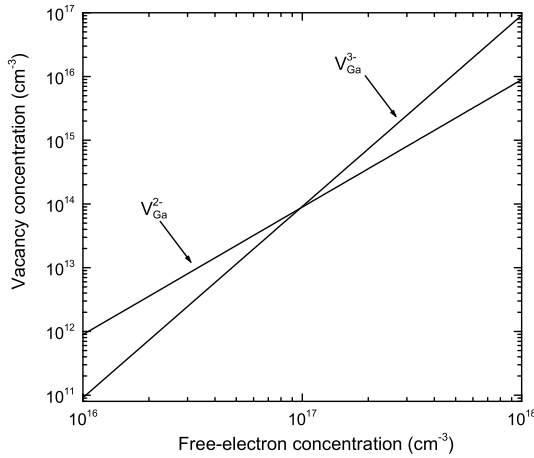


Figure 6.8: The configurational coordinate model for the transition from the excited to the ground state of a complex. The absorption energy,  $E_{abs}$  is greater than the emission energy  $E_{ems}$ ; and the difference is due to the Stokes shift.  $X$  represents the configurational coordinate.

Before confirming this assumption, two concepts must be firstly stressed. One is that a donor–vacancy complex is molecule-like so that it is the orbital hybridization of the donor and the vacancy that results in its ground and excited states. The other one is that the shorter distance between the donor and the vacancy leads to a larger separation between the ground and excited states [50]. The latter explains why the luminescence band C through the transitions within the nearest-neighbor  $(S_{As}V_{Ga})^{2-}$  or  $(Te_{As}V_{Ga})^{2-}$  complexes is positioned at a higher energy than the transitions within the second-nearest-neighbor  $(Si_{Ga}V_{Ga})^{2-}$  complexes. From the configurational coordinate model (see Fig. 6.8), the energy of an emitted photon [123, 124]

$$h\nu = E_g - E_D - (E_A - e^2/4\pi\epsilon_0\epsilon r) - E_{cc} + \frac{1}{2}h\nu_e. \quad (6.2)$$

is obtained, where  $E_g$  is the band gap,  $E_A$  and  $E_D$  are the ionization energies of an isolated  $V_{Ga}$  acceptor and a  $S_{As}^+$  donor.  $r$  is the distance between  $V_{Ga}$  and  $S_{As}^+$ .  $E_{cc}$  is the configurational coordinate shift between the final state of the optical emission and the ground state energy curve minimum. It was deduced as 0.24 eV by Williams and White for the band C of the  $(Si_{Ga}V_{Ga})$  complexes in GaAs:Si [123, 124].  $\frac{1}{2}h\nu_e$  is the vibrational energy of a phonon at excited state with zero vibrational level (i.e.  $m = 0$  in Fig. 6.8), and it is given as 11 meV [68]. Given  $E_{cc} = 0.24$  eV is the same for the  $(S_{As}V_{Ga})$  complexes with all the charge states [124], the ionization energy of  $V_{Ga}$  can be obtained as 0.52 eV for  $V_{Ga}^{3-}$  and 0.42 eV for  $V_{Ga}^{2-}$ . According to Eq. (2.11), the ratio of the concentration of  $V_{Ga}^{3-}$  to  $V_{Ga}^{2-}$  is equal to



$$\frac{C_{V_{Ga}^{3-}}}{C_{V_{Ga}^{2-}}} = \exp\left[\frac{(E_F - E_{V_{Ga}^{3-}})}{k_B T}\right], \quad (6.3)$$

The free-electron concentration  $n$  in an n-type semiconductor is expressed as

$$n = N_c \exp[(E_F - E_c)/k_B T], \quad (6.4)$$

where  $E_c$  is the conduction band minimum,  $N_c$  the effective density of states estimated to be approximately  $2.88 \times 10^{18} \text{ cm}^{-3}$  in GaAs at 1100 °C [125]. From Eqs. (6.3) and (6.4),

$$\frac{C_{V_{Ga}^{3-}}}{C_{V_{Ga}^{2-}}} = \frac{n}{N_c} \exp\left[\frac{(E_c - E_{V_{Ga}^{3-}})}{k_B T}\right] \quad (6.5)$$

is obtained. The temperature dependence of the energy gap of GaAs is [125]

$$E_g(T) = 1.519 - 5.4 \times 10^{-4} T^2 / (T + 204) \text{ eV}. \quad (6.6)$$

Eq. (6.6) results in  $E_c = 0.87$  eV above the valence band maximum at 1100 °C. Consequently, an important information is achieved that  $C_{V_{Ga}^{3-}}/C_{V_{Ga}^{2-}}$  is smaller than 1 and thus  $V_{Ga}^{2-}$  are favorable gallium vacancies when  $n$  is below a critical value of  $1.0 \times 10^{17} \text{ cm}^{-3}$ , above which  $V_{Ga}^{3-}$  are dominant gallium vacancies at 1100 °C (see Fig. 6.9). Of course, the concentration of the two kinds of vacancies increases from the low-level to the high-level doping due to Fermi-level effect. Since a  $V_{Ga}^{2-}$  is a deep-level acceptor, 0.42 eV above the valence band, the probability that an electron is thermally excited from the valence band to the  $V_{Ga}^{2-}$  state is low so that the transition from a  $V_{Ga}^{2-}$  to a  $V_{Ga}^{3-}$  state is difficult by capturing an electron from the valence band. Therefore, the character of the gallium vacancies after quenching the sample is supposed to be the same as that at 1100 °C.

Previous theoretical calculations provided the energy level of  $V_{Ga}^-$ ,  $V_{Ga}^{2-}$  and  $V_{Ga}^{3-}$  of 0.11 eV, 0.22 eV and 0.33 eV above the valence band maximum, respectively [81, 120]. The calculations by Baraff and Schlüter (0.2, 0.5 and 0.7 eV) [119] and by Xu et al. (0.28 eV, 0.44 eV and

0.65 eV) [127] as well as the experiments on p-type GaAs [117,118] supported deeper levels above the valence band, comparable to the deductions here. The discussion above suggests that the luminescence band B result from the  $(S_{As}V_{Ga})^-$  complexes formed by  $S_{As}^+$  and  $V_{Ga}^{2-}$  and the band C from the  $(S_{As}V_{Ga})^{2-}$  complexes formed by  $S_{As}^+$  and  $V_{Ga}^{3-}$ . The concentrations of  $(S_{As}V_{Ga})^-$  and  $(S_{As}V_{Ga})^{2-}$  complexes increase with the doping level. Consequently, the CL intensities of the bands B and C relative to that of the band A increase with the doping level. The variation in  $C_{V_{Ga}^{3-}}/C_{V_{Ga}^{2-}}$  and hence in the ratio of the luminescence intensity of the band B to C leads to the difference of the peak position when the two bands merge and form a single band. This is possibly the reason why the gallium vacancy-related luminescence bands are found at different energy positions from 1.10 eV to 1.30 eV by different groups.

According to the Fermi-level effect, the increasing strength in the number of  $V_{Ga}^{2-}$  is weaker than in the number of  $V_{Ga}^{3-}$  with the free-electron concentration (see Fig. 6.9). Therefore, when the doping level is high enough,  $V_{Ga}^{3-}$  dominate and enhance the compensation effect with increasing doping level, as indicated in Ref. [128].

In this section, the luminescence in the case of GaAs:S was analyzed with different doping levels. It has been suggested that both  $V_{Ga}^{2-}$  and  $V_{Ga}^{3-}$  acceptors contribute to the luminescence, depending on the doping level. The energy levels of an isolated  $V_{Ga}^{2-}$  and  $V_{Ga}^{3-}$  have been deduced to lie at 0.42 eV and 0.52 eV, respectively, above the valence band maximum. The transition within  $(S_{As}V_{Ga})^-$  complexes causes a luminescence band around 1.30 eV, while the transition within  $(S_{As}V_{Ga})^{2-}$  complexes results in the band around 1.20 eV. It is worth noting that the absolute CL intensity of a luminescence band in a CL spectra with several luminescence bands does not directly correspond to the concentration of the defects contributing to the band since the recombination probability for an electron-hole pair may be different for different recombination paths. An enhanced luminescence band may suppress other bands due to different increases in the strength of the amount of the relevant defects.



# 7 Dislocations in GaN

The effect of dislocations on the electronic and optical properties of GaN-based devices has been a controversial topic since the work by Lester et al., who showed that light emitting diodes based on GaN can work efficiently in spite of a high density of dislocations ( $10^{10} \text{ cm}^{-2}$ ) [129]. It is known that dislocations in conventional semiconductors such as GaAs, GaP, and ZnSe act as non-radiative recombination centers to reduce the luminescence intensity, leading to fatal degradation of optoelectronic devices. In principle, two different models have been applied to explain the exotic characters of GaN: (i) Dislocations in GaN do not act as recombination centers [129]. (ii) More frequently, dislocations are believed to act as recombination centers. However, the diffusion length of excess minority carriers (about  $0.25 \mu\text{m}$ ) is too short so that they cannot reach the dislocations for recombination [12, 130, 131]. It is difficult to determine whether dislocations as recombination-active centers are non-radiative or radiative ones because some point defects usually aggregate around the dislocations to make it ambiguous to distinguish experimentally who, dislocations themselves or point defects, affect the luminescence at the dislocations. Recent experiments on fresh dislocations created by micro-indentation of single GaN crystal seem to overcome this difficulty, suggesting that dislocations in GaN can be either radiative or non-radiative recombination centers, depending on the dislocation type [132]. It has been deduced that the enhanced yellow luminescence (YL) band around the dislocations actually originates from the aggregation of gallium vacancies there [133].

Although experiments have found that almost all n-type GaN samples exhibit a broad YL band around  $2.2 - 2.3 \text{ eV}$  [64, 134–138], it is still controversial whether the YL band originates from intrinsic defects [137–139] or from impurities [140–142]. The YL intensity was found to increase with the concentration of gallium vacancies. Furthermore, from theoretical calculations, it has been concluded that a gallium vacancy is energetically favorable in n-type GaN.  $V_{\text{Ga}}$ -related complexes (e.g. with impurities like oxygen) have been suggested to be the most likely sources responsible for the YL [134]. It is generally expected that two mechanisms are responsible for the YL: a radiative transition from a shallow-donor state to a deep-acceptor level [143]; or a transition from a deep-double donor level to a shallow-acceptor state [144]. In this chapter, Raman scattering and cathodoluminescence microscopy are used to obtain information about the structure of GaN associated with in-grown dislocations or dislocations freshly introduced by Vickers micro-indentations. While the in-grown dislocations originate from the crystal growth at high temperatures, the dislocations at the indentations were generated at rather low temperatures. It is expected that both types of dislocations exhibit a different character with respect to the decoration with a point-defect atmosphere.

## 7.1 Experiments

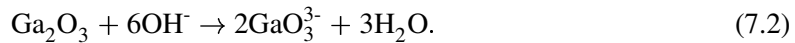
Similar to previous work [145], unintentionally doped n-type GaN single crystals with a wurtzite structure and (0001)-orientation were grown under high-hydrostatic pressure of nitrogen (15 to 20 kbar) from liquid gallium at a temperature of  $1600 \text{ }^\circ\text{C}$ . The free-electron concentration amounts to about  $3.0 \times 10^{19} \text{ cm}^{-3}$ . Two groups of different samples without or with indentations were prepared. The indentations on the N-polar (000 $\bar{1}$ ) surface were performed at 250 to  $350 \text{ }^\circ\text{C}$  under

a 2 N load using a Vickers diamond indenter. The dwell time ranged from 1 to 20 min. After deformation, the samples were cooled down slowly to room temperature. The local deformation by Vickers indentation produces a high density of dislocations. In order to visualize dislocations, the samples were etched for about 2 min in a molten KOH–NaOH eutectic at temperatures of 200 °C, at which Ga-polar surfaces are resistant to the molten KOH–NaOH etchant whereas N-polar surfaces are chemically active [146]. Afterwards, the samples were investigated by Raman and CL microscopy.

Similar to GaAs, the etching process in GaN is based on the oxidation and dissolution through two steps [147]. In the first step, GaN is oxidized,



the oxide ( $\text{Ga}_2\text{O}_3$ ) is chemically dissolved in the second step,



Reactions (7.1) and (7.2) indicate that the kinetics of surface reactions is controlled by  $(\text{OH})^-$  ions and holes. The hydrodynamics conditions are important for the dissolution rate and the morphology. In order to reveal crystallographic defects like dislocations, the supplying rate of  $(\text{OH})^-$  ions to the GaN-solution interface must be faster than the rate of the reaction of GaN-surface bonds with holes. In this way, reaction (7.2) is faster than reaction (7.1). As a result, the  $\text{Ga}_2\text{O}_3$  oxide produced by reaction (7.1) can be removed in time from the GaN surface through reaction (7.2) not to hinder the appearance of the defects.

## 7.2 Results and discussion

The characteristic rosette around the Vickers indentation formed by dislocation etch pits is shown in Fig. 7.1(a). In addition to the dislocation rosette, radial cracks are to be seen as dark lines. Raman measurements were carried out at several different positions in the indentation, as indicated in Fig. 7.1(a).

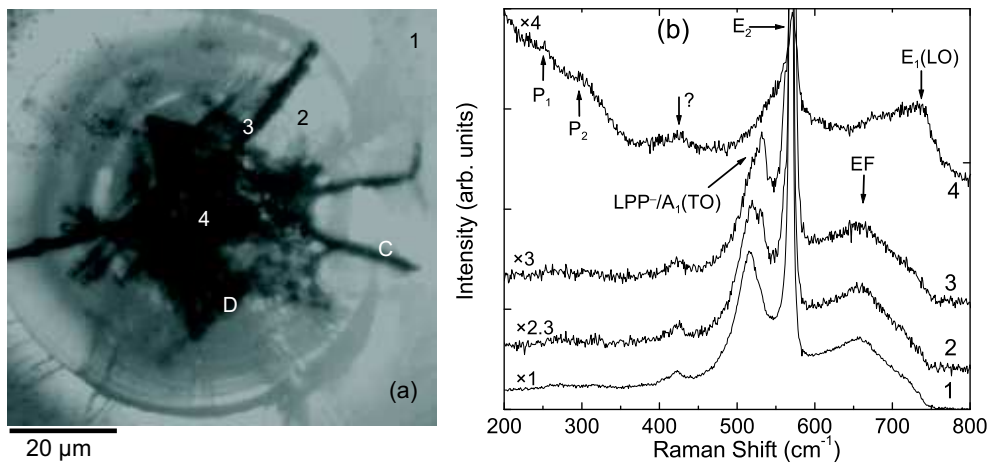


*Figure 7.1:* (a) Image of the etched region around an indentation in GaN taken by optical microscopy. D indicates the dislocation rosette, C crack. (b) Raman spectra acquired at the positions 1–4 marked in (a). The labels of the peaks are explained in the text.

As described in Sec. 3.1.3, GaN with a wurtzite structure belongs to the  $C_{6v}$  space group. Group theory predicts eight  $\mathbf{q} = \mathbf{0}$  phonon modes, i. e. two  $E_2$ , one  $A_1(\text{TO})$ , one  $A_1(\text{LO})$ , one  $E_1(\text{TO})$ ,

one  $E_1(\text{LO})$ , as well as two  $B_1$  modes [see Tab. 3.1(b)]. The  $E_2$  modes are Raman active, the  $A_1$  and  $E_1$  modes are both Raman and infrared active, and the two  $B_1$  modes are silent.

The Raman spectra obtained in the undeformed matrix are consistent with the hexagonal structure of GaN because of the existence of the  $E_2$  peak at  $567\text{ cm}^{-1}$  [Fig. 7.1(b), curve 1]. The line position in a stress-free GaN sample is expected at  $566.2\text{ cm}^{-1}$  [148]. The detailed examination of the  $A_1(\text{TO})$ -like peak of curve 1 reveals that it is actually at  $518\text{ cm}^{-1}$ ,  $15\text{ cm}^{-1}$  below the  $A_1(\text{TO})$  peak expected in a perfect GaN crystal. Previous results showed that the peak around  $518\text{ cm}^{-1}$  reflects the low-frequency branch of the two  $A_1(\text{LO})$  phonon–plasmon modes ( $\text{LPP}^-$ ), which is a function of the free-electron concentration as shown in Fig. 3.2(b).  $\text{LPP}^-$  here corresponds to the  $A_1(L^-)$  in Fig. 3.2(b). The broad  $A_1(\text{TO})$ -like peak in Fig. 7.1(b) may thus indicate the degeneration of  $\text{LPP}^-$  and  $A_1(\text{TO})$  peaks. As a matter of fact, the degenerated  $\text{LPP}^-/A_1(\text{TO})$  peak is split into the two subpeaks,  $\text{LPP}^-$  and  $A_1(\text{TO})$ , near the indentation [Fig. 7.1(b), curve 2]. The approximate attribution of  $518\text{ cm}^{-1}$  to  $\text{LPP}^-$  gives a free-electron concentration of  $9.5 \times 10^{19}\text{ cm}^{-3}$ . It is twice larger than the actual value ( $3.0 \times 10^{19}\text{ cm}^{-3}$ ) in the matrix, as the peak position at  $518\text{ cm}^{-1}$  is determined by both  $\text{LPP}^-$  and  $A_1(\text{TO})$ , not only by  $\text{LPP}^-$ .

A wide band around  $650\text{ cm}^{-1}$  (labeled EF for convenience) is present in the high-energy part of the curves 1–3 of Fig. 7.1(b). The EF peak has been proven to have a  $A_1$  character [149]. It is known from doped GaN with a high free-electron concentration [139], consistent with the appearance of the  $\text{LPP}^-$  peak. Actually, the intensity of the EF peak increases with the free-electron concentration [139].

Fig. 7.1(b) shows further that the  $\text{LPP}^-/A_1(\text{TO})$  peak shifts up to a higher position from the matrix to the indentation center [from point 1 to 4 marked in Fig. 7.1(a)], until it is finally a shoulder in the  $E_2$  peak [see Fig. 7.1(b), curve 4]. There are two possibilities for the blue shift. One is due to an increase in the free-electron concentration, the other one due to an enhanced compressive stress. However, a reduction in the free-electron concentration from the matrix to the indentation center follows from the weakening of the EF peak at the indentation center. Thus, an increase in the compressive stress should be responsible for the blue shift of the  $\text{LPP}^-/A_1(\text{TO})$  peak.

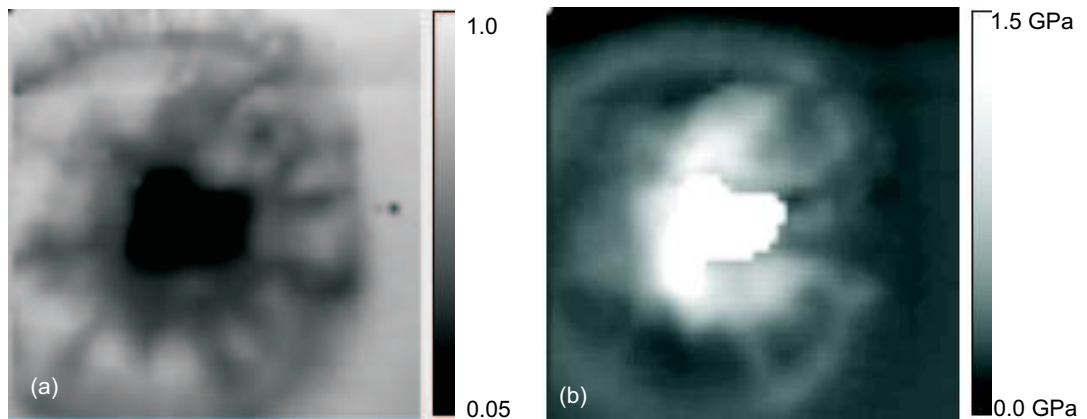


*Figure 7.2:* (a) Spatial distribution of the intensity of the  $E_2$  peak at an indentation. The grey scale indicates the intensity which has been set to 1 in the matrix. At the indentation center, the intensity of the  $E_2$  peak amount to 5 % of the intensity in the matrix. (b) Calculated spatial distribution of the residual compressive stress. The maximum stress of 1.5 GPa is reached at the indentation center.

Compared to that in the matrix, the Raman peaks at the indentation center are found to be rather broad while their intensities are very low, especially that of the  $E_2$  phonon mode [Fig. 7.1(b), curve 4]. This suggests a poor hexagonal crystalline order after deformation. In spite of the structural

changes at the indentation center, there are still Raman peaks like  $E_1$  (LO) around  $740\text{cm}^{-1}$ , which is superimposed in the matrix by the wide EF band, suggesting that the indentation region does keep some crystalline order.

The character of the peak at  $420\text{cm}^{-1}$ , which is always present from the matrix to the indentation center, could not be identified. In the deformed region, the intensity of Raman shift below  $350\text{cm}^{-1}$  is lifted abnormally due to noise caused by surface roughness. Further low-intensity peaks, marked as  $P_1$  at  $250\text{cm}^{-1}$  and  $P_2$  at  $300\text{cm}^{-1}$ , appear near the indentation center [Fig. 7.1(b), curve 4]. Previous experimental and theoretical work have elucidated that GaN with a wurtzite structure at ambient pressure transforms to rocksalt structure under the pressure of 37 GPa [150]. In combination of these studies with the present observations, it is deduced that the weak  $P_1$  and  $P_2$  peaks might be related to rocksalt structure. However, stronger proofs are required to support this conclusion.

The mapping of the spatial distribution of the Raman intensity of the  $E_2$  peak in Fig. 7.2(a) shows that the intensity decreases significantly from the matrix to the indentation center, while a residual compressive stress [Fig. 7.2(b)] is found to concentrate mainly in the indentation region. This residual stress is evaluated by calculating the peak position of the  $E_2$  mode in relation to that of a perfect GaN crystal. A blue shift of the  $E_2$  mode is assumed to be caused by a compressive stress, and a red shift by a tensile stress. A conversion factor of  $3.6\text{cm}^{-1}/\text{GPa}$  for the  $E_2$  Raman mode [148] results in a maximum compressive stress of 1.5 GPa at the indentation center.

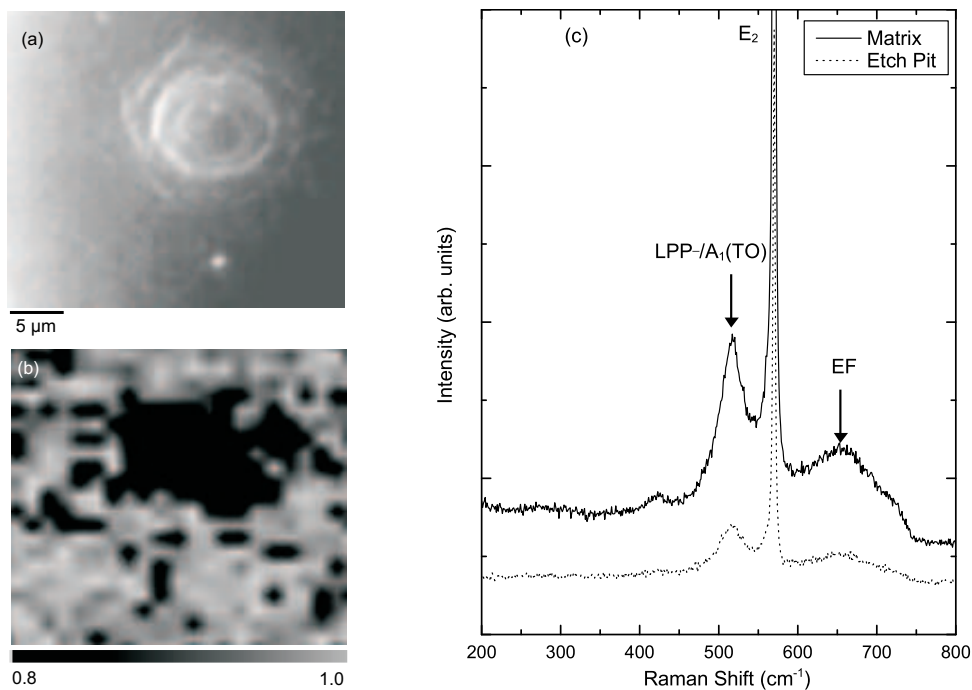
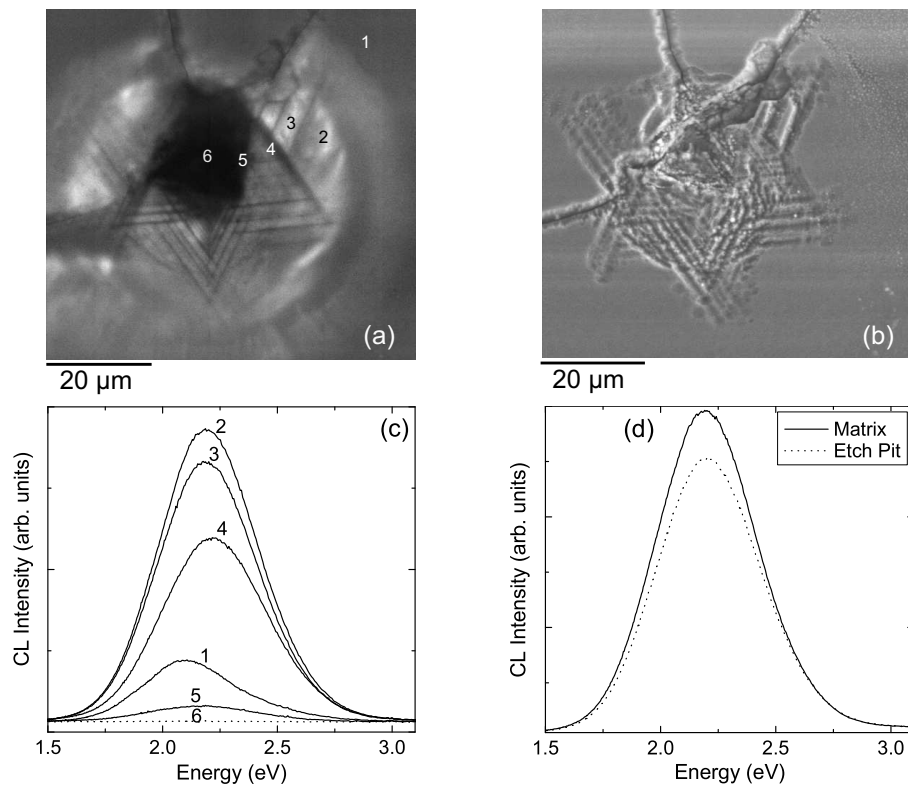


Figure 7.3: (a) Etch pit of an in-grown dislocations. (b) Spatial distribution of the  $E_2$  Raman peak in the same region. The relative intensity decreases from 1.0 to 0.8 from the matrix to the etch pit. (c) Raman spectra acquired in the matrix and at the etch pit of an in-grown dislocation.

The Raman spectra obtained at the indentation with a high density of fresh dislocations are compared to those obtained at individual in-grown dislocations, which are presumably formed at very high temperatures during growth of the GaN crystal. After etching, in-grown dislocations appear as etch pits with a diameter of about  $15\ \mu\text{m}$  [Fig. 7.3(a)]. The pits formed at in-grown dislocations are distinctly larger than those formed at the dislocations in the indentation rosettes. The remarkable difference in the size of the etch pits has been interpreted as the result of decoration

of in-grown dislocations with point defects [145]. A similar effect is also known for other III–V semiconductors.

The special etching by molten KOH–NaOH eutectic results in the formation of point-top, stepped circular etch pits. A typical example given in Fig. 7.3(a) shows a centra-symmetric etch pit to indicate that the dislocation is perpendicular to the N-polar (000 $\bar{1}$ ) surface. It is also found that some etch pits are non-symmetrical as the dislocations are inclined to the surface. Raman spectra measured at the etch pit and in the matrix are shown in Fig. 7.3(c). The same Raman peaks as in the matrix are found near in-grown dislocations. However, their intensity is slightly reduced. The distribution of the  $E_2$  intensity around an in-grown dislocation is given in Fig. 7.3(b). The reduction in the Raman intensity of the  $E_2$  mode near the dislocation to about 80 % of the intensity in the matrix may be attributed to the structural disorder induced by the dislocation. The reduction in the intensities of the EF and the LPP /  $A_1$ (TO) peaks is due to a lower-carrier concentration in the surrounding of the dislocation. The extension of the reduced carrier concentration is consistent with the diameter of the etch pit.



*Figure 7.4:* (a) Panchromatic cathodoluminescence (CL) image of an indentation. The same area is shown in the secondary-electron (SE) image in (b). CL spectra obtained at the positions 1–6 indicated in (a) are shown in (c). (d) CL spectra measured at an in-grown dislocation (etch pit) and in the GaN matrix.

As a second step, investigations by means of CL microscopy were carried out in order to investigate the optical properties of GaN near deformation-induced and in-grown dislocations, respectively. Panchromatic CL and secondary electron (SE) images of the indentation region are shown in Figs. 7.4(a) and (b). Small dislocation etch pits are arranged in a rosette-like pattern in the SE picture. The alignment of the dislocations in rosette slip lines can be recognized in the CL image in a one-to-one correspondence to the SE picture. However, no individual dislocations can be resolved in panchromatic cathodoluminescence images since their CL contrast is rather weak. The indentation center appears dark. The dislocation rosette itself is surrounded by bright regions

of high CL intensity.

CL spectra were measured at 4 K at a few typical positions in the indentation [Fig. 7.4(c)]. The luminescence band at 360 nm due to the near-band-edge emission cannot be detected due to the limitation of the CCD detector used, by which the effective wavelength detected ranges from 400 to 1100 nm. In all the cases, a broad luminescence band around 550 nm, which is known as the YL band, is acquired. The YL band has been attributed to intrinsic defects [137–139], to impurities such as oxygen or carbon [140–142], or to complexes formed by intrinsic point defects and impurities [151]. Recent positron annihilation in correlation to photoluminescence measurements have made clear that these point defects must be vacancies, most likely  $V_{\text{Ga}}$  acting as acceptors [152]. Isolated Ga vacancies in GaN are unstable at the temperature below 300 °C, so it has been concluded that they are part of complexes with impurities [153], similar to the case of  $V_{\text{Ga}}$  in GaAs.

Combining the results of Raman and CL microscopy obtained near the indentation site, it is reasonable to assume that the YL band originates from Ga vacancies which are generated as a result of the plastic deformation. Vacancies in the vicinity of the indentation are formed as a result of dislocation motion and interaction. When the indentation experiments were carried out at elevated temperatures (250 to 350 °C), a very effective process of vacancy supply is the jog dragging mechanism, which is able to provide a high density of vacancies during plastic deformation [154]. It is likely that the deformation-induced vacancies form stable complexes with impurities such as oxygen during the slow cooling to room temperature. The concentration of residual impurities in the GaN samples investigated is high enough to ensure the formation of a large number of such complexes near the indentation. The fact that the free-electron concentration decreases from the matrix to the indentation center is in agreement with the increase in the density of compensating acceptor-like complexes.

The YL intensity in the matrix [Fig. 7.4(c), curve 1] is not zero due to vacancies or vacancy-related complexes formed during crystal growth. The intensity strongly increases in the surrounding of the indentations. The dislocations in the rosette act as non-radiative recombination centers, and thus the measured YL intensity there (curve 4) is smaller than the ones at its surroundings (curves 2 and 3). At the indentation center, a high density of dislocations and other possible non-radiative recombination centers exist to passivate the radiative recombination; as a consequence, the intensity of the YL band is strongly reduced (curves 5 and 6).

It is obvious from Fig. 7.4(a) that the YL intensity and thus the defects are inhomogeneously distributed. Fig. 7.4(c) exhibits furthermore a blue shift in the position of the YL band in the indentation region (curve 5) compared to that in the matrix (curve 1). The shift can be related to the increase in the residual compressive stress near the indentation and to the reduction in the free-carrier concentration (see Sec. 3.2.2), as determined by Raman scattering. If a stress coefficient of 36 meV/GPa is assumed [64], the stress in the indentation region can be calculated as 4 GPa. This is in reasonable agreement with the stress value of 1.5 GPa obtained from Raman scattering, since the variation in the carrier concentration is not considered here.

The YL intensity at the center of the etch pit formed at an in-grown dislocation amounts to about 80 % of the intensity in the matrix [Fig. 7.4(d)]. This can be understood as the balance of non-radiative recombination at the dislocation line and the radiative recombination of vacancy–impurity complexes decorating the dislocation.

In summary, structural, electrical and optical properties of GaN near deformation-induced and in-grown dislocations by combination of Raman scattering and cathodoluminescence microscopy have been presented. Fresh dislocations were introduced by indentations. Such high-pressure indentations introduce structural disorder and a high density of dislocations. The dislocation motion and interaction generates a high density of intrinsic point defects. These point defects are most probably gallium vacancies which form stable complexes with residual impurities like oxygen

donors during cooling after the indentation. The YL band at 2.2 eV is probably related to the  $V_{\text{Ga}}$ -related complexes. Its intensity is determined by the competition between radiative recombination at the vacancy complexes and non-radiative recombination at dislocations. The results from cathodoluminescence measurements are in agreement with the decrease in the free-electron concentration and the increase in the compressive stress at the indentation center as deduced from Raman microscopy. Similar to the region of the dislocation rosette at indentations, a decrease in the free-electron concentration has been found at individual in-grown dislocations. Correspondingly, characteristic changes in the Raman spectra are observed in the etch pit region.



## 8 Summary and Conclusion

The effect of point defects and dislocations on the electrical and optical properties of III–V semiconductors (GaAs and GaN) has been investigated theoretically and experimentally by concentrating on the interactions between point defects and dislocations. A few summaries and conclusions are given in the following.

Raman scattering has been applied to determine the free-carrier concentration from the matrix to the dislocation by calculating the ratio of Raman intensity of LO phonon to that of the low-frequency branch ( $L^-$ ) of the two LO phonon–plasmon coupled modes or by detecting the position of the high-frequency branch ( $L^+$ ) in Raman spectra. Raman scattering has further been carried out to reveal the spatial distribution of the free-carrier concentration and stress in the GaN single crystal with and without indentation. The residual stress from the matrix to the dislocation after indentation of the GaN single crystal determined by Raman scattering is comparable to the evaluation through the cathodoluminescence (CL) measurements.

A so-called diffusion–drift–aggregation (DDA) model has been developed to describe the kinetic processes of point defects due to their interactions with dislocations. Computer simulations based on the DDA model have been carried out to reveal that the conventional “Cottrell” atmosphere cannot correctly describe the aggregation of point defects at the dislocation in all cases. In spite of different diffusion mechanisms, the whole character of the dislocations in n-type GaAs:Si and GaAs:S are similar: the interactions of point defects with dislocations induce dopants, gallium vacancies, arsenic interstitials, and donor–gallium vacancy complexes to diffuse towards and to aggregate around the dislocations. The aggregation magnitude of point defects around the dislocation in GaAs depends on temperature, arsenic pressure, and the doping level. The higher the temperature, arsenic pressure, or the doping level is, the stronger the aggregation of point defects around the dislocations is. In addition to an important influence on the aggregation magnitude and extension of the point-defect atmosphere around the dislocations, the arsenic precipitation at the dislocation is found to decisively extend the increasing region of the resultant free-electron concentration around the dislocation. Computer simulations based on the DDA model reveal that an arsenic precipitate is kinetically preferred to be formed at the dislocation. Molecular dynamics simulations with a Tersoff-type interaction potential have been carried out to elucidate that it is energetically favorable for arsenic precipitates to be formed at the dislocations.

Dislocations act as non-radiative recombination centers to passivate the luminescence in GaAs and GaN. Whether the dislocations appear dark or bright in the CL images relies on the concentration of point defects aggregated there, the density of excess minority carriers, and the competition between radiative recombination and non-radiative recombination channels at the dislocations. By eliminating the passivation effect of dislocations on the luminescence, the spatial variation in the defect concentration from the matrix to the dislocation has been determined from CL measurements. By considering the detailed atomic diffusion mechanism, it is explained why the concentrations of the  $\text{Si}_{\text{Ga}}^+$  ( $\text{S}_{\text{As}}^+$ ) donors, gallium vacancies ( $\text{V}_{\text{Ga}}^{3-}$ ), and donor-vacancy complexes such as  $(\text{Si}_{\text{Ga}}\text{V}_{\text{Ga}})^{2-}$  and  $(\text{S}_{\text{As}}\text{V}_{\text{Ga}})^{2-}$ , as well as the resultant free-electron concentration increase from the matrix to the dislocation in n-type GaAs:Si and GaAs:S. The formation of a large number of interstitial dislocation loops may largely consume the interstitial arsenic. In this case, no arsenic precipitate can be formed and the free-electron concentration near the dislocation may be lower

than in the matrix due to the pronounced production of gallium vacancies acting as acceptors, accompanying the formation of interstitial dislocation loops. Therefore, the increase or decrease in the free-electron concentration from the matrix to the dislocation cannot be simply attributed to a dilution of the concentration of acceptors or donors occupying the arsenic lattice sites around the dislocation.

Positron annihilations (positron lifetime and Doppler broadening) in GaAs have been carried out to distinguish point defects and their chemical environments. By correlating positron annihilation with CL, the defects responsible for the 0.95 eV luminescence band have been identified. In n-type GaAs:Si and GaAs:S, depending on the doping level, there are three possible kinds of gallium vacancy-related complexes. A doubly or triply charged gallium vacancy and one donor form a complex such as  $(S_{As}V_{Ga})^-$  or  $(S_{As}V_{Ga})^{2-}$  in GaAs:S, and  $(Si_{Ga}V_{Ga})^{2-}$  in GaAs:Si. A triply charged gallium vacancy and two donors form a complex such as  $(S_{As}V_{Ga}S_{As})^-$  in GaAs:S and  $(Si_{Ga}V_{Ga}Si_{Ga})^-$  in GaAs:Si. These complexes result in the luminescence bands around 1.30 eV [ $(S_{As}V_{Ga})^-$ ], 1.20 eV [ $(Si_{Ga}V_{Ga})^{2-}$  or  $(S_{As}V_{Ga})^{2-}$ ], and around 0.95 eV [ $(Si_{Ga}V_{Ga}Si_{Ga})^-$  or  $(S_{As}V_{Ga}S_{As})^-$ ], respectively. The ground states of the three kinds of complexes lie at about 0.2 eV, 0.3 eV, and 0.5 eV, respectively, above the valence band maximum, while their excited states are shallow levels (about 20 meV) below the conduction band minimum. Using the configurational coordinate model, the energy levels of an isolated  $V_{Ga}^{2-}$  and  $V_{Ga}^{3-}$  are supposed to lie at 0.42 eV and 0.52 eV above the valence band maximum. The formation energy of charged point defects, which is dependent of the Fermi level, determines their concentration at a given doping level. The CL and positron-annihilation investigations of n-type GaAs:Si and GaAs:S suggest that the formation energy of a  $(Si_{Ga}V_{Ga}Si_{Ga})^-$ ,  $(S_{As}V_{Ga}S_{As})^-$ , or a  $(S_{As}V_{Ga})^-$  complex be lower than that of a  $(Si_{Ga}V_{Ga})^{2-}$  or a  $(S_{As}V_{Ga})^{2-}$  complex at a low doping level. It is vice versa at a high doping level. Due to the Fermi-level effect, the concentration of the gallium vacancy-related complexes with higher charge states increases at a higher rate with the doping level than that of complexes with lower charge states. In the same way, the compensation at the low doping level is low due to the formation of singly charged gallium vacancy-related complexes. In contrast, the compensation is enhanced at the high doping level by forming gallium vacancy-related complexes with higher charge states. The enhanced compensation from the low to the high doping level is one of the reasons why the free-carrier concentration in semiconductors is actually limited within some range and cannot always increase with the dopant concentration.

A high density of intrinsic point defects is formed during dislocation generation, motion, and interaction during plastic deformation by indentation of GaN. These point defects are most probably gallium vacancies which form stable complexes with residual impurities such as oxygen donors during cooling after the indentation on GaN. The gallium vacancy-related complexes have been suggested to be responsible for the yellow luminescence (YL) band at 2.2 eV in GaN. The intensity of the YL band is determined by the competition between radiative recombination at the gallium vacancy-related complexes and non-radiative recombination at dislocations. Cathodoluminescence measurements indicate a decrease in the free-electron concentration and an increase in the compressive stress at the dislocation rosette at indentations, as deduced from Raman scattering. The aggregation of gallium vacancy-related complexes acting as acceptors at the dislocation results in a decrease in the free-electron concentration at individual in-grown dislocations, similar to that in the dislocation-rosette region at indentations.

# Bibliography

- [1] P. J. McNally, P. A. F. Herbert, T. Tuomi, K. Kariahti, and J. A. Higgins, *J. Appl. Phys.* **79**, 8294 (1996).
- [2] J. P. Van der Ziel, R. D. Dupuis, R. A. Logan, and C. J. Pinzone, *Appl. Phys. Lett.* **51**, 89 (1987).
- [3] S. Miyazawa, T. Honda, Y. Ishii, and S. Ishida, *Appl. Phys. Lett.* **44**, 410, (1984).
- [4] R. A. Brown and J. S. Williams, *Phys. Rev. B* **55**, 12852 (1997).
- [5] M. G. Tabache, E. D. Bourret, and A. G. Elliot, *Appl. Phys. Lett.* **49**, 289 (1986)
- [6] C. Hannig, G. Schwichtenberg, E. Buhrig, and G. Gärtner, *Mater. Sci. Eng. B* **66**, 97 (1999)
- [7] Y. Seki, H. Watanabe, and J. Matsui, *J. Appl. Phys.* **49**, 822 (1978).
- [8] H. Alexander, H. Teichler, in *Handbook of Semiconductor Technology*, Edited by K. A. Jackson, W. Schröter, (Weinheim: Wiley-VCH, 2000), Vol. 1, pp. 291–376.
- [9] W. Walukiewicz, *Phys. Rev. B* **39**, 8776 (1989).
- [10] R. Jones, *Mater. Sci. Eng. B* **71**, 24 (2000).
- [11] C. Kieselowski-Kemmerich, *Phys. Status Solidi B* **161**, 11 (1990).
- [12] S. J. Rosner, E. C. Car, M. J. Ludowise, G. Girolami, and H. I. Erikson, *Appl. Phys. Lett.* **70**, 420 (1997).
- [13] S. Nakamura, *Science*, **281**, 956 (1998).
- [14] H. Lei, H. S. Leipner, N. Engler, and J. Schreiber, *J. Phys: Cond. Mat.* **14**, 7963 (2002).
- [15] H. Lei, H. S. Leipner, and N. Engler, *Appl. Phys. Lett.* **82**, 1218 (2003).
- [16] H. J. Queisser and E. E. Haller, *Science*, **281**, 945 (1998).
- [17] P. Sitch, R. Jones, S. Öberg, and M. I. Heggie, *Phys. Rev. B* **50**, 17717 (1994).
- [18] J. Bennetto, R. W. Nunes, and D. Vanderbilt, *Phys. Rev. Lett.* **79**, 245 (1997).
- [19] J. F. Justo, R. W. Nunes, and L. V. C. Assali, *J. Phys.: Condens. Matter.* **14**, 12749 (2002).
- [20] I. Yonenaga and K. Sumino, *J. Appl. Phys.* **65**, 85 (1989).
- [21] D. J. Chadi and K. J. Change, *Phys. Rev. Lett.* **60**, 2187 (1988).
- [22] J. Elsner, R. Jones, P. K. Stich, V. D. Porezag, M. Elstner, Th. Frauenheim, M. I. Heggie, S. Öberg, and P. R. Briddon, *Phys. Rev. Lett.* **79**, 3672 (1997).
- [23] A. F. Wright and J. Furthmuller, *Appl. Phys. Lett.* **72**, 3467 (1998).
- [24] A. F. Wright and U. Grossner, *Appl. Phys. Lett.* **73**, 2751 (1998).
- [25] S. M. Lee, M. A. Belkhir, X. Y. Zhu, Y. H. Lee, Y. G. Hwang, and T. Frauenheim, *Phys. Rev. B* **61**, 16 033 (2000).

- [26] J. Elsner, R. Jones, M. I. Heggie, P. K. Stich, Th. Frauenheim, S. Öberg, and P. R. Briddon, *Phys. Rev. B* **58**, 12571 (1998).
- [27] J. A. Van Vechten, *Phys. Rev. B* **17**, 3197 (1978).
- [28] R. Bullough and R. C. Newman, in *Progress in Semiconductors*, edited by A. F. Gibson and R. E. Burgess (Heywood, London, 1964), Vol.8, pp. 100.
- [29] H.-M. You, U. Gösele, and T. Y. Tan, *J. Appl. Phys.* **74**, 2461 (1993); *ibid*, **74**, 7207 (1993).
- [30] C. M. Wolfe, N. Holonyak, and G. E. Stillman, in *Physical Properties of Semiconductors* (Prentice Hall, Englewood Cliffs, NJ, 1989), pp. 128-130.
- [31] C.-H. Chen, U. Gösele, and T. Y. Tan, *J. Appl. Phys.* **86**, 5376 (1999).
- [32] T. Y. Tan, U. Gösele, and S. Yu, *Crit. Rev. Sol. State Mater. Sci.* **17**, 47 (1991).
- [33] P. M. Petroff and L. C. Kimerling, *Appl. Phys. Lett.* **29**, 461 (1976).
- [34] B. P. R. Marioton, T. Y. Tan, and U. Gösele, *Appl. Phys. Lett.* **54**, 849 (1989).
- [35] T. Y. Tan, H.-M. You, and U. M. Gösele, *Appl. Phys. A.* **56**, 249 (1993).
- [36] J. E. Northrup and S. B. Zhang, *Phys. Rev. B* **47**, 6791 (1993).
- [37] W. Jüngling, P. Pichler, S. Selberherr, E. Guerrero, and H. W. Pötzl, *IEEE Trans. Electron Devices* **ED-32**, 156 (1985).
- [38] A. H. Cottrell, *Dislocation and plastic flow in crystals*, (Oxford University Press, London, 1953).
- [39] T. R. Waite, *Phys. Rev.* **107**, 463 (1957).
- [40] S. Yu, U. M. Gösele, and T. Y. Tan, *J. Appl. Phys.* **66**, 2952 (1989).
- [41] B.-T. Lee, E. D. Bourret, R. Gronsky, and I.-S. Park, *J. App. Phys.* **65**, 1030 (1989).
- [42] R. Tuck, *Diffusion in III-V Compounds*, (Stevenage, Peregrims, 1988).
- [43] H. S. Leipner, Habilitation, Martin-Luther-Universität Halle-Wittenberg (2001).
- [44] K. Sonnenberg, *IFF-Bulletin* **51**, 14 (1997).
- [45] D. Turnbull, *Solid State Physics* (Academic Press Inc., New York, 1956), Vol. 3, pp. .225-306.
- [46] M. Lannoo, J. Bourgoin, *Point defect in semiconductors I*, (Springer-Verlag, Berlin, 1983), pp. 211.
- [47] M. Uematsu, P. Werner, M. Schultz, T. Y. Tan, and U. Gösele, *Appl. Phys. Lett.* **67**, 2863 (1995).
- [48] N. Engler, Phd thesis, Halle University, 2002.
- [49] H. Kuzmany, *Solid-State Spectroscopy: An Introduction*, (Springer-Verlag, Berlin, Heidelberg, 1998).
- [50] P. Y. Yu and M. Cardona, *Fundamental s of Semiconductors*, (Springer-Verlag, Berlin, Heidelberg, 1996).
- [51] H. Siegle, G. Kaczmarczyk, L. Filippidis, A. Hoffman, and C. Thomsen, *Phys. Rev. B* **55**, 7000 (1997).
- [52] F. Cerdeira, C. J. Buchenauer, F. H. Pollak, and M. Cardona, *Phys. Rev. B* **5**, 580 (1972).
- [53] D. Olego and M. Cardona, *Phys. Rev. B* **24**, 7217 (1981).
- [54] A. Mooradian and G. B. Wright, *Phys. Rev. Lett.* **22**, 999 (1966).

- 
- [55] P. D. Wang, M. A. Foad, C. M. Sotomayor-Torres, S. Thoms, M. Watt, R. Cheung, C. D. W. Wilkinson, and S. P. Beaumont, *J. Appl. Phys.* **71**, 3754 (1992).
- [56] B. G. Yacobi and D. B. Holt, *Cathodoluminescence Microscopy of Inorganic Solids*, (Plenum, New York and London), 1990, pp. 123.
- [57] S. Hildebrandt, J. Schreiber, W. Hergert, H. Uniewski, and H. S. Leipner, *Scanning Microsc.* **12**, 535 (1998).
- [58] T. Suzuki and Y. Matsumodo, *Appl. Phys. Lett.* **26**, 431 (1975).
- [59] W. A. Brantley, O. G. Lorimor, and P. D. Dapkup, *J. Appl. Phys.* **46**, 2629, 1975.
- [60] M. Lax, *J. Appl. Phys.* **49**, 2796 (1978).
- [61] H. Kressel, F. Z. Hawrylo, M. S. Abrahams and C. J. Buiocchi, *J. Appl. Phys.* **39**, 5139 (1968).
- [62] H. Kressel, H. Nelson, S. H. McFarlane, M. S. Abrahams, P. Le Fur, and C. J. Buiocchi, *J. Appl. Phys.* **40**, 3587 (1969).
- [63] P. Perlin, I. Gorczyca, N. E. Christansen, I. Grzegory, H. Teisseyre, and T. Suski, *Phys. Rev. B* **45**, 13307 (1992).
- [64] T. Suski, P. Perlin, H. Teisseyre, M. Leszczynsky, I. Grzegory, J. Jun, M. Bockowski, S. Porowski, and T. D. Moustakas, *Appl. Phys. Lett.* **67**, 2188 (1995).
- [65] B. E. Sernelius, *Phys. Rev. B* **33**, 8582 (1986).
- [66] F. Betram, S. Srinivasan, F. A. Ponce, T. Riemann, J. Christen, and R. J. Molnar, *Appl. Phys. Lett.* **78**, 1222 (2001).
- [67] O. Paetzold, K. Sonnenberg, and G. Irmer, *Mater. Sci. Eng. B.* **44**, 217 (1997).
- [68] E. W. Williams, *Phys. Rev.* **168**, 922 (1968).
- [69] M. Capizzi, V. Emiliani, A. Frova, and F. Sarto, *Phys. Rev. B* **47**, 4301 (1993);
- [70] T. Sauncy, C. P. Palsule, M. Holtz, and S. Gangopadhyay, *Phys. Rev. B* **53**, 1900 (1996).
- [71] N. H. Ky and F. K. Reinhart, *J. Appl. Phys.* **83**, 718 (1998).
- [72] P. D. Augustus and D. J. Stirland, *J. Microsc.* **118**, 111 (1980).
- [73] C. Frigeri and J. L. Weyher, *J. Appl. Phys.* **65**, 4646 (1989).
- [74] A. G. Elliot, C. L. Wei and D. A. Wanderwater, *J. Cryst. Growth* **85**, 59 (1987).
- [75] C. A. Warwick and G. T. Brown, *Appl. Phys. Lett.* **46**, 574 (1985).
- [76] G. Abstreiter, M. Cardona and A. Pinczuk, in *Light Scattering in Solids IV*, edited by M. Cardona and G. Guentherodt (Springer, Berlin, 1984), pp. 5.
- [77] K. Wan and J. F. Young, *Phys. Rev. B* **41**, 10772 (1990).
- [78] M. E. Pistol, M. Gerling, D. Hessman, and L. Samuelson, *Phys. Rev. B* **45**, 3628 (1992).
- [79] K. Fujii, Y. Okada, and F. Osito, *J. App. Phys.* **73**, 88 (1993).
- [80] P. Parayanthal and F. H. Pollak, *Phys. Rev. Lett.* **52**, 1822 (1984).
- [81] S. B. Zhang and J. E. Northrup, *Phys. Rev. Lett.* **67**, 2339 (1991).
- [82] M. Tajima, Y. Kawate, R. Toba, M. Warashina, and A. Nakamura, *Inst. Phys. Conf. Ser.* **149**, 257 (1996).

- [83] M. Noack, K. W. Kehr, and H. Wenzl, *J. Cryst. Growth*. **178**, 438 (1997).
- [84] N. Engler, H. S. Leipner, R. F. Scholz, P. Werner, and U. Gösele, *Physica B*. **310**, 742 (2001); and references therein.
- [85] N. Engler, H. S. Leipner, R. F. Scholz, P. Werner, F. Syrowatka, J. Schreiber, and U. Gösele, *Sol. Stat. Phenom.* **69-70**, 443 (1999).
- [86] H. S. Leipner, unpublished, 2000.
- [87] C. Frigeri, J. L. Weyher, and J. Jimenez, *J. Phys.: Condens. Matter*. **12**, 10335 (2000).
- [88] R. F. Scholz, P. Werner, U. Gösele, N. Engler, and H. S. Leipner, *J. Appl. Phys.* **89**, 7045 (2000).
- [89] A. C. Warren, J. M. Woodall, J. L. Freeouf, D. Grischkowsky, D. T. McInturff, M. R. Melloch, and N. Otsuka, *Appl. Phys. Lett.* **57**, 1331 (1990).
- [90] M. R. Melloch, N. Otsuka, K. Mahalingam, C. L. Chang, P. D. Kirchner, J. M. Woodall, and A. C. Warren, *Appl. Phys. Lett.* **61**, 177 (1992) and references therein.
- [91] T. J. Rogers, C. Lei, B. G. Streetman, and D. G. Deppe, *J. Vac. Sci. Technol. B* **11**, 926 (1993).
- [92] M.P. Allen and D. J. Tidesley, *Computer Simulation of Liquids* (Clarendon, Oxford, 1989).
- [93] F. H. Stillinger and T. A. Weber, *Phys. Rev. B* **31**, 5262 (1985).
- [94] J. Tersoff, *Phys. Rev. B* **37**, 6991 (1988); *ibid* **39**, 5566 (1989).
- [95] M. Sayed, J. M. Jefferson, A. B. Walker, and A. G. Cullis, *Nucl. Instrum. Meth. Phys. Res. B* **102**, 218 (1995).
- [96] K. Nordlund, J. Nord, J. Frantz and J. Keinonen, *Comput. Mater. Sci.* **18**, 283 (2000).
- [97] J. P. Hirth, J. Lothe, *Theory of Dislocations*, (Wiley, New York, 1982).
- [98] S. Ruvimov, C. Dicker, J. Washburn, and Z. Liliental-Weber, *Appl. Phys. Lett.* **72**, 226 (1998).
- [99] R. Toba, M. Warashina, and M. Tajima, *Mater. Sci. Forum*. **196-201**, 1785 (1995).
- [100] M. Tajima, R. Toba, N. Ishida, M. Warashina, *Mater. Sci. Tech.* **13**, 947 (1997).
- [101] M. A. Reshchikov, A. A. Gutkin, and V. E. Sedov, *Mater. Sci. Forum*. **196-201**, 237 (1995).
- [102] M. Suezawa, A. Kasuya, Y. Nishina, and K. Sumino, *J. Appl. Phys.* **76**, 1164 (1994).
- [103] D. T. J. Hurle, *J. Appl. Phys.* **85**, 6957 (1999), and references therein.
- [104] R. Krause-Rehberg and H. S. Leipner, *Positron Annihilation in Semiconductors* (Springer-Verlag, Berlin, 1999).
- [105] J. Gebauer, M. Lausmann, T. E. M. Staab, R. Krause-Rehberg, M. Hakala, and M. J. Puska, *Phys. Rev. B* **60**, 1464 (1999).
- [106] S. B. Zhang and A. Zunger, *Phys. Rev. Lett.* **77**, 119 (1996).
- [107] C. Le Berre, C. Corbel, K. Saarinen, S. Kuisma, P. Hautojärvi, and R. Fornari, *Phys. Rev. B* **52**, 8112 (1995).
- [108] M. Alatalo, B. Barbiellini, M. Hakala, H. Kauppinen, T. Korhonen, M. J. Puska, K. Saarinen, P. Hautojärvi, and R. M. Nieminen, *Phys. Rev. B* **54**, 2397 (1996)].
- [109] P. J. Dean, *Phys. Rev.* **157**, 655 (1967).

- 
- [110] J. Schreiber, S. Hildebrandt, H. Uniewski, and V. Bechstein, *Mater. Sci. Eng. B* **42**, 24 (1996).
- [111] A. Zylberstejn, R. H. Wallis, and J. M. Besson, *Appl. Phys. Lett.* **32**, 764 (1978).
- [112] B. V. Shanabrook, W. J. Moore, and S. G. Bishop, *J. Appl. Phys.* **59**, 2535 (1986).
- [113] R. Addinall and R. C. Newman, *Semicond. Sci. Technol.* **7**, 1005 (1992), and references therein.
- [114] S. K. Brierley, H. T. Hendriks, W. E. Hoke, P. J. Lemonias, and D. G. Weir, *Appl. Phys. Lett.* **63**, 812 (1993).
- [115] P. Dansas, *J. Appl. Phys.* **58**, 2212 (1985).
- [116] C. M. Wolfe and G. E. Stillman, *Appl. Phys. Lett.* **27**, 564 (1975).
- [117] Y. Q. Jia, H. J. von Bardeleben, D. Stievenard, and C. Delerue, *Phys. Rev. B* **45**, 1645 (1992).
- [118] H. Bracht, M. Norseng, E. E. Haller, K. Eberl, and M. Cardona, *Solid. Stat. Commun.* **112**, 301 (1999).
- [119] G. A. Baraff and M. Schlüter, *Phys. Rev. Lett.* **55**, 1327 (1985).
- [120] M. J. Puska, *J. Phys: Condens Matter* **1**, 7347 (1989).
- [121] T. Y. Tan and U. Gösele, *Mater. Sci. Eng. B* **1**, 47 (1988).
- [122] T. Y. Tan and U. Gösele, *Appl. Phys. Lett.* **52**, 1240 (1988).
- [123] E. W. Williams and A. M. White, *Solid State Commun.* **9**, 279 (1971).
- [124] M. Capizzi, C. Coluzza, V. Emiliani, P. Frankl, A. Frova, A. A. Bonapasta, Z. Sobiesierski, and R. N. Sacks, *J. Appl. Phys.* **72**, 1454 (1992);
- [125] J. S. Blakemore, *J. Appl. Phys.* **53**, R123 (1982).
- [126] J. Gebauer, M. Lausmann, F. Redmann, H. S. Leipner, R. Krause-Rehberg, E. R. Weber, and Ph. Ebert, *Phys. Rev. B* **67**, 235207 (2003).
- [127] H. Xu and U. Lindelfelt, *Phys. Rev. B* **41**, 5979 (1989).
- [128] P. S. Dobson, P. F. Fewster, D. T. J. Hurle, P. W. Hutchinson, J. B. Mullin, B. W. Straughan, and A. F. W. Willoughby, *Inst. Phys. Conf. Ser.* **45**, 163 (1979).
- [129] S. D. Lester, F. A. Ponce, M. G. Craford, and D. A. Steigerwald, *Appl. Phys. Lett.* **69**, 2737 (1996).
- [130] J. Duboz, F. Binet, D. Dolfi, N. Laurent, F. Scholz, J. Off, A. Sohmer, O. Briot, and B. Gil, *Mater. Sci. Eng. B* **50**, 289 (1997).
- [131] S. Evoy, H. G. Craighead, S. Keller, U. K. Mishra, and S. P. DenBaars, *J. Vac. Sci. Technol. B* **17**, 29 (1999).
- [132] M. Albrecht, H. P. Strunk, J. Weyher, I. Grzegory, S. Porowski, and T. Wosinski, *J. Appl. Phys.* **92**, 2000 (2002).
- [133] H. Lei, H. S. Leipner, J. Schreiber, J. Weyher, T. Wosinski, and I. Grzegory, *J. Appl. Phys.* **92**, 6666 (2002).
- [134] F. A. Ponce, D. P. Bour, W. Götz, and P. J. Wright, *Appl. Phys. Lett.* **68**, 57 (1996).
- [135] A. Cremades, J. Piqueras, C. Xavier, T. Monterio, E. Pereria, B. K. Meyer, D. M. Hofmann, and S. Fischer, *Mater. Sci. Eng. B* **42**, 230 (1996).

- [136] S. Christansen, M. Albrecht, W. Dorsch, H. P. Strunk, A. Pelzmann, M. Mayer, M. Kamp, J. Ebeling, C. Zanotti-Fregonara, and G. Salviatti, *Mat. Sci. Eng. B* **43**, 243 (1997).
- [137] L. W. Tu, Y. C. Lee, S. J. Chen, I. Lo, D. Stocker, and E. F. Schubert, *Appl. Phys. Lett.* **73**, 2802 (1998).
- [138] H. Siegle, P. Thurian, L. Eckey, A. Hoffman, C. Thomsen, B. K. Meyer, H. Amano, I. Akasaki, T. Detchprohm, and K. Hiramatsu, *Appl. Phys. Lett.* **68**, 1265 (1996).
- [139] P. Perlin, T. Suski, H. Teiseyre, M. Leszczynsky, I. Grzegory, J. Jun, S. Porowski, P. Boguslawski, J. Bernholc, J. C. Chervin, A. Polian, and T. D. Moustakas, *Phys. Rev. Lett.* **75**, 296 (1995).
- [140] J. Neugebauer and C. G. Van de Walle, *Appl. Phys. Lett.* **69**, 503 (1996).
- [141] C. G. Van de Walle and J. Neugebauer, *Mater. Sci. Forum* **258–263**, 19 (1997).
- [142] C. Wetzel, T. Suski, J. W. Ager, E. R. Weber, E. E. Haller, S. Fischer, B. K. Meyer, and P. Perlin, *Phys. Rev. Lett.* **78**, 3923 (1997).
- [143] T. Ogino and M. Aoki, *Jpn. J. Appl. Phys.* **19**, 2395 (1980).
- [144] E. R. Glaser, T. A. Kennedy, K. Doverspike, L. B. Rowland, D. K. Gaskill, J. A. Freitas, Jr., M. Asif Khan, D. T. Olson, J. N. Kuznia, and D. K. Wickenden, *Phys. Rev. B* **51**, 13326 (1995).
- [145] J. L. Weyher, M. Albrecht, T. Wosinski, G. Nowak, H. P. Strunk, and S. Porowski, *Mater. Sci. Eng. B* **80**, 318 (2001).
- [146] J. L. Rouvière, J. L. Weyher, M. Seelmann. Eggebert, and S. Porowski, *Appl. Phys. Lett.* **73**, 668 (1998).
- [147] G. Nowak, X. H. Xia, J. J. Kelly, J. L. Weyher, and S. Porowski, *J. Cryst. Growth* **222**, 735 (2001).
- [148] C. Kisielowski, J. Krüger, S. Ruvimov, T. Suski, J. W. Ager, E. Jones, Z. Liliental-Weber, M. Rubin, and E. R. Weber, *Phys. Rev. B* **54**, 17745 (1996).
- [149] P. Perlin, C. Jauberthie-Carillon, J. P. Itie, and A. S. Miguel, *Phys. Rev. B* **45**, 83 (1992).
- [150] H. Xia, Q. Xia, and A. L. Ruoff, *Phys. Rev. B* **47**, 12925 (1993).
- [151] G. Salviatti, M. Albrecht, C. Zanotti-Fregonara, N. Armani, M. Mayer, Y. Shreter, M. Guzzi, Yu. V. Melnik, K. Vassilevski, V. A. Dmitriev, and H. P. Strunk, *phys. stat. sol. (a)* **171**, 325 (1999).
- [152] K. Saarinen, T. Laine, S. Kuisma, J. Nissilä, P. Hautojärvil, L. Dobrzynski, J. M. Baranowski, K. Pakula, R. Stepniewski, M. Wojdak, A. Wyszomolek, T. Suski, M. Leszczynski, I. Grzegory, and S. Porowski, *Phys. Rev. Lett.* **79**, 3030 (1997).
- [153] K. Saarinen, J. Nissilä, J. Oila, V. Ranki, M. Hakala, M. J. Puska, P. Hautojärvi, J. Likonen, T. Suski, I. Grzegory, B. Lucznik, and S. Porowski, *Physica B* **273–274**, 33 (1999).
- [154] S. J. Zhou, D. L. Preston, and F. Louchet, *Acta mater.* **47**, 2695 (1999).

# Acknowledgments

First of all, I would like to express my great gratitude to Priv.-Doz. Dr. Hartmut S. Leipner and Prof. Dr. H.-R. Höche for providing me the opportunity to work at Interdisziplinäres Zentrum für Materialwissenschaften (IZM) and guiding my studies. I am very grateful to Priv.-Doz. Dr. Hartmut S. Leipner for his friendly and effective promotion and help in my study and living since I arrived at Halle. I appreciate the delightful work and discussions with him.

I am indebted to Dr. N. Engler for helping to prepare the samples and to make computer simulations. I am deeply impressed by his easy-going quality. I thank Dr. J. Schreiber, H. Mähl, and V. Bondarenko at Fachbereich Physik for their important support and help in the CL and positron annihilation experiments. I also thank Dr. B. Gründig at TU Bergakademie, Freiberg for carrying out Hall-effect measurements.

I thank all of my colleagues at the Kristal-Labor and IZM for their valuable help and efficient cooperation.

I should also thank Prof. U. Gösele and Dr. P. Werner at Max-Planck-Institut für Mikrostrukturphysik for allowing me to do preparation and TEM work there.

I can never forget to present my appreciation to Prof. Y.-Y. Zhang at Sichuan university, China for leading me into the field of science.

I address my special thanks to my parents and my sister. It is with their love, encouragement and support that I can breezily and absorbedly concentrate on the world of science.

The financial support from the Kultusministerium Sachsen-Anhalt, Deutschland, is largely appreciated.



# Erklärung

Hiermit erkläre ich an Eides Statt, dass ich die vorliegende Arbeit selbständig und ohne fremde Hilfe verfasst und nur die angegebenen Quellen und Hilfsmittel verwendet habe. Ergebnisse anderer wissenschaftlicher Arbeiten wurden als solche gekennzeichnet. Diese Arbeit wurde bisher weder im In- noch im Ausland in gleicher oder ähnlicher Form in einem Prüfungsverfahren vorgelegt. Ich erkläre hiermit, dass ich mich bis zu dem jetzigen Zeitpunkt noch nie um einen Doktorgrad beworben habe.

Halle(Saale), Juni 2003

Haile Lei



# Lebenslauf

Name: Haile Lei

geb. am: Aug. 20, 1975

Geburtsort: Mianzhu, China

Familienstand: unverheiratet

Adresse: Lutherstraße 43, 06110, Halle/Saale

1981 – 1987, Xiangyang-Grundschule in Mianzhu, China

1987 – 1993, Tumen- und Chengbei- Oberschule in Mianzhu, China

1993 – 1999, Physikstudium an der Sichuan Universität, China

1997 Abschlussarbeit (Bachelor): Design Integrierter Koinzidenz- und Antikoinzidenzschattkreise

1999 – 2000, Promotionsstudent an der Université Libre de Bruxelles, Belgien

2000 – 2003, Wissenschaftlicher Mitarbeiter an der Martin-Luther-Universität Halle-Wittenberg, Deutschland

2001 Abschlussprüfung Festkörperphysik als Zulassungsvoraussetzung zur Promotion (Äquivalenz zum Masterabschluss)